Design of new protective systems based on the intermetallic compound RuAl

Dissertation

zur Erlangung des Grades

des Doktors der Ingenieurwissenschaften

der Naturwissenschaftlich-Technischen Fakultät III

Chemie, Pharmazie, Bio- und Werkstoffwissenschaften

der Universität des Saarlandes.

von

MARIA AGUSTINA GUITAR

Saarbrücken – 2014

Tag des Kolloquiums:	27.06.2014
Dekan:	Prof. Dr. Volkhard Helms
Erstgutachter:	Prof. Dr. Frank Mücklich
Zweitgutachter:	Prof. Dr. Dirk Bähre
Vorsitz:	Prof. Dr. Guido Kickelbick
Akad. Mitarbeiter:	Dr. Michael Marx

"God made solids, but surfaces were the work of the devil."

W. Pauli

List of contents

Acknowledgements

I want to express my gratitude to all the people who supported my work for this thesis. I would like to thank my supervisor Prof. Dr.-Ing Frank Mücklich (Functional Materials, Department of Materials Science, Saarland University) for giving me the opportunity to carry out this doctoral thesis at his institute. For accepting the revision of this work, I am also very grateful to Prof. Dr.-Ing. Dirk Bähre (Institute of Production Engineering).

Many thanks go to the Deutsche Akademischer Austausch Dienst (DAAD) as well, for the funding during my doctoral thesis. Also, I am grateful to Dr. Esteban Ramos-Moore for the critical scientific discussion and input for this work. To Dr. U. Klotz and Dipl.-Ing. M. Eisenbart from the Research Institute of Precious Metals + Metals Chemistry (FEM), (Schwäbisch Gmünd, Germany) for the help with the wetting measurements. To Prof. Dr. Helmut Seidel, G. Marchand, H. Völlm and C. Kirsch (Micromechanic, Microfluidics/Microactuators) for providing the facilities and the help for the films deposition.

Furthermore, I appreciate the feedback provided by my colleagues Dr. F. Soldera, Dr. K. Woll, Dipl.-Ing. S. Suárez, Dipl.-Ing. F. Miguel, Dipl.-Ing. C. Pauly, Dipl.-Ing. N. Souza, M.Sc. F. Lasserre, and Dipl.-Ing. B. Bax after reading this manuscript; and to M.Sc. H. Aboulfadl for the APT analysis. Particularly, I would like to thank C. Pauly and B. Bax for the German translation of the abstract. I am also grateful to all the colleagues from the Functional Materials Institute, who helped me during the experimental part of my work. A special mention is made to my office co-workers, Paula and Jeni, for the time shared during the past years.

Last but not least I would like to thank my family who gave me support during my whole academic formation and most importantly to my husband Sebastián, for his patience, daily encouragement, support and unconditional love he has guaranteed me over the years.

Abstract

RuAl shows a high melting point, good ductility at room temperature and excellent oxidation resistance due to the growth of a protective α-Al_2O_3 layer with similar thermal expansion, increasing its adherence. RuAl is thus a promising protective coating material oxidising high-temperature environments, yet this has yet to be thoroughly studied.

RuAl thin films on stainless steel (SS) are produced from magnetron sputtered multilayers (periods of 3 nm). Since bulk and thin film properties often differ, thermal stability, grain growth, oxidation and substrate interaction were studied at different temperatures.

The films showed phase and thermal stability after 6 h at 750 °C. Normal and abnormal grain growth occurred at 650 °C $\leqslant$ T $\leqslant$ 750 °C, induced by a 3D curvature-driven evolution and due to impurities and grain-orientation-specific driving forces, respectively.

α-Al_2O_3 is the only oxide present even at T = 750 °C, an advantage over most studied aluminides. Its linear, phase-boundary controlled growth changes to a parabolic, diffusion-controlled process at about 200 nm (at 900 °C). Excess Ru in RuAl diffusing into the SS avoids the precipitation of new δ-Ru regions during oxidation. Additionally, Fe and Cr from the SS contribute to the stabilisation of the microstructure.

RuAl films have also been evaluated for glass moulding dies. High-temperature contact angles show molten borosilicate glass does not wet the films. Chemical interactions occur under air, but not under Ar.

Kurzzusammenfassung

RuAl zeichnet sich aus durch einen hohen Schmelzpunkt, Raumtemperaturduktilität und sehr gute Oxidationsbeständigkeit aufgrund des Wachstums einer gut haftenden α-Al_2O_3-Schicht mit ähnlicher thermischer Ausdehnung. Damit ist RuAl ein interessanter Kandidat für Hochtemperaturbeschichtungen, erfordert jedoch weitere Forschung.

RuAl-Dünnschichten wurden durch Magnetronsputtern von Multilagen (3 nm Periode) auf CrNi-Stahl hergestellt. Da die Eigenschaften dünner Schichten oft von denen des Vollmaterials abweichen, wurden thermische Stabilität, Kornwachstum, Oxidtion und Substrateinfluss bei verschiedenen Temperaturen untersucht.

Die Schichten zeigen thermische und Phasenstabilität nach 6 h bei 750 °C. Normal und anormales Kornwachstum treten bei 650 °C $\leqslant$ T $\leqslant$ 750 °C auf. Ersteres reduziert die Korngrenzenkrümmung, während letzteres mit Verunreinigungen und orientierungsabhängigen Oberflächenenergien in Verbindung steht.

Anders als bei vielen anderen Aluminiden wächst auf RuAl lediglich α-Al_2O_3. Sein lineares, grenzflächenbestimmtes Wachstum geht ab 200 nm (bei 900°C) in diffusionskontrolliertes, parabolisches Wachstum über. Dabei diffundiert Ru in den Stahl, wodurch die Ausscheidung von δ-Ru vermieden wird. Fe und Cr aus dem Stahl tragen zur Stabilisierung der Mikrostruktur bei.

RuAl wurde ebenfalls als Beschichtung von Blankpressmatrizen für Glas bewertet. Borosilikatschmelze zeigt keine Benetzung der Schichten. Chemische Wechselwirkungen treten an der Luft auf, jedoch nicht unter Ar.

List of symbols, units and abbreviations

Symbol	Description
a	lattice parameter
C_{ij}	mechanical constant
d	interplanar distance
k	oxidation rate
k_p	oxidation rate from mass gain
k_x	oxidation rate from oxide thickness
L_c	critical load
n	time exponent
Q	activation energy
R	gas constant
r	grain radius
s	stress
T	temperature
t	time
T_g	softening point
T_m	melting temperature
T_s	temperature of substrate
α	coefficient of thermal expansion
γ	surface/interfacial energy
ΔG	Gibbs free energy
ΔHf	enthalpy of fusion
ε	strain
θ	diffraction (Bragg) angle
λ	X-Ray wave length
Λ	period of multilayer films
Λ_c	critical periof of multilayers
ρ	density
υ	Poisson's coefficient

Units	Description
°C	Celsius degree
Å	Angstrom
bar	bar
eV	electron Volt
h	hour
Hz	Hertz
J	Joule
K	Kelvin
m	meter
N	Newton
Pa	Pascal
s	second
V	volt
W	Watt

Abbreviations	Description
(HT)XRD	(high temperature) X-ray diffraction
AC	alternating current
APT	Atom Probe Tomography
bcc	body-centred cubic
CTE	coefficient of thermal expansion
DC	direct current
EBSD	electron backscattered diffraction
EDX	energy dispersive X-ray spectroscopy
fcc	face-centred cubic
FIB	focused ion beam
GB	grain boundary
GI-XRD	grazing incidence X-ray diffraction
GMD	glass moulding dies
hcp	hexagonal close-packed
I-A	image analysis
IMC	Intermetallic compound
IPF	inverse pole figure
MA	mechanical alloying
MLs	multilayers
NC	nanocrystalline
PVD	physical vapour deposition
RE	reactive elements
SAD	selected area diffraction
SEM	scanning electron microscopy
SS	Stainless steel
STEM	scanning transmision electron microscopy
TEM	transmission electron microscopy
W-A	Warren-Averbach method

1

Introduction

1.1. Motivation

Single-phase RuAl has been considered for applications at elevated temperatures as a consequence of a series of very interesting properties. It shows an unusual combination of high melting point, high temperature strength, oxidation and corrosion resistance (even above 1000 °C), and good toughness at room temperature [1,2]. However, this intermetallic compound is difficult to produce as single-phase RuAl using conventional synthesis techniques, such as melting and casting, mainly given the large difference between the melting points of Ru (~2330 °C) and Al (~660 °C). For this reason, coatings and thin films are an interesting and effective way to benefit from the good properties of RuAl to protect the underlying alloy substrate from atmospheric degradation.

Single-phase RuAl has been successfully produced in form of thin films [3,4]. However, to this date, no studies have been conducted neither on the films stability at elevated temperatures nor on the interaction with technically relevant substrates. A satisfactory coating system requires an excellent adhesion to the underlying substrate, good oxidation resistance by forming highly protective and mechanically strong oxide scales during long exposure times, and limited interdiffusion between the coating and the substrate, avoiding the formation of depletion zones and/or brittle phases.

The scientific interest of this work arises from the possibility of applying the RuAl intermetallic compound as a novel thin film material to be used as protective coating on components demanding oxidation resistance at elevated temperatures such is the case of tools and dies for precision glass moulding.

1.2. Intermetallic compounds

Intermetallic compounds (IMC[1]) boast attractive high-temperature properties due to their long-range order, which reduces dislocation mobility and diffusion processes at elevated temperatures [5]. IMCs are considered a class of material between metals and ceramics, because their metallic interatomic bonding lies somewhere between covalent and ionic. These strong bonds confer high thermodynamic stability and hardness, making IMCs promising structural materials for high temperature applications. However, this also limits their plasticity, making most of them brittle, a main drawback in structural applications [6]. This brittleness makes their processing difficult or even impossible [6]. Despite relatively high strength at high temperatures, ideal for such structural applications, their deformation behaviour, intermediate between metals and ceramics, more closely resembles the latter, showing low ductility particularly at low and intermediate temperatures [7].

IMCs ductilisation or strengthening usually involves the addition of alloying elements, such as boron, or a composition adjustment to take advantage of second phases [7]. This often produces changes in the inherent density, melting point and high-temperature strength. Yet the addition of a second phase can be detrimental for the oxidation resistance. Such is the case of Ti_3Al, whose ductility at room temperature is improved by the addition of Nb but its oxidation resistance remains insufficient [7]. The combination of creep resistance and low density in these compounds positions them among nickel-based superalloys and advanced ceramics, regarding performance and overall properties. Despite their current disadvantages, IMCs are still being considered as potential substitutes for metallic alloys in a variety of high temperature applications.

The combination of high-temperature strength and superior oxidation resistance makes intermetallic materials exceptional candidates to be used in high temperature component design, providing not only longer service-life of the devices but also the possibility to operate above current operating temperatures. The high oxidation resistance can be achieved by the formation of a continuous, uniform and well adhered surface oxide layer, with high thermodynamic stability and slow thickening rate [8]. Oxidation resistance at high temperatures is provided particularly by the presence of Cr, Si, or Al which form protective oxide layers. Thus, most IMCs that might be considered for high-temperature applications (either as base material or coating) are either *chrominides*, *silicides* or *aluminides,* forming Cr_2O_3, SiO_2 or Al_2O_3, respectively. These oxides are known to be the most protective among oxide scales. However, under high-temperature oxidation (above 1000 °C), Cr oxide is volatile and Si oxide may form low-melting silicates [6]. Aluminides are strongly favoured for high-temperature applications in view of their oxidation resistance. They must contain a sufficiently high aluminium concentration to ensure the formation of stable Al_2O_3 and thus, provide a proper oxidation resistance at elevated temperatures [6]. Alumina can be

1) Not to be confused with how certain authors [7,195] abbreviate *intermetallic matrix composites.*

present in the form of thermally stable or metastable phases. The metastable phases γ- or θ-Al_2O_3 are predominant below 900 °C on iron and nickel aluminides, whereas α-Al_2O_3 is the most thermodynamically stable phase formed at higher temperatures [9,10].

Aluminide-based IMCs, such as Fe-Al, Ni-Al, Ti-Al and Ru-Al, rely on the formation of a highly protective alumina scale at the surface to effectively isolate the underlying alloy substrate from aggressive environments. The retention of the alumina scale may occur by different mechanisms and at different rates depending on the system. Among the wide variety of intermetallics, the aluminides such as Fe-Al, Ni-Al and Ti-Al are attracting most of the attention for applications and they are the focus of thorough studies. FeAl (36-50 at.% Al) presents lower density than commercial Fe-based alloys and much better corrosion and high-temperature oxidation resistance due to the high Al content, which allows the formation of a slowly-growing and mechanically-stable external Al_2O_3 scale at temperatures above 500 °C. However, its room temperature ductility is low [5]. One of the most deeply studied intermetallic systems is Ni-Al in its different chemical configurations [11–14]. NiAl is the most promising of the Ni-aluminides family for high-temperature structural applications, because of its higher melting temperature, higher thermal conductivity and its very good oxidation resistance. However, it presents both low deformability at room temperature and insufficient strength and creep resistance above 1000 °C [7]. Other very attractive system is the Ti-Al, with its intermetallic phases TiAl and $TiAl_3$. The latter shows low specific weight and very high strength at temperatures above 600 °C, but minimum ductility at T > 700 °C. Furthermore, its low density, high strength at elevated temperatures and good oxidation resistance make TiAl ideal for aircraft-engines and gas turbines [15–17].

1.3. B2 intermetallics and the Ru-Al system: a literature overview

1.3.1. B2 intermetallic compounds

The B2 phase has a CsCl structure (ordered bcc) with only two atoms per unit cell (Figure 1.1) and it is adopted by many AB-type compounds, such as AgMg, AuZn, CoZr, NiAl, FeAl, RuAl, etc. These compounds often exist over a range of off-stoichiometry. Excess elements are accommodated as constitutional defects [18].

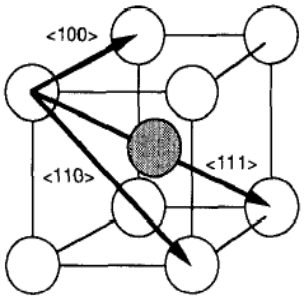

Figure 1.1: B2 crystal structure. The slip vectors are identified [18].

Dislocations with three different slip vectors (<100>, <110> and <111>) have been observed in these compounds. The activation of one or more of these slip vectors is a function of the B2 system. It also depends strongly on the composition and deformation temperature [18,19]. Furthermore, the elastic properties of B2 alloys are highly dependent on the crystal orientation, presenting an anisotropic elastic constant (C_{ij}) [18].The minimum yield strength and hardness are usually observed at (or near to) the stoichiometric composition. The reason is that both vacancies and antisite defects, which are responsible for the strengthening, usually have their minimum concentration close to the stoichiometric composition [18]. However, the elastic modulus E of polycrystalline FeAl, NiAl and CoAl was found not being strongly composition dependent [18].

Aluminides in form of coatings or thin films have been studied in the last years with the aim of taking advantage of their interesting properties. For instance, Ir-Al coatings have been used to protect carbon materials from oxidation at high temperature [20], whereas NiAl thin films has been studied as possible protective coatings for glass moulding dies [21–23]. These were deposited onto different substrates using magnetron sputtering from a NiAl compound target. The composition, texture and microstructure of said films were characterised with varying the deposition power and substrate. NiAl bond coats for thermal barrier coatings of about 20 μm were also deposited using electron beam directed vapour deposition (EB-DVD) [24]. Moreover, NiAl coatings 10 μm thick with 10 nm grain size were produced using a partitioned Ni-Al target, showing a nanohardness of 11.5 GPa [25]. Corrosion studies on Ni_3Al films deposited by pulsed-laser deposition presented a considerable improvement in corrosion resistance compared to pure Ni. Additionally, Ni-Al intermetallic compounds were fabricated from reacted multilayers (MLs), and the reaction kinetics fully analysed [26–29].

1.3.2. Ru-Al system

The formation of intermetallic phases in the Ru-Al system is observed in detail in the phase diagram of Figure 1.2. Six intermetallic phases are formed from these two elements each possessing unique structures, none of which are fcc or hcp such the Al and Ru (fcc and hcp, respectively). In this particular system, all the intermetallics remain ordered until the melting point is reached.

Single-phase RuAl exists as a B2 crystal, covering off-stoichiometry on both sides from 49.7 to 53.8 at.% Al, as established by Gobran *et al*. [30]. However, this go up to 54.5 at.% Al if samples are quenched from high temperatures. Stoichiometry deviation implies the presence of point defects, including substitutional atoms, vacancies and interstices [31,32]. Other intermetallic phases are also possible in the Ru-Al system ($RuAl_6$, $RuAl_2$, etc.), as observed in Figure 1.2. The high thermodynamic stability of stoichiometric RuAl is reflected in its high melting point ($T_m \sim 2050$ °C) and heat of formation (-124.1 ± 3.3 kJ/mol) reported for RuAl [33], indicating a very strong chemical interaction. The interdiffusion coefficient in coarse-grained (CG) B2-RuAl was found to be

$D_0 = 2.2\ (\pm 1.6) \times 10^{-6}\ m^2s^{-1}$, with an activation energy $Q = 236 \pm 18\ kJ/mol$, as determined by Woll and co-workers [34].

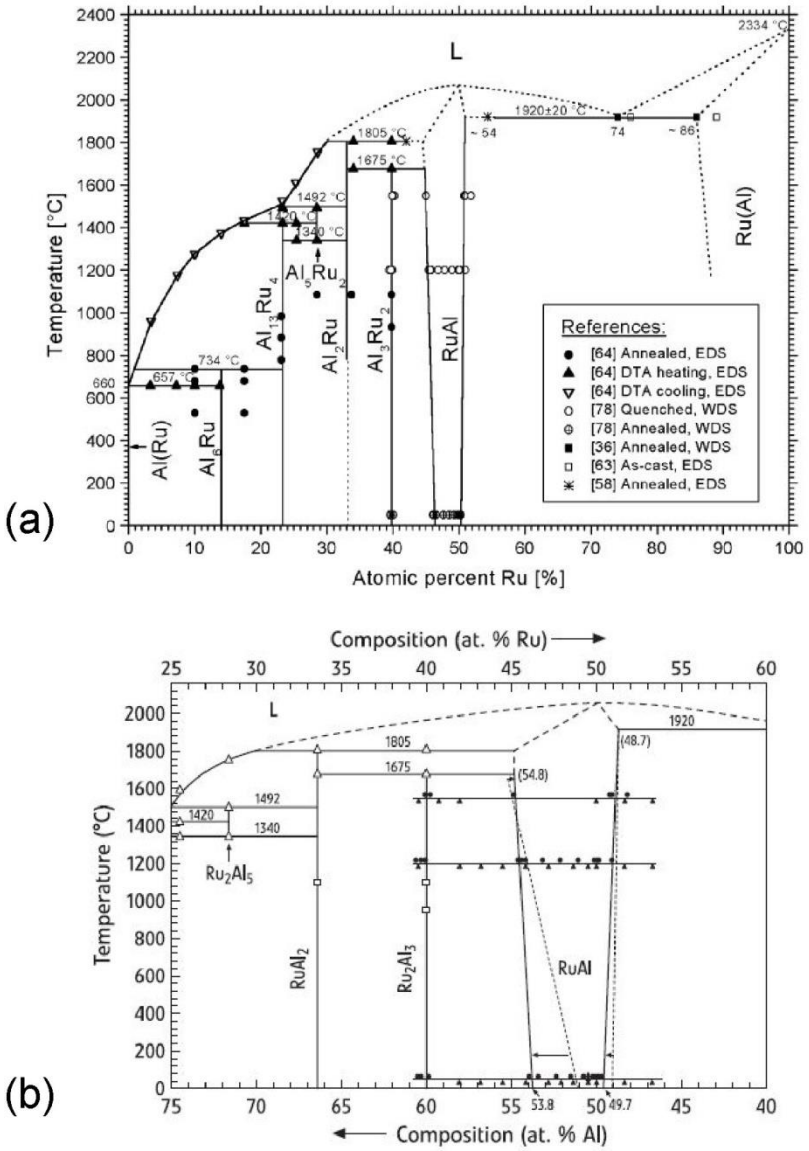

Figure 1.2: (a) Ru-Al phase diagram based in experimental results from diverse authors [2] and (b) region of the diagram modified by Gobran [30].

The combination of very high melting point (~2050 °C), high-temperature strength, oxidation and corrosion resistance and particularly good room temperature toughness [1,2] placed to the B2-RuAl in the focus of considerable attention as an attractive material for high-temperature applications in aggressive environments [35]. Single phase RuAl is very difficult to manufacture by conventional melting processes without volatilisation of Al in the molten state, which results in highly inhomogeneous materials [1,36,37]. Fabrication through powder metallurgy has been developed in different ways in order to obtain single-phase RuAl. This compound was successfully synthesised by Liu [38] using mechanical alloying. Borah [39] obtained RuAl+α-Ru using the same

method but with larger powder particle sizes than in the previous case. Meanwhile, Gobran [40] fabricated single-phase RuAl by the reactive sintering method and multi-phase compound by reactive hot pressing. The exothermic reaction between Ru and Al is an important advantage in reactive sintering, but extended treatments at high temperature are still required in some cases to obtain a homogeneous microstructure.

The oxidation resistance of RuAl is good up to about 1100 °C, being somewhat better for Al-rich compositions as it might be expected given the tendency of Al to form a protective Al_2O_3 layer at the oxidation interface. It can be further improved with specific ternary alloying additions, such as Y, Cr, B or Re [41]. The stable α-Al_2O_3 is the only oxide observed to form in RuAl at the investigated temperature range (up to 1300 °C) [42,43], whereas other B2 aluminides like NiAl grow non protective oxides such as θ- and δ-Al_2O_3 [44]. The volume change produced during the transformation from transition oxides to stable α-Al_2O_3 results in cracking of the oxide scale. This decreases the oxidation resistance of the intermetallic material with severe consequences for the material stability, exposing fresh material to the oxidising atmosphere. Furthermore, this compound possesses good thermal conductivity, similar to that of pure platinum, showing values of ~70-80 W/mK for both stoichiometric and Ru-rich alloys ($Ru_{53}Al_{47}$) [45].

An important advantage for the use of this intermetallic in oxidising atmospheres, compared to other B2-aluminides, is based on the coefficient of thermal expansion (CTE), which is significantly lower than that of FeAl, CoAl and NiAl, and is closer to that of α-Al_2O_3 for a wide temperature range (between 123 °C and 1500 °C) (see Figure 1.3). Additionally, its value does not show a strong stoichiometry dependence [46]. Since the CTE of α-Al_2O_3 is almost identical to that of RuAl in a large temperature range, the generation of thermal stresses as a consequence of the CTE mismatch, during thermal cycling and cooling from high temperatures is negligible and the adherence of the protective layer is enhanced [46].

The mechanical properties of the RuAl phase have been studied in some detail by Fleischer and Pollock [19,47,48]. The ductility of B2 Al-Ru based alloys is influenced by the addition of B and the Ru content. According to Wolff et al. [49], samples with stoichiometric composition presented a maximum in ductility during compression tests, but a decrease in strength compared to the eutectic composition of the Ru-Al system [49]. However, Fleischer et al. [47] observed the ductility increase with the Ru-content. The remarkable compressive ductility observed in the RuAl system is unusual for high-temperature intermetallics at room temperature.

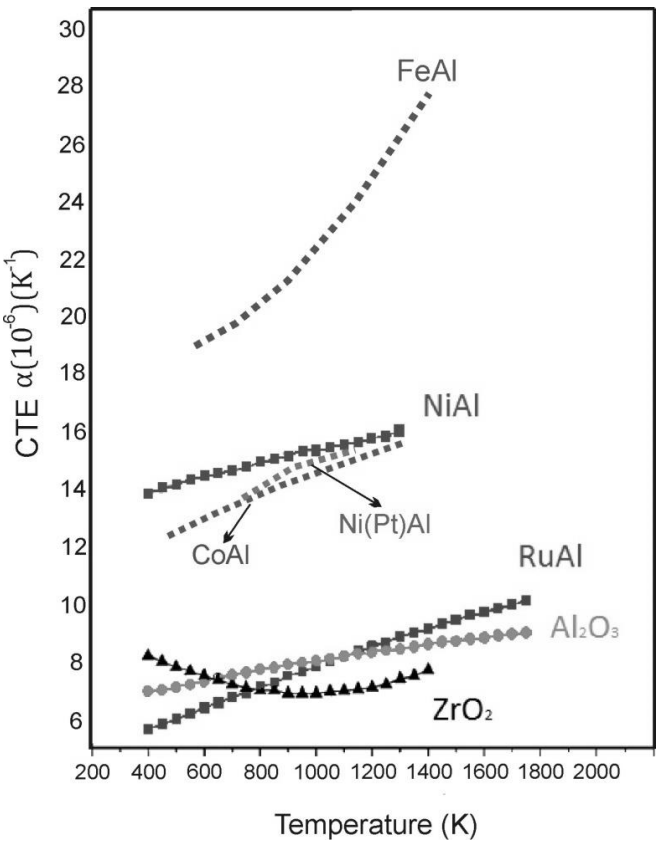

Figure 1.3: thermal expansion coefficients of B2 intermetallic aluminides as a function of temperature based on [46]. The CTE of RuAl is compared to that of other B2 intermetallic compounds and α-Al_2O_3.

1.3.3. RuAl thin films

Research studies on the Ru-Al thin film system started in the early ´80s by Chaudhury [50] who looked at vapour-deposited Al-Ru films containing 10-15 wt.% Ru. A supersaturated Al(Ru) solid solution is formed during the annealing, showing a fcc structure and stability up to 350 °C. Precipitates of an unknown metastable phase and $RuAl_6$ presenting an orthorhombic phase were detected at higher temperatures. The metastable phase was identified as a cubic phase from the A_3B_2 (e.g. Mo_3N_2) or A_2B_{11} (e.g. Mg_2Zn_{11}) types. The stable phase corresponding to the Al+Al_6Ru equilibrium phases is reached after annealing for long times. Anlage et al. [51] used evaporating deposition techniques to synthesise non-equilibrium solid-state Ru-Al thin films by reacting a series of multilayers at elevated temperatures. From the annealing of Ru/Al bilayers at 450 °C, icosahedral Al-16.5 at.%Ru films were formed.

The formation of the RuAl intermetallic phase using laser interference metallurgy (LIMET) from Ru/Al MLs was studied by Mücklich et al. [52]. By this method it was possible to obtain the intermetallic phase with a periodic pattern, making the functionalisation of the film surface possible.

The first studies on equiatomic Ru/Al MLs for synthesis of single-phase RuAl thin films were carried out by Zotov et al. [3] and Woll [4]. Zotov et al. [3] carried out a detailed investigation of the interdiffusion, the reaction behaviour and the B2-RuAl formation in Ru/Al MLs with periods (Λ) between 2.2 and 22.4 nm. The effect of the ML period on the formation of the B2-RuAl intermetallic was analysed. The kinetics of the B2-RuAl grain growth were found to be Λ-dependent, being slower in the as-deposited MLs with $\Lambda < 4.5$ nm. Thus, the transformation of the MLs into the B2-RuAl phase is incomplete for short annealing times (10 min). A faster interdiffusion along vertical GBs accelerates the grain growth in MLs with $\Lambda > 4.5$ nm at $T \geq 600$ °C. They established a critical period (Λ_c) for the direct formation of the single-phase RuAl.

Moreover, Woll [4] carried out a systematic study on the solid diffusion and self-propagating reactions in stoichiometric Ru/Al MLs with periods between 2.2 and 178 nm. The solid-state reaction, for $\Lambda \geq 44$ nm, begins at temperatures close to 400 °C regardless the Λ, at the Ru/Al interface, dominated by Al diffusion into the Ru-layer. MLs with $\Lambda < 22$ nm transform directly to RuAl at $T > 425$ °C and the transformation is diffusion controlled. Increasing the period of the MLs ($\Lambda > 44$ nm), the single-phase RuAl is formed after the sequential formation of diverse Ru_xAl_{1-x}. The phase sequence for the single-RuAl formation is highly dependent on Λ, being more complex for larger periods. MLs with $\Lambda = 178$ nm transform to RuAl following the formation of $RuAl_6$, Ru_4Al_{13}, $RuAl_2$ at 303 °C, 491 °C and 537 °C, respectively. Additionally, the advantage of the highly exothermic synthesis reaction occurring in the Ru-Al system was considered by the same author for a potential application as reactive bonding for electronic devices. For that, the solid-state phase transformations and self-propagating reactions in equiatomic Ru/Al MLs were also characterised.

The self-propagating reactions also allow the single-phase thin film synthesis, where one-stage transformations at solid Ru/liquid-Al interfaces occur regardless of the period. However, for $\Lambda <$ 35 nm the reaction rate decreases considerably. Reaction rates and temperatures of 10.9 m/s and 1946 °C, reveal the superior energy density compared to commercial Ni/Al layers. Ru/Al multilayer reactive bonding is thus a promising technological advance in the context of an ongoing miniaturization in microsystems technology.

A brief study on the oxidation resistance of RuAl thin films, in terms of the surface morphology and electrical resistance, was carried out by Howell [53]. The RuAl thin films showed alternating Al_2O_3 and Ru-rich layer morphologies when oxidising in pure O_2 atmosphere up to 850 °C. However, the study did not show conclusive and detailed results of the oxide morphology and oxidation kinetics. RuAl films have also been studied for potential application as interlayers for the epitaxial growth of FePt films [54]. The magnetron-sputtered films grew with a preferential orientation in the <100> direction and with an average grain diameter of 5 nm.

1.3.4. RuAl as protective coating for glass moulding dies

Glass lenses have shown an increasing demand in the field of high-resolution digital cameras and mobile phone cameras, as well as for CD/DVD players and recorders, as a consequence of the ongoing demand in the miniaturisation of electronic devices. In order to reduce the cost, size and weight of the final devices, lenses with complex shapes (e.g. aspheric lenses, micro-lens arrays, etc.) and reduced sizes are strongly favoured. The high surface complexity of these types of lenses, in combination with the requirement of highly accurate dimensions, will limit the use of existing manufacturing technologies. The conventional production methods for glass lenses, which include several grinding and polishing steps and require long production times, tend to be replaced by precision glass-moulding. This technique shows a great potential for the mass production of aspheric glass lenses with high precision and low cost.

In the fabrication of glass lenses by moulding there are still three critical problems which must be overcome, in order to maintain the quality of the final glass products, namely: *wear, oxidation and sticking adhesion* by molten glass. Since inorganic glasses require working temperatures of at least 500 °C to be moulded [55], thermal and mechanical stresses shorten the duty life of the glass moulding dies (GMD), a major drawback. Moreover, a strong chemical interaction between hot glass and the moulding surface derive in the degradation of the second, due to small glass adhesions or abrasions. The chemical interactions between the coating and the glass must be therefore reduced in order to minimise these adhesions, thus maximising the lifetime of the moulding tools. Furthermore, glass-mould interactions should not result in deficient unmoulding (non-wettability with molten glass). To overcome these problems, different solutions can be adopted, namely: a) developing low softening-point glasses - more expensive and difficult to control surface properties [56]; b) operating in an inert environment, requiring more sophisticated equipment and noble gas installations; or c) the use of protective coatings (working layers exposed directly to the work environment) to increase the life of the GMD and obtain the best quality of the glass products.

Oxidation-resistant and non-sticking protective coatings are currently under development in order to optimise the performance and reliability of the moulds and the quality of the glass products. Many materials have been developed as potential coatings for GMDs. The different materials for mould coatings presented in the literature were tested at different temperatures, atmospheres and using glasses with a wide range of chemical compositions. For this reason, the comparison and selection of the optimal material is very difficult and each system must be analysed separately. Moreover, one single coating might not completely fulfil all the requirements, therefore, an optimised, multi-layered, graded coating 'architecture' must be constructed [57,58]. Tungsten carbide (WC) is used as mould material for normal optical and low transition temperature (T_g)

glasses [59]. Ni is used to mould diffractive optics from low-Tg glasses due to its low thermal resistance [55]. On the other hand, noble-metal-based coatings present a considerable amount of advantageous properties, especially regarding their chemical interaction with glass. Pask and co-workers [60] studied the nature of wetting and adherence of $Na_2Si_2O_5$ glass to Cu, Ag, Au, Pd, Pt and Ni under different atmospheres. The contact angle of molten sodium disilicate on Pt was observed to be sensitive to pressure and temperature changes, and even wetting of the surface occurred. A reaction between glass and lead substrate was also observed, indicated by a green coloration in the glass. Moreover, Zhong et al. [59] studied the nature of wetting of molten Duran® glass to different coatings deposited onto Si substrates (NiAl, Ni-Al-N, Ti-B-C, and Ti-B-C-N).

Table 1.1 shows a comparison of the properties of different materials used as GMDs. The benefits of using ceramics are high hardness, oxidation resistance and low CTE, but they show low thermal conductivity and they are very difficult to machine. On other hand, compounds usually have better wear resistance and thermal stability. The main advantages of metals are the lower costs involved and their good machinability, allowing an optimal surface finish of the moulds. However, they generally show poor temperature stability and the contact with the reactive molten glass is detrimental given their low oxidation resistance. The advantageous properties of ceramics and compounds can be transferred to metals by coating them with IMCs possessing high thermal stability, hardness and oxidation resistance, as indicated by the arrows in Table 1.1.

Table 1.1: Comparative graph of the different substrate properties adapted from [55]. The "+" sign indicates an advantage, the "-" a disadvantage and "0" a non-decisive factor. The arrows show metal properties of metal that could be enhanced by coating with intermetallic materials, e.g. RuAl.

Relevant substrate Properties	Ceramics	Metals	Compounds
Hardness	(+) →	-	-
Fracture toughness	-	+	0
Compressive strength	0	-	0
Oxidation resistance	(+) →	-	0
Wear resistance	+	0	← (+)
Temperature stability	0	-	← (+)
Thermal shock resistance	-	0	0
Thermal conductivity	-	+	0
Thermal expansion coefficient	(+) →	-	+
Machinability	-	+	-

For all the reasons previously mentioned, RuAl IMC is here proposed as potential candidate for GMD protective coatings. Due to its high melting point (2060 °C), it offers high thermal stability and oxidation resistance [61]. The last is provided by the growth of a protective α-Al_2O_3 layer, which

possesses a CTE of approximately the same value than that of RuAl ($\alpha \approx 5 \times 10^{-6}$ K^{-1} and $\alpha \approx 6.6 \times 10^{-6}$ K^{-1} for Al_2O_3 and RuAl, respectively) [46]. A minimum mismatch in the CTE between RuAl and a wide variety of glasses (i.e. 3×10^{-6}/K for borosilicate glass) is another advantage of this compound. This is due to the minimisation in stress generation in the glass during the fabrication process, which avoids variations in the refraction index of the lenses.

1.4. Objectives of this thesis

Single-phase RuAl is a suitable candidate material to be used as a protective coating in applications that demand oxidation resistance. Since no concentrated efforts have been so far made on studying the possibility of using RuAl IMC as thin films or coatings in technological applications, it is of high interest to analyse the thermal and oxidation properties of RuAl thin films and their capability to coat different technically relevant substrates. The principal objectives of this work are detailed as follows:

- Find the deposition parameters to obtain an adequate Ru-Al multilayer sequence, in order to form single-phase RuAl during a subsequent annealing and to avoid the formation of other intermetallic phases. The improvement of the film/substrate adhesion is another challenge to overcome.
- The thermal stability of thin films could differ with respect to their bulk counterpart and a film/substrate interaction might even take place at high temperatures. The RuAl phase stability, grain growth mechanisms and the role of impurities and grain orientation on the growth inhibition will be studied and discussed within this work.
- Intermetallic thin films usually show different oxidation rates compared to those of bulk materials, due to their nanocrystalline nature and high density of structural defects. The oxidation behaviour of the RuAl films and the oxide stability will be studied performing microstructure, kinetics and stress analyses.
- The presence of impurities or reactive elements can alter the oxidation rate and the nature of the oxides formed at the surface. The influence of such impurities on the oxidation kinetics and the morphology, the adhesion and stability of the oxide scale will be studied and correlated to the oxidation behaviour of impurity-free RuAl films. Stainless steel and Al_2O_3 will be employed as substrates in order to study the influence of the impurity content in the oxidation behaviour of RuAl films.
- In the context of the application of RuAl films as working layers in GMDs, the wettability and adherence of glass to the intermetallic phase will be analysed by measuring the contact angle between molten glass and the RuAl film at high temperatures.

1.5. Organization of the present work

The first part of the present work describes the principles of the physical vapour deposition techniques (**Chapter 2**) and the methods used for the microstructural and phase characterisation (**Chapter 3**). C**hapters 4** to **7** describe the *results* obtained during the development of the different studies and their corresponding *discussions*. Each chapter contains a brief theoretical introduction, the experimental parameters used for the corresponding tests, discussion of the results and conclusions. They will appear in the following order: first, the synthesis and characterisation of the as-sputtered and annealed samples (**Chapter 4**); followed by thermal stability and grain growth analysis (**Chapter 5**); next, the oxidation behaviour studies (**Chapter 6**) and finally, the wettability and contact angle measurements (**Chapter 7**). The last part of this work presents a summary with the most important results and the global conclusions.

2

Deposition techniques

2.1. Physical Vapour Deposition techniques (PVD)

Physical vapour deposition (PVD) techniques involve the creation of several vapour-phase species (by evaporation, sputtering or laser ablation), the transfer of the evaporated material on the atomic level and its subsequent condensation onto a substrate. The vaporised species are transported from the source to the substrate (with or without collisions between atoms and molecules), where they condense, resulting on the formation of the film by nucleation and growth process. PVD processes are used to deposit films with thicknesses going from a few nanometres up to several micrometres. They can also be used to produce multilayer coatings or deposits with a graded composition [62].

2.1.1. Sputtering

Sputtering is a non-thermal vaporisation process in which surface atoms are physically ejected from a solid by momentum transfer from an energetic bombarding particle, which is usually a gaseous ion accelerated from a plasma [63]. The particles ejected in this process are predominantly neutral atoms. The capability of depositing alloys and insulators as composite materials is an important benefit of sputtering.

The ions formed in the plasma are accelerated towards a target (of the material to be deposited), eroding it via energy transfer, resulting in the ejection of neutral particles. These travel through the plasma colliding with other particles or surfaces. If a substrate is placed in the path of these ejected particles, it will be coated by a thin film of the target material [63]. Depending on the configuration, the substrate and the growing film may be subjected to low energy bombardment from accelerated

host species or noble gas ions, which can play an important role in determining the nucleation and growth kinetics of the film [64]. Figure 2.1a shows the sputtering process.

This deposition technique can use DC glow discharges or RF discharges. DC discharges impose the limitation that the electrodes have to be conductive; whereas RF discharge can be used to sputter insulating materials. Because of the lower pressure operating during RF sputtering, the material ejected from the target arrives at the substrate with more energy than in the DC case because of fewer collisions [64].

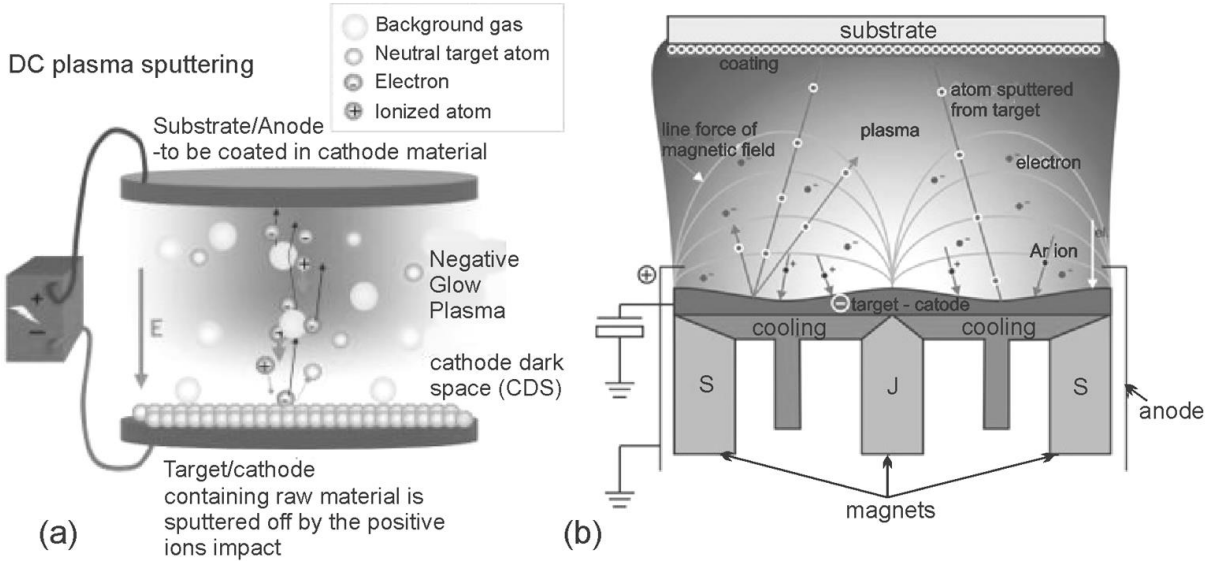

Figure 2.1: schematic representation of (a) the sputter deposition technique[2] and (b) the magnetron sputtering configuration[3].

2.1.1.1. Magnetron sputtering

The sputtering rate (max. 1000 Å/min for metals) in DC and RF sputtering can be increased with the assistance of a magnetic field, which enhances the efficiency of the electrons near the target in creating ions [64]. By applying a magnetic field parallel to the cathode surface, free electrons become trapped and the motion of primary electrons is restricted to the vicinity of the cathode, increasing the probability of ionizing a neutral gas molecule by several orders of magnitude. This increases the target erosion rate and the subsequent deposition onto the substrate. The application of an axial magnetic field in a planar diode glow discharge system increases the electron path length by forcing longer helical orbits for the electrons to reach the anode. The electrons are trapped close to the target as a result of the combined effect of the electric and magnetic fields, increasing their ionising effect. Moreover, the magnetic field reduces the loss of electrons due to recombination processes at the walls [62]. Magnetrons are cold cathode discharge devices, which use magnetic fields to trap electrons at the cathode surface. The perpendicular configuration of $\vec{E}$ and $\vec{B}$ produces

2) Image from: *http://www.etafilm.com.tw/PVD_Sputtering_Deposition.html*
3) Image from: *http://www.arzuffisrl.it/eng/sputtering.htm*

closed electron drift currents. Primary electrons which leave the cathode and enter the plasma are trapped in the magnetic field and the plasma is confined above the cathode in annular rings [65] (Figure 2.1b). Magnetrons greatly enhance the capability of the sputtering process by increasing the ionization rate by a factor of 10 over conventional diode targets, resulting in faster deposition rates at lower pressure.

2.2. Microstructure as a function of deposition parameters

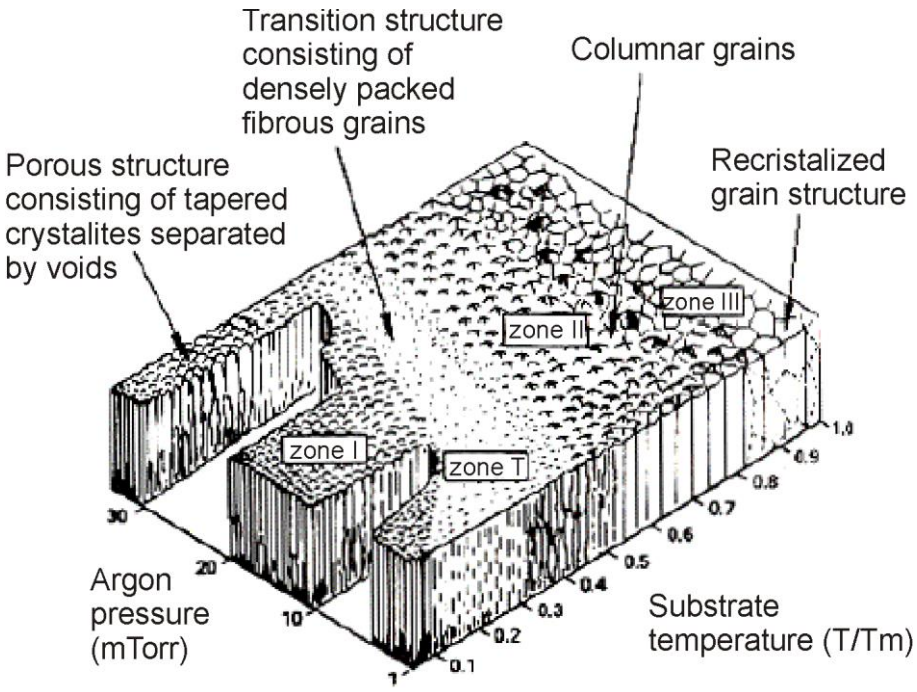

Figure 2.2: Structure zone model for film growth proposed by Thornton for sputtered metal coatings. T_s is the substrate temperature and T_m is the melting point of the coating material [64].

Thornton has reviewed and summarised the most recent understanding of film microstructure formed from deposition techniques. Figure 2.2 shows the structure zone model (SMZ) proposed by Thornton, which predicts the morphology and microstructure of a film, independently of its material, as a function of the adatom mobility, which is related to the Ar pressure and substrate temperature [64]. At low deposition temperature ($T_s/T_m < 0.3$) a fine-grained structure of fibrous grains is expected, containing a high density of lattice imperfections and porous GB. This growth is due to the continuous nucleation of grains as a consequence of the low adatom mobility (zone I). For the temperature range $0.3 \leq T_s/T_m \leq 0.5$, the growth of columnar grains is observed and they may extend through the film thickness (zone II). In zone III ($T_s/T_m > 0.5$) the columnar grains have grown in width by bulk diffusion or recrystallisation. A transition zone (zone T) between zone I and zone II has been added by Thornton [64], where the bombardment-induced mobility during the sputtering was also considered as a function of the gas pressure.

3

Methods for microstructural and phase characterisation

3.1. Scanning Electron Microscopy/Focused Ion Beam (SEM/FIB) dual beam system

A scanning electron microscope (SEM) uses a focused electron beam to produce images by scanning the sample surface. The electron beam interacts with the atoms in the specimen, which respond producing different signals containing information about the sample topography and composition. A focused ion beam microscope (FIB) has similar operation principles to those of a SEM, but uses ions instead of electrons (see Figure 3.1). For the microstructural analysis of the samples, a ***FEI Helios NanoLab 600 DualBeam*** work station was used. The Dual-Beam system includes both an e^- and a Ga ion column. Both beams operate independently and can be focused onto the same point in space. This equipment also allows chemical composition analysis by using an energy dispersive X-ray spectroscopy (EDX from EDAX) detector; phase and orientation analysis using electron backscattered diffraction (EBSD, see 3.1.1); and site-specific TEM foil preparation by ion milling of the samples (see 3.1.3).

SEM images were acquired using a 5 keV electron beam with 1.4 nA current, showing resolutions of few nanometers (~3-4 nm). For high-resolution images, a *through-the-lens detector* (TLD) was used for highest collection efficiency of *secondary electrons* (SE). EDX measurements were made using a 15 keV and 30 keV electron energy, when measuring at the surface of the sample and in TEM foils, respectively. The K-lines from aluminium and L-lines from ruthenium were acquired and a ZAF-

corrected quantification was performed, using the *EDAX-Genesis* software. The ion beam can be focused to a size as small as 10 nm. For machining, the Ga ions are accelerated towards the specimen at 30 keV, causing a fast sputtering of the sample.

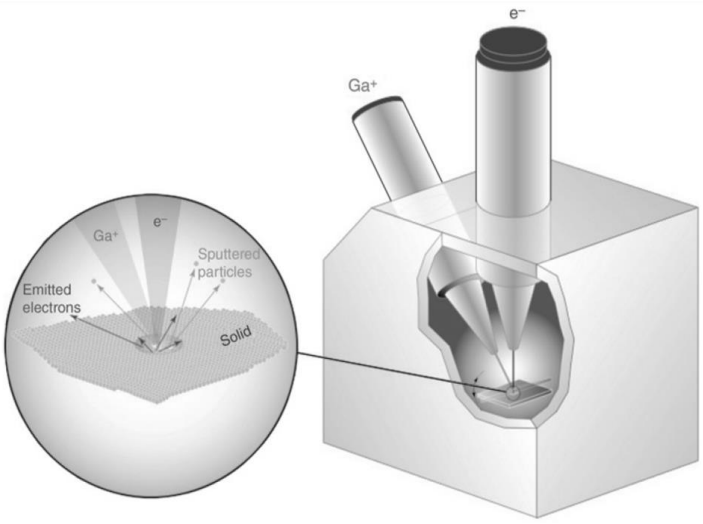

Figure 3.1: Schematic illustration of a dual beam FIB/SEM instrument. The amplified image shows the interaction of the electron and ion beams with the sample[4].

3.1.1. Electron backscatter diffraction (EBSD)

EBSD was used to obtain quantitative information of phase, orientation and size of individual grains. The information obtained with EBSD comes from a very shallow depth in the material (10 to 20nm) [66], allowing a surface analysis which shows 2D distributions of crystal orientations.

The electron beam strikes (15 keV) the crystalline sample (at 70° angle) and the diffracted electrons form a pattern on a phosphor screen, as indicated in Figure 3.2. The step size was 20 nm. The obtained pattern consists of the denominated Kikuchi bands and is characteristic of the crystal structure and orientation of the sample region from which it was generated. The primary electrons are inelastically scattered by the atoms in the material, forming a divergent source of electrons close to the surface of the sample. The electrons which satisfy the Bragg condition (see 3.2) diffract forming paired high-angle cones, corresponding to each diffracting plane, which will create the characteristic Kikuchi bands at the intersection with the phosphor screen as shown in Figure 3.2. Each Kikuchi band is then indexed according to their Miller indices and analysed with the help of the OIM 5.3 analysis software provided by EDAX.

Two different filters, cleanup (confidence index, *CI,* standardisation) and the removal of point with CI <0.09, were applied to the diffraction patterns for their correction prior the grain size and texture analysis. Furthermore, the grains intersecting the measurement window were automatically excluded from the analysis.

4) Image from: *MRS bulletin, vol. 32 – May 2007 - www/mrs.org/bulletin*

Figure 3.2: Schematic EBSD measurement configuration (left[5]) and formation of the Kikuchi patterns (right) [67].

3.1.2. Scanning transmission electron microscopy (STEM)

In STEM, a narrow, focused electron beam scans the surface of a sufficiently thin specimen. Transmitted electrons reach a detector placed at the bottom of the microscope column, where the image is formed. For this technique, *electron-transparent* samples are needed (thickness <100 nm). The specimens were prepared using FIB, in the workstation previously mentioned (see 3.1.3). In this work, low-voltage (30 kV) STEM was performed in a SEM using a multisegment STEM detector, which allows bright-field (BF), dark-field (DF) and high-angle annular dark-field (HAADF) imaging. Figure 3.3 shows the geometric arrangement of the different detectors.

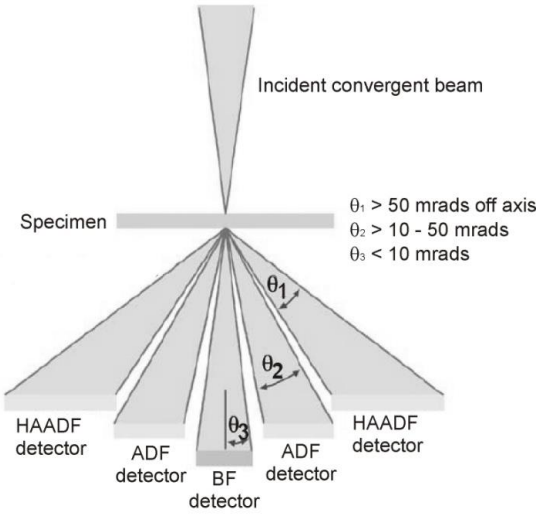

Figure 3.3: Geometric arrangement of bright field, angular dark field and high angle angular dark field detectors [68].

5) Graphic from EDAX web site: *www.edax.com/Products/EBSD/TEAM-EBSD-Analysis-System.aspx*

3.1.3. TEM sample preparation using the dual beam system

S/TEM samples with thicknesses t < 100 nm were prepared using the dual beam system (see 3.1). The sample was extracted from selected specific locations and specimens with a "transparent" area of about 40 to 50 μm^2 were fabricated, including interfaces composed of very dissimilar materials.

Prior to the milling process, a platinum protective layer (~1 µm e^- Pt and ~1 µm ion Pt) was deposited onto the region of interest of the sample in order to prevent the erosion of its surface by the ion beam. The machining of the sample was performed using an automatic-running wizard (FEI company),then, the specimen was lifted out using an *OmniProbe 200* micromanipulator and attached to a Cu grid which allows the transport to the TEM or STEM devices. The specimen was thinned once the sample is on the grid until achieving electron-transparency, using Ga^+ ions (30 kV) and 44, 28, 0.96 and 0.48 nA. A final FIB milling was performed using 5 keV ion beam in order to relieve possible accumulated stresses. Figure 3.4 shows the different stages of a TEM sample preparation.

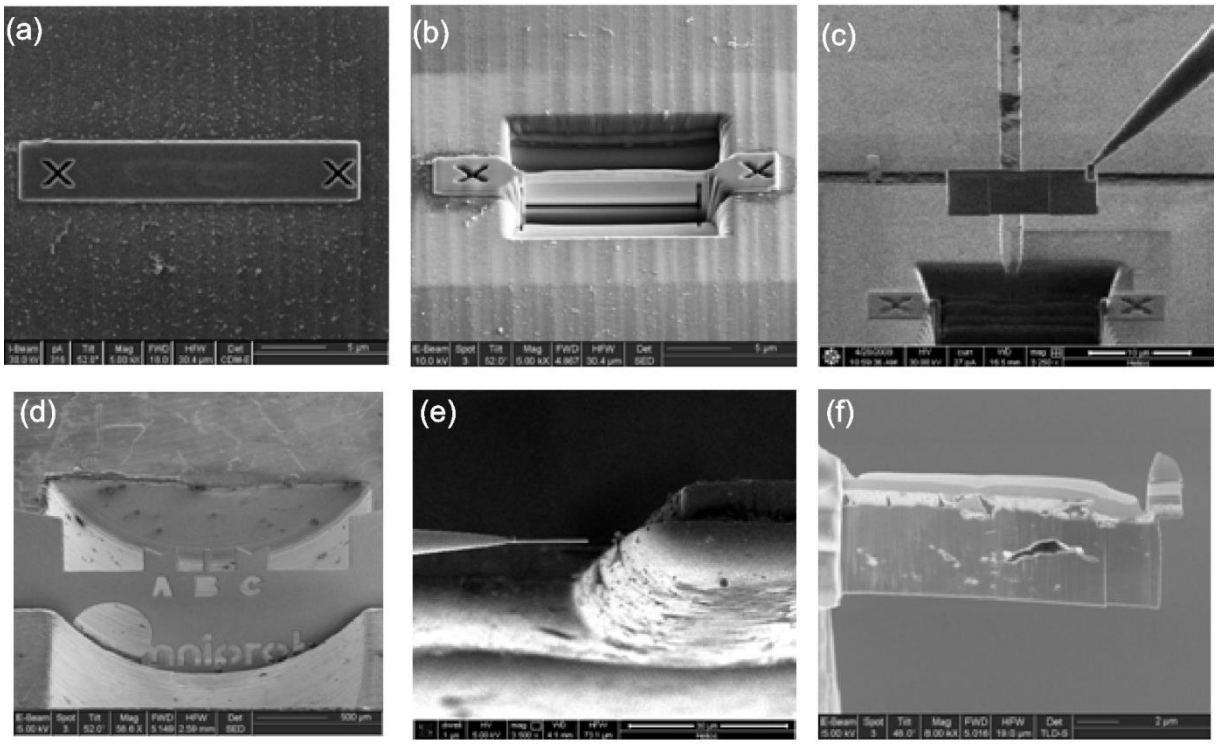

Figure 3.4: Stages of the TEM sample preparation. The figure shows (a) the surface protected by a Pt layer; (b) the milled front and back section of the TEM sample; (c, d, e) the transport using a micromanipulator and the subsequent joining to the Cu grid; and (f) the milled sample.

3.2. X-Ray Diffraction (XRD)

XRD allows the characterisation of the periodic atomic structure of crystalline materials by the diffraction of a focused beam of monochromatic X-rays at their surfaces. The wave scattering is produced by the atom arrangement, forming a constructive interference when the Bragg's

condition is fulfilled. Equation 3.1 represents Bragg's law, where d is the spacing between diffracting planes, θ is the incidence angle of the beam, n is an integer and λ is the X-ray wavelength. Figure 3.5 illustrates the process.

$$2d_{hkl}\, sin\, \theta_{hkl} = n\lambda \qquad (3.1)$$

XRD was used to analyse the crystal structure of the bulk substrates and the RuAl thin film crystals. Texture and residual stresses in the films were also analysed using this technique. In this work, ***PANalytical X´Pert Pro MPD*** and ***PANalytical X´Pert Pro MRD*** difractometres were used for phase and stress analysis, respectively. Furthermore, XRD measurements were performed in non-ambient conditions (at high-temperature, in vacuum, etc.) in an Anton Paar HTK 1200N chamber, mounted in the former. This allowed the study of dynamic processes such as reactions involving solid state reactions, phase transitions and crystallite growth.

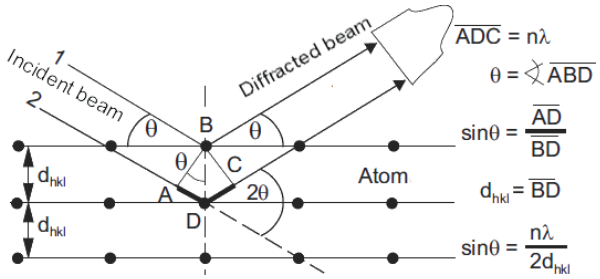

Figure 3.5: X-ray beam showing constructive interference after the interaction with a periodic arrangement of atoms.

3.2.1. Grazing-incidence XRD (GI-XRD)

This method was employed to measure the RuAl films using a low incidence angle (ω = 1°) while the detector was scanned over the 2θ-range of interest (see Figure 3.6). The measured effective volume is then confined to a relatively small volume adjacent to the surface of the sample, where the higher diffraction intensities originate, avoiding (or at least minimising) the signal from the substrate (in coated samples). Using this configuration, not only the crystal planes oriented parallel to the surface will achieve the Bragg's condition, but also those with other directionality [69,70].

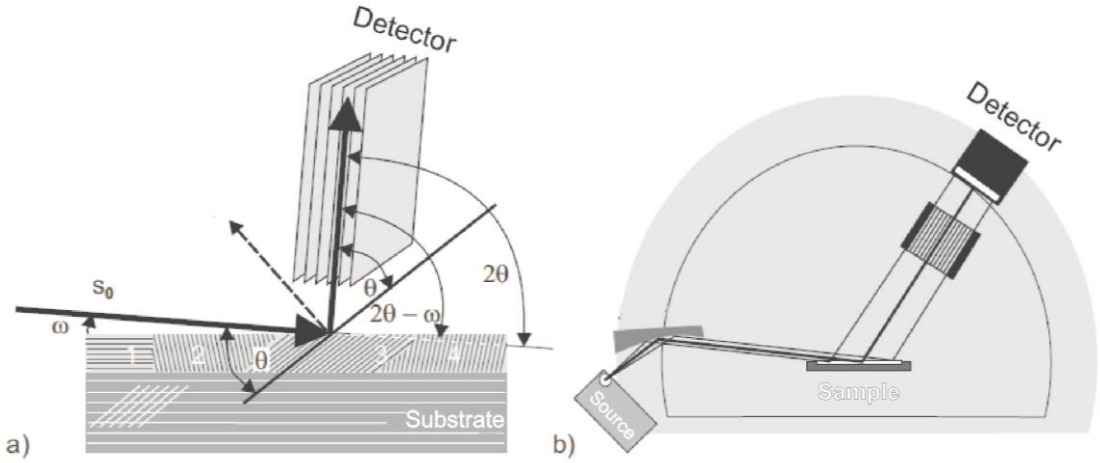

Figure 3.6: Grazing incidence configuration for measurement of thin films [69].

3.2.2. Residual stresses

Stresses in the crystal structure are determined by measuring the variation in the lattice spacing for a series of {hkl} planes. The lattice spacing depends on the crystallite orientation with respect to the specimen frame reference. The elastic strain of determined {hkl} planes can be calculated from Equation 3.2. In this equation, d_0^{hkl} is the strain-free lattice spacing of the {hkl} lattice planes. The direction of the diffraction vector is represented by the angles φ and ψ, which describe its rotation and inclination, respectively, from the specimen surface normal (Figure 3.7). By using the GI-XRD method, the inclination angle ψ for a set of {hkl} planes is given by $\psi = \theta^{hkl} - \alpha$.

$$\varepsilon^{hkl} = \left(d^{hkl} - d_0^{hkl}\right)/d_0^{hkl} \qquad (3.2)$$

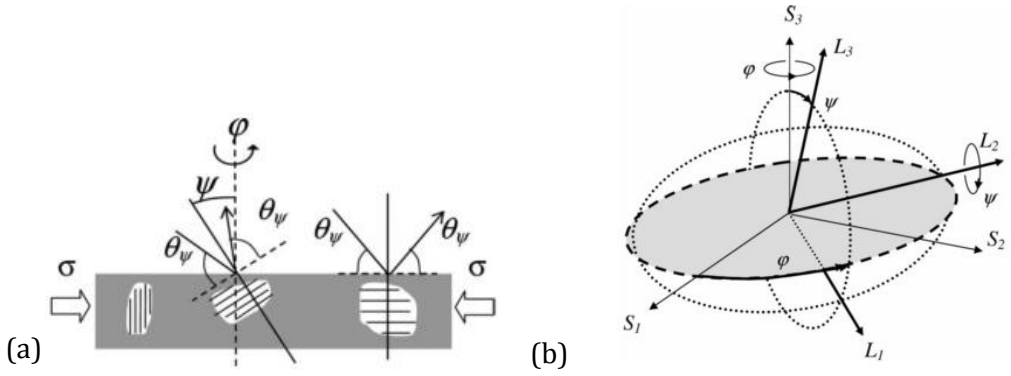

Figure 3.7: a) lattice spacing of the {hkl} planes in a sample subjected to uniaxial stress, changing with the orientation of the lattice planes with respect to the loading direction; b) relation between the sample and the laboratory reference frames [71].

The $\sin^2\psi$ method is used to calculate the material stress. For a rotationally-symmetric biaxial state of stress, the non-zero components of the stress tensor are $\langle\sigma_{11}^S\rangle = \langle\sigma_{22}^S\rangle = \langle\sigma_{\parallel}^S\rangle$ and the stress

perpendicular to the surface is zero. The general strain-stress relation is given by Equation 3.3. In this equation, S_1^{hkl} and $\frac{1}{2}S_2^{hkl}$ are the X-ray elastic constants [71].

$$\varepsilon_{\psi}^{hkl} = \left(S_1^{hkl} + \tfrac{1}{2}S_2^{hkl}\, sin^2\,\psi\right)\langle\sigma_{\parallel}^{S}\rangle \qquad (3.3)$$

Untextured materials normally show a linear dependence between the strain values $\left(\varepsilon_{\psi}^{hkl}\right)$, measured at several ψ angles, and $\sin^2$ ψ. Consequently, the slope of the straight line obtained from the ε_{ψ}^{hkl} plot is used to determine the stress $\langle\sigma_{\parallel}^{S}\rangle$, as shown in Figure 3.8.

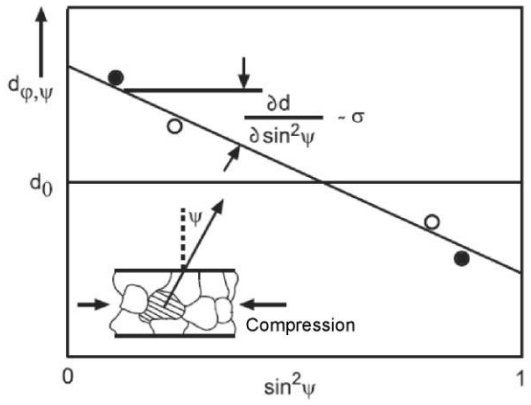

Figure 3.8: Relationship between the lattice spacing *d* with the measured angle(*ψ)* [69].The stress is obtained from the slope of the plot $(d\text{-}d_0)/d_0$ as a function of $\sin^2\psi$.

3.3. Transmission electron microscopy (TEM)

Thin specimens (thickness < 100 nm) prepared using FIB (see 3.1.3) were used for TEM analysis. Operation principles of TEM can be found elsewhere [72,73]. The samples were analysed using a Philips CM200 and a JEOL JEM 2011,both equipped with LaB_6 filament as electron source, with 200 kV. The as-sputtered samples, RuAl films in annealed condition and oxidised samples were analysed by this technique in imaging and diffraction (SAD) modes.

3.4. Atom Probe Tomography

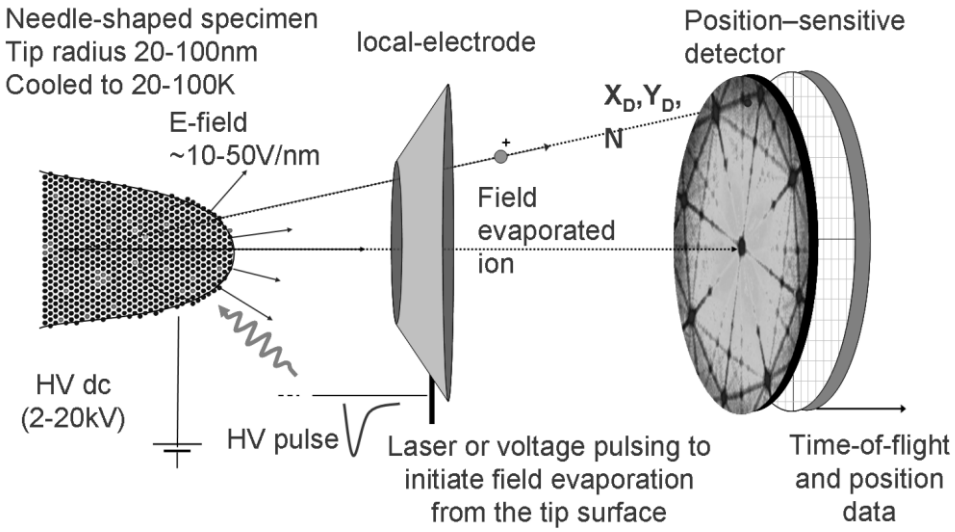

Figure 3.9: Principles of atom probe tomography[6]. The evaporation process occurs by applying a laser or voltage pulse. 3D reconstruction is possible registering x,y coordinated at the position-sensitive detector.

Atom probe tomography (APT) provides three-dimensional analytical mapping of materials with atomic-scale resolution. For this technique, needle-shaped specimens are needed, which are usually prepared using FIB techniques or electropolishing. The specimen is subjected to a standing (DC) electrostatic field combined either with high-voltage or laser pulses that will trigger the evaporation of individual ions. The ions are accelerated stack of microplate channels (MPC) that transform these ions into electrons and amplifies the signal. The electron cascade is then sensed by a delay-line position-sensitive detector that registers not only the position of the impact, but also the time-of-flight of the ions. These data permits to track back the three-dimensional position of the atoms and to know their chemical nature (Figure 3.9). Furthermore, the implementation of a local electrode enables ion evaporation at lower voltages. This configuration improves the measurements by allowing high data collection rate within a large field of view. Another advantage is the shortening of the time of flight, which prevents time-varying fields, and reduces energy, enhancing the spectrum's mass resolution [74].

The multilayer morphology of the as-deposited samples and the impurity content and distribution in the oxidised films were analysed using a pulsed-laser assisted APT CAMECA™ LEAP 3000 XHR system with green light laser (wavelength 532 nm). The laser pulsing frequency was 100 kHz, with 0.4 nJ energy. The data analysis was made using IVAS™ 3.6.6 software with a standard reconstruction algorithm developed by Bas et al. [75]. The needle-shape specimens were prepared using FIB according to [76] with a 2 kV final polishing.

6) Image from: *http://atomprobe.materials.ox.ac.uk/*.

3.5. Grain size determination

3.5.1. Warren-Averbach XRD technique

The Warren-Averbach (W-A) method for peak shape analysis enables the separation of size and stress contributions to the diffraction peak broadening, by expressing the Bragg-peak line profile as a Fourier series. The mathematical treatment behind the method is detailed elsewhere [77,78]. In this paragraph, the main results for the peak analysis are presented, which are expressed in terms of a Fourier sum, as showed in Equation 3.4.

$$\boldsymbol{f(s) \propto \sum_{L=-\infty}^{\infty}\{A(L)\,cos[2\pi(s-s_0)L] + B(L)sin[2\pi(s-s_0)L]\}} \qquad (3.4)$$

Where A and B are the Fourier coefficients*; L (equal to nλ/[2(sinθ₁-sinθ₂)])* is interpreted as the length of the column of unit cells perpendicular to the diffracting planes corresponding to the Bragg peak. The coefficient *A(L)* can be written as $A(L) = A^{size}(L) \times A^{strain}(L)$. The size component depends on the length of the column but not on the diffraction order, while the strain component does and is given by $A^{strain}(L) = exp(-2\pi^2L^2g^2\langle\varepsilon^2_{g,L}\rangle)$, being g the diffraction vector [77,78].

3.5.2. Image analysis grain size determination

For the grain size determination, the grain boundaries of the sample from STEM images were digitally reconstructed using the *Aquinto-A4i* software. The images were binarised, followed by the application of the Euclidean distance transformation (EDT) and watershed filters. In this way, the grain boundary reconstruction as shown in Figure 3.10 was obtained. Then, the average grain size was calculated measuring the mean Feret, which is defined as the distance between two parallel tangents to the contour of the particle in a defined orientation, as indicated in Figure 3.11. The mean Feret measured by the A4i software is the mean value obtained from measuring the Feret over 36 different directions, simultaneously obtaining the grain size distribution.

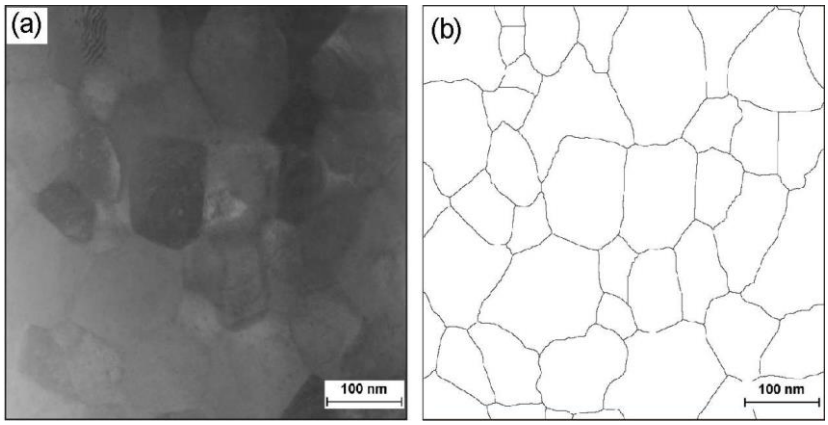

Figure 3.10: (a) STEM image of an annealed sample at 750 °C for 3 h and (b) its grain boundary reconstruction using the software A4i.

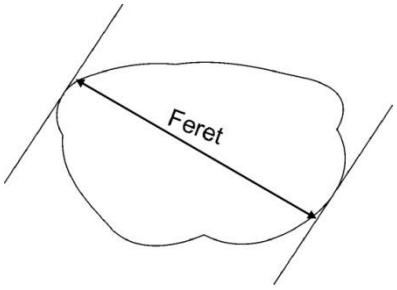

Figure 3.11: feret is defined as the distance between two tangents to the contour of the particle**.**

3.6. Film/substrate adhesion

The American Society for Testing and Materials (ASTM) defines adhesion as the "condition in which two surfaces are held together either by valence forces or by mechanical anchoring or by both together" (ASTM D907-70). The adhesion failure is the separation of the materials at or near the interface over a large area, usually under stress.

Adhesion can be classified in three different modes [79]:

- *Fundamental adhesion*: it is defined as the sum of all molecular and atomic interactions across the interface between the coating and the substrate material.
- *Thermodynamic adhesion*: it describes the change in free energy when an interface is formed.
- *Practical adhesion*: it is described as the force required to remove or detach the coating from the underlying substrate, independently of the location of the failure.

Practical adhesion is the most interesting since it is the only one which can be experimentally measured. The most used technique for measuring coating adhesion is the *scratch test,* which is a semi-quantitative analysis. It is a comparative test in which the critical loads, at which failures appear, are used to evaluate the relative cohesive or adhesive properties of a coating.

During the scratch adhesion testing, a diamond tip is drawn across the coated surface at a constant velocity and with an increasing normal load, resulting in various types of failure at specific critical loads. In the present work, the adhesion of the RuAl to SS was evaluated using a CSM nano-scratch tester possessing a 2 μm Rockwell diamond pin. The initial normal load was 2 mN, being increased up to 100 and 130 mN for two RuAl layer thicknesses (650 and 1200 nm, respectively). The scratch length was 4 mm and the failure in the films was evaluated by means microscopic observations (optical microscopy and SEM). In this way, the critical load, L_c, is identified as the minimum load at which coating damage was observed. Figure 3.12 shows the common operation mode of a scratch adhesion tester.

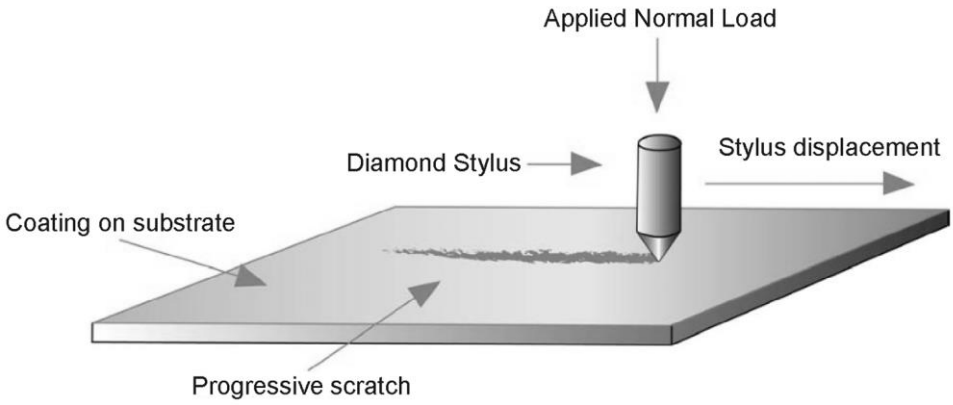

Figure 3.12: Scratch testing apparatus. A diamond tip is drawn across the coated surface with an increasing normal load. The film failure is detected by using load cells, acoustic emission and observation with optical microscope.

The scratch test does not directly measure the adhesion, but rather the load required for the disruption of the coated specimen at the interface or in the interfacial region. Scratch testing is combined with examination of the scratch track and the surface morphology in its vicinity by optical and scanning electron microscopy [62]. A detailed description of failure modes during scratch tests is given by Burnett and Rickbery and by Bull [80,81].

4

Synthesis and characterisation of RuAl thin films

The present chapter details the steps for the synthesis of single-phase RuAl thin films starting from Ru and Al multilayers (ML) with very small periods (<4 nm). The microstructural characterisation of both the as sputtered Ru/Al MLs and the annealed samples are also included. Austenitic stainless steel (SS) was selected as substrate due to its technical relevance, since it is frequently used as a moulding material in the production of precision lenses [58,82].

This chapter incorporates a detailed study of the RuAl phase formation by in-situ high-temperature X-ray diffraction (HT-XRD) measurements during the annealing process. Moreover, the ML morphology and chemistry was locally analysed, in a cross-sectional view, using atom probe tomography (APT). Transmission electron microscopy (TEM) and scanning TEM (STEM) were also used to analyse the MLs and annealed samples. Additionally, the effect on the film/substrate adhesion of sputter cleaning the substrate and adding a metallic adhesion-layer was evaluated by nano-scratch tests.

The results exposed in the present chapter have been submitted for publication to the *Surface & Coatings Technology* journal ("*Production of single-phase intermetallic films from Ru-Al multilayers*" - Guitar, Pauly, Aboulfadl, Leibenguth, Migot, Mücklich, 2013).

4.1. Introduction

The properties (i.e. mechanical properties, oxidation behaviour, etc.) of intermetallic materials are strongly dependent on the chemical composition and stoichiometry, which are linked to the type

and amount of constitutional defects [18]. By depositing the constituents as MLs and varying the thickness of each individual layer, it is possible to control the final composition of the desired intermetallic phase [3,83,84]. Previous studies [3,4] have demonstrated that the direct formation of single-phase RuAl from MLs during annealing is highly dependent on the ML period. For small periods (<4.5 nm) the transformation to the single phase is direct. In this work, Ru and Al were deposited sequentially by using a modified deposition process in order to obtain MLs with periods in the order of 2-3 nm. A posterior annealing step of the as-deposited MLs films is generally required to obtain the desired equilibrium compound as previously observed for RuAl and other intermetallic compounds such as NiAl and FeAl [3,83,84].

A satisfactory coating system requires excellent adhesion to the underlying alloy substrate and limited interdiffusion between them, avoiding the formation of depletion zones and/or brittle phases. The film/substrate adhesion is in many cases the limiting factor for a wider use of coatings and it represents the basic requirement for the durability and performance of any coated component. The adhesion improvement methods usually include *sputter-cleaning* and/or *deposition of metallic adhesion layers*, where Ti is mostly used.

4.2. Results and discussion

4.2.1. RuAl thin film synthesis

In order to deposit Ru and Al ML with very small periods, a modified deposition process was employed using a PVD magnetron sputtering. This device offers the possibility to ignite the plasma simultaneously under both targets. Thus, by rotating the sample from target to target it is possible to deposit alternated layers of Ru and Al in a reduced period of time. A schematic representation of this periodic deposition process is shown in Figure 4.1. A subsequent annealing step of the as-deposited MLs is required in order to obtain the desired equilibrium compound.

The RuAl thin films, with a total thickness of 650 nm, were deposited by AC/DC magnetron sputtering using a Von Ardenne PPS-A 200 source. High-purity (99.99%) Al and (99.9%) Ru targets were used, together with 15 mm x 15 mm AISI 316L SS substrates. These presented a mirror polished surface and were cleaned in an ultrasound bath with ethanol during 60 seconds, prior to their introduction into the PVD chamber. The sputtering parameters are listed in Table 4.1.

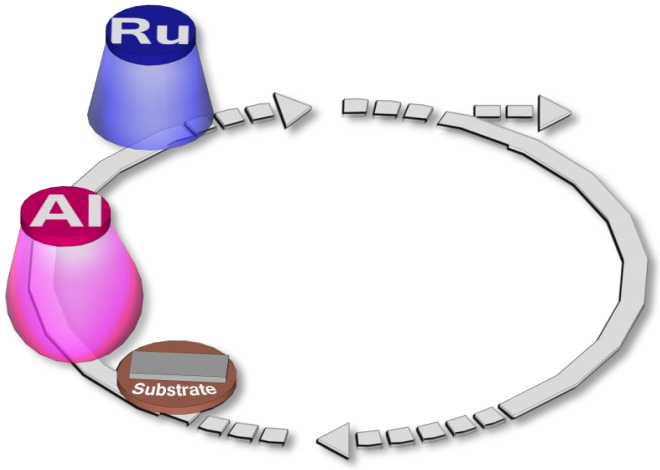

Figure 4.1: Schematic representation of the periodic deposition. The plasma under the Al and Ru targets can be simultaneously ignited and by rotating the samples, it is possible deposit alternating layers of Ru and Al. This technique allows for a periodic deposition of Ru and Al films, with thickness of 1-2 nm, each.

Table 4.1: Deposition parameters for achieving 1:1 atomic ratio of stoichiometric RuAl.

Sputtering targets	Al	Ru
Purity	99.99%	99.9%
Current type	AC	DC
Power density	2.07 W/cm^2	0.62 W/cm^2
Target to substrate distance	65 mm	
Base pressure	10^{-7} mbar	
Ar flow	80 sccm	
Sputtering pressure	3 x 10^{-3} mbar	
Substrate plate rotation	4 rpm	

4.2.2. Microstructural characterisation of the as-deposited (Ru-Al ML) films

Sequential deposition of Al and Ru results in the growth of very thin Ru/Al ML, with thickness up to 2 nm, as shown in the TEM image of Figure 4.2. The grazing-incidence XRD diffractogram (GI-XRD) of Figure 4.3 shows a broad peak at about 29° (2θ) which can be related to the presence of the RuAl phase. Moreover, the broad and asymmetric peak at about 42-43° (2θ) might be the consequence of the superposition of Al, Ru and/or RuAl peaks. The individual identification of each peak is difficult due to the principal peaks for Al, Ru and/or $RuAl_x$ overlapping. XRD peak broadening has been related in the literature [3] with a Λ-disorder and changes in the d-spacing of the Ru and Al layers in MLs with $\Lambda \leq 4.5$ nm. The Λ disorder suggests chemical interaction at the Ru/Al and Al/Ru interfaces during the deposition process.

Selected area diffraction (SAD) performed during the TEM analysis of the MLs (Figure 4.2) shows diffraction rings as associated with Ru, Al and RuAl phases. Broadening of the Al-{200} diffraction

ring might be, as mentioned before for XRD analysis, an effect of the interdiffusion of Ru and Al at the Ru/Al and Al/Ru interfaces. Broadening of the SAD diffraction ring has been related in [85]with an Al-Ru icosahedral phase possessing about 18.5 at.% Ru, formed during the reaction of Al-Ru MLs. However, there is insufficient evidence in this work to relate the broadening of the Al reflection with the formation of a new phase at the Al-Ru interface.

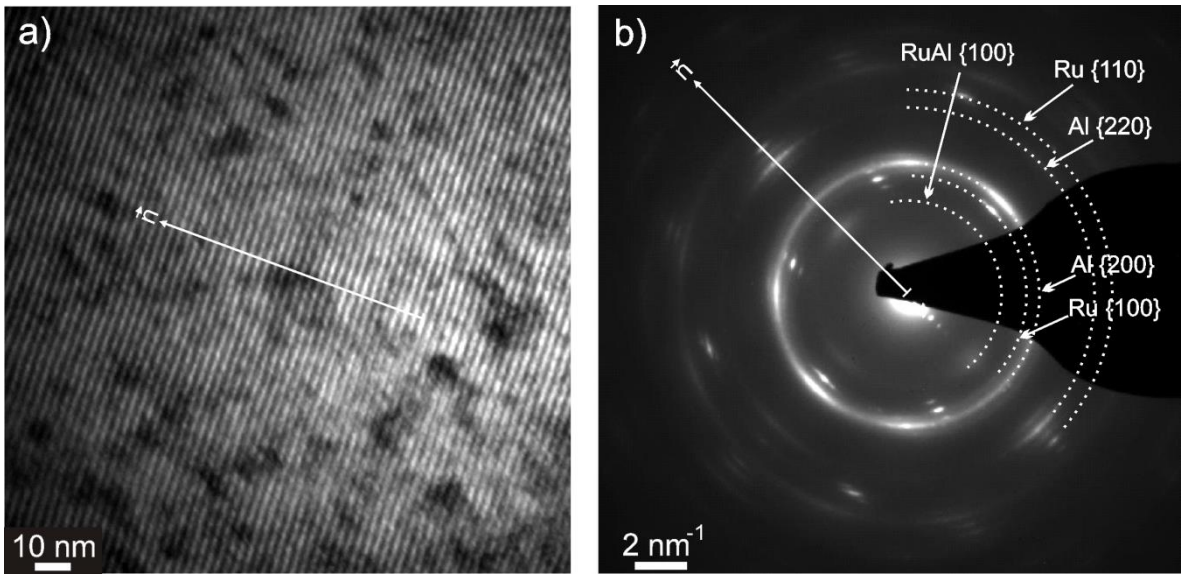

Figure 4.2: a) Cross-section TEM micrograph of the multilayer morphology of an as-sputtered sample with individual ~1.5 nm thick Ru and Al layers of. The darker areas likely correspond to reaction or interdiffusion zones. b) SAD patterns (*Philips CM200*) of the MLs. The reflections of Ru, Al and RuAl phases are identified with dotted lines.

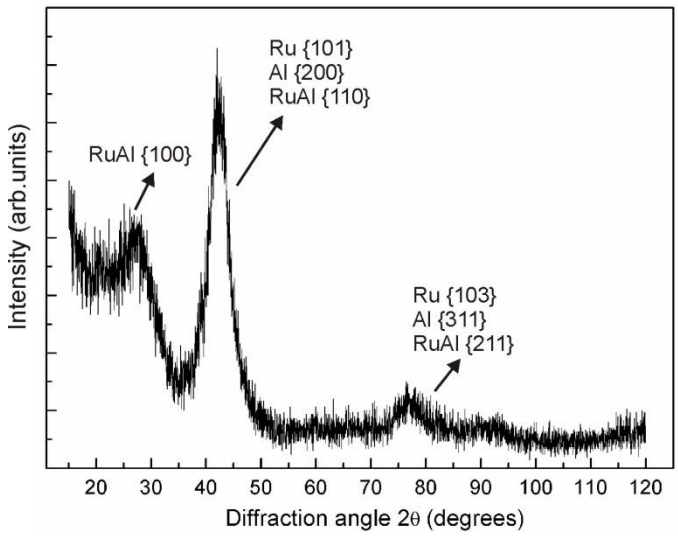

Figure 4.3: GI-XRD patterns from the as-sputtered sample. The diffractogram was corrected for substrate scattering by subtracting the background intensity.

From the XRD and TEM analysis, it seems that reaction and interdiffusion zones are present in the as-deposited films. APT was used to investigate this, providing higher-magnification images of the

ML structure. During the measurements, the electric field on the specimen tips fluctuated gradually during the field evaporation of each individual Al and Ru layer, given the strong difference in field evaporation rates (19 and 41 V/nm, respectively [86]). Since the depth reconstruction procedure in the standard reconstruction algorithm assumes a homogenous evaporation from the tip surface, variations in the calculated local atomic densities along the interfaces are induced in the reconstruction, originating from the inhomogeneous field distribution on the tip surface [87]. Nevertheless, these artefacts do not impede the eventual detection of intermixed regions within the MLs, which was the goal of the study. As seen in Figure 4.4b, some parts of the reconstruction show regions of intermixed Ru-Al, which have about 3 at.% off-stochiometric compositions compared to the ordered ML regions. As explained by Vurpillot et al. [88], the local magnification effects observed during the reconstruction of MLs is induced by spatial distribution errors for two different elements (i.e. Ru and Al), which can lead to biased compositional measurements along the interfaces. However, the overall chemical composition of the individual layers should not be affected by the inhomogeneous field-evaporation rates. Therefore, we can confirm that the overall compositional difference between the ordered and intermixed regions indicates the formation of a different phase.

From APT analysis, the overall composition of the ordered regions have shown a slight Ru enrichment (~53 at.% Ru), which is in agreement with preliminary EDX measurements performed on STEM foils. The intermixed zone showed a $Ru_{0.54}$-$Al_{0.46}$ composition. Despite the deviation from stoichiometry [2], this region might correspond to the RuAl phase identified in XRD and SAD.

The high interdiffusion in the MLs, observed on the right part of Figure 4.4b, might be consequence of many factors. The Ar plasma generated in front of each target material shows different characteristics. That of the Al target (RF discharge) is very energetic and spreads over a large part of the chamber partially overlapping the Ar plasma generated by the DC discharge of the Ru target. Consequently, a region of co-deposition is created between both targets, given the high-spatial distribution of the sputtered material, principally that of Al [63]. The continuous rotation of the substrate holder, passing sequentially under the Al and Ru targets, generates the microstructure previously described. Co-sputtering of Ni/Al has shown the formation of a B2-NiAl phase when performed at RT [26], whereas other authors [83] detected B2-NiAl with a fraction of amorphous phase, using the same process. This is in accordance with the APT observations in the as-sputtered Ru-Al samples studied here. Additionally, Al atoms arriving at the substrate during the Ru-Al deposition are highly energetic[7] and possess a higher mobility than Ru atoms [89]. This allows the

7) The energy of Al atoms is much higher than that of Ru, due to the higher power of the RF (650W) plasma sputtering the Al target, with respect to the DC plasma (200 W) used for the Ru.

former to accommodate and diffuse, even when the sample temperature during the deposition does not exceed 80-100 °C.

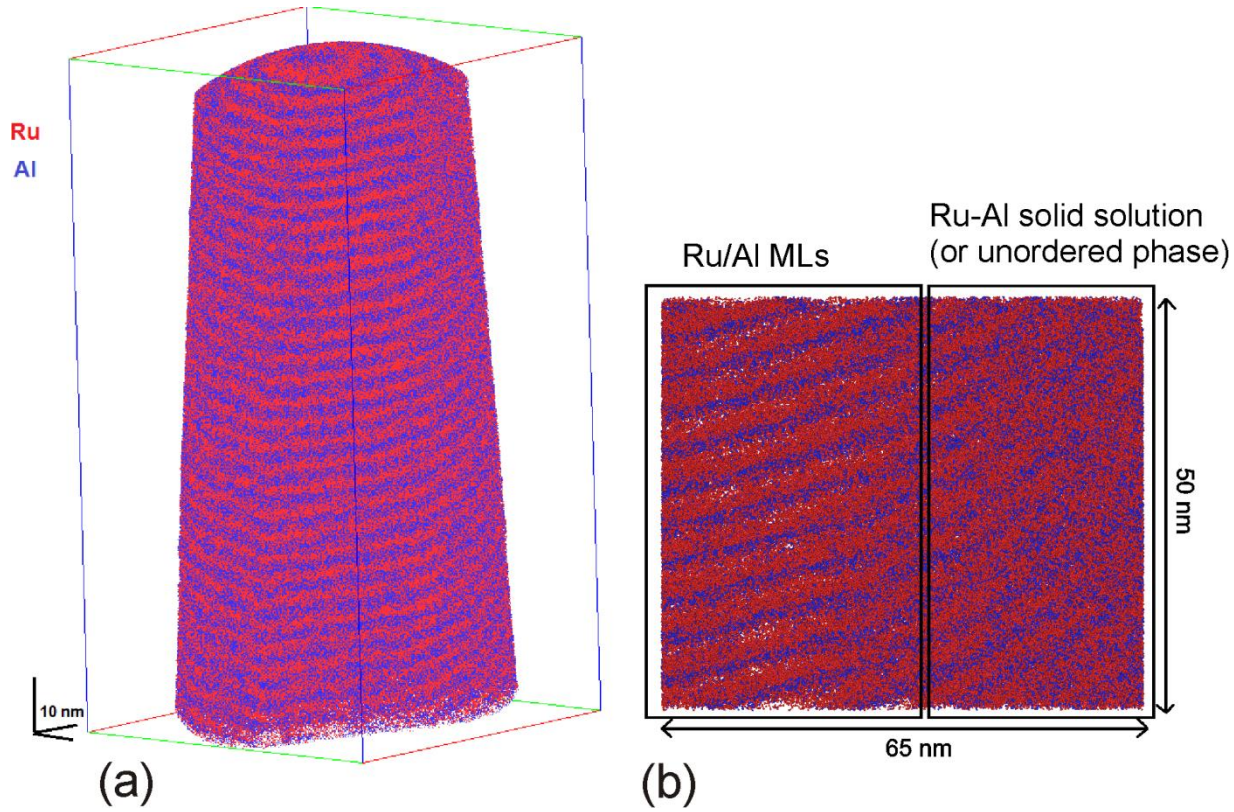

Figure 4.4: APT 3D reconstruction of an as-sputtered sample. The complete reconstruction is shown on the left and a section from the reconstruction (10 nm thick) shows the multilayer and intermixed zones on the right part.

4.2.3. Solid state formation of single-phase RuAl

The RuAl phase formation during the annealing of the as-sputtered Ru/Al samples was studied by in-situ HT-XRD measurements. The measurements were made under vacuum from room temperature RT at 1 °C/min up to 600 °C, every 60 °C with 15 min per diffractogram.

XRD diffractograms (Bragg-Bentano configuration) of the intermetallic phase formation during annealing of the Ru/Al MLs are shown in Figure 4.5. At temperatures below 220 °C, only limited changes in the XRD patterns were detected. The peak intensity is low for the as-sputtered films and the annealed samples up to 280 °C. This might be related to the presence of disordered interfaces, as consequence of the large fraction of interfacial regions in the MLs with very short period [27]. This effect was also observed previously in TEM (Figure 4.2b) and in XRD (Figure 4.3) from the broadening of diffraction rings and diffraction peaks, respectively. As the temperature approached 280 °C, Al and Ru began to react and the characteristic {100} and {200} peaks of the B2-RuAl phase became apparent at around 29.7° and 61.7° (2θ), respectively. At 600 °C, the diffraction pattern shows the presence of very strong peaks corresponding to the single-phase RuAl, whereas those of

the elements have completely disappeared. The growth and evolution of the {100} peak as a function of the temperature during the annealing is also displayed in Figure 4.5. Peaks {100} and {200} developing in intensity during annealing could be the result of the films growing epitaxially to the substrate or the formation of highly textured film. Since the films are deposited onto polycrystalline SS, epitaxial growth is not possible. Furthermore, texture measurements (see Annexe) confirmed the films growing with a strong fibre texture in the [100] direction.

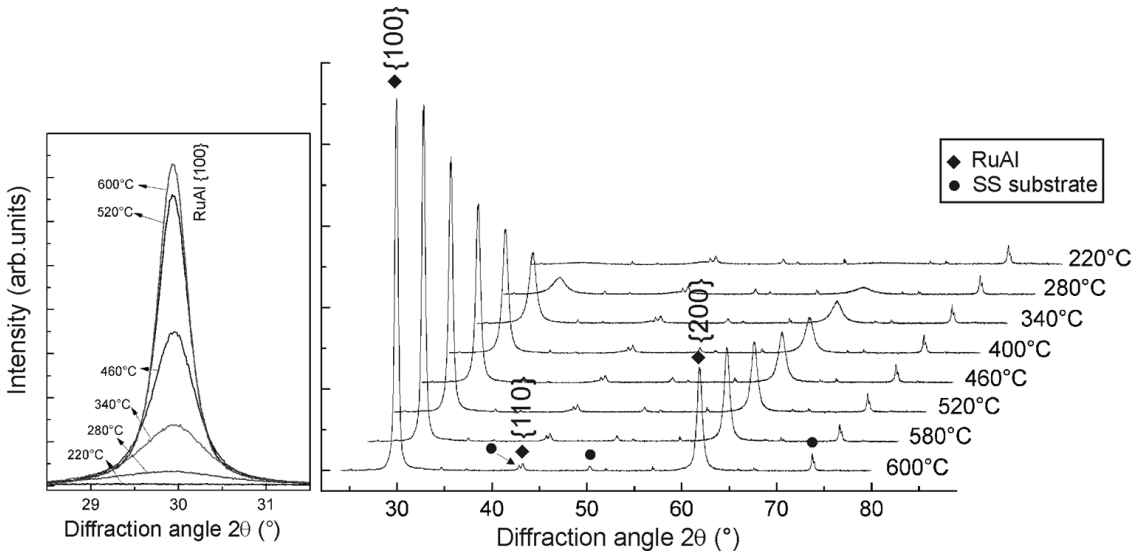

Figure 4.5: RuAl formation as a function of temperature, measured in-situ by HT-XRD, using the Bragg-Bentano configuration. The diffractograms were corrected by subtracting the background intensity. The smaller peaks not indexed correspond to the SS substrate. The left side of the figure shows the evolution of the formation of the RuAl phase for the peak {100}. *JPCDS-RuAl: 29-1404*.

In order to study the kinetics of the RuAl formation, the as-sputtered samples were also analysed isothermally at 280 °C (Figure 4.6), which is the temperature for the RuAl formation observed in Figure 4.5. An intermediate temperature between 280 and 600 °C (400 °C) was also selected for the analysis. The same behaviour was observed in both cases (280 and 400 °C), therefore only the diffractograms for the lower temperature are shown in Figure 4.6. The B2 RuAl phase was the only phase formed. The integral intensity of the RuAl {100} peak showed parabolic time dependence during the isothermal annealing at 280 °C. This indicates that the growth of the RuAl phase was a consequence of a diffusion-controlled process. Further, the grain size was calculated by the Warren-Averbach method [90] as a function of time, during isothermal annealing at 280 °C and 400 °C (Figure 4.7b). Grain size depends on the annealing temperature, being 7.7 nm, 11.7 nm and 27.4 nm after treating at 280 °C, 400 °C and 600 °C, respectively. The values for the samples annealed at 600 °C will be discussed further in Chapter 5 and for this reason they are not included in the graphic.

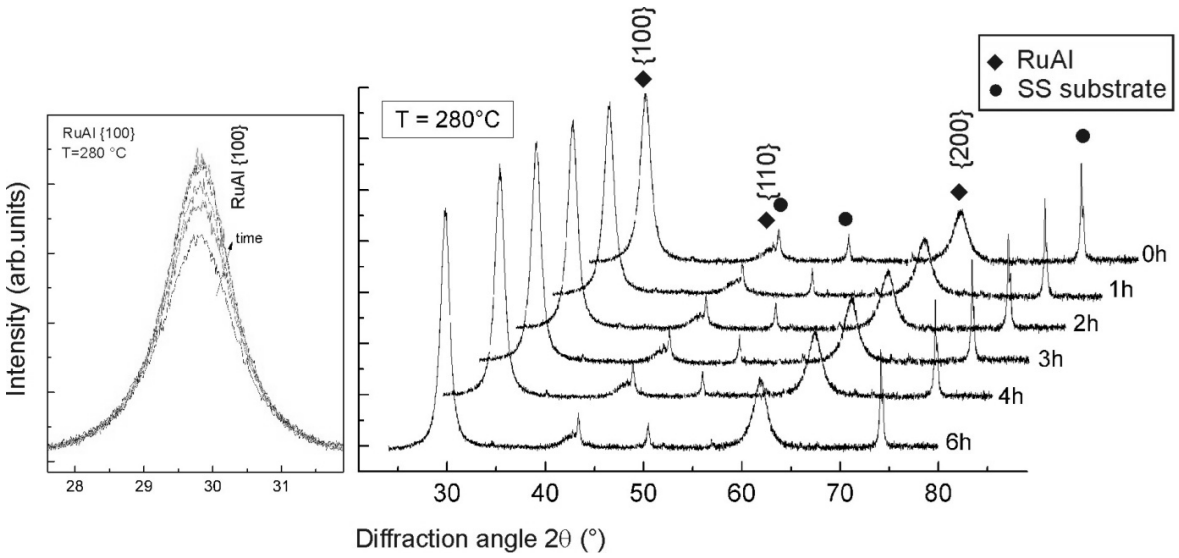

Figure 4.6: Isothermal (280 °C) HT-XRD measurement of RuAl formation as a function of time. The left side of the figure shows the evolution of the RuAl {100} peak as a function of the time, for an annealing temperature of 280 °C.

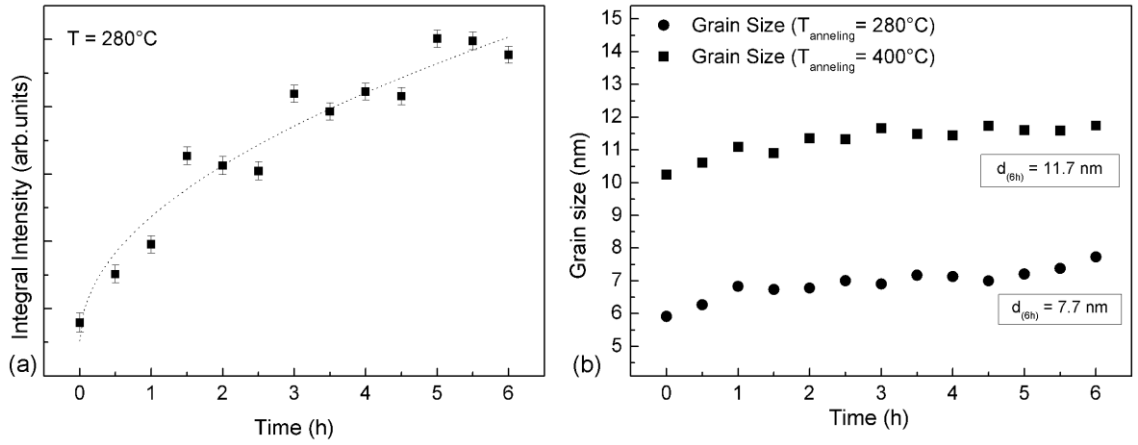

Figure 4.7: (a) kinetic analysis of the integral intensity as a function of time of the RuAl {100} XRD reflexion. The parabolic behaviour is indicative of a diffusive process during the RuAl formation. (b) The evolution of the grain size as a function of time, by HT-XRD measurements at 280 °C and 400 °C. The points at time zero, coincide with the first measurement at the corresponding temperature.

The formation of single-phase RuAl from Ru/Al MLs was reported [3] to be highly dependent on the ML period. It was observed the formation of RuAl at temperatures close to 550 °C in MLs with $\Lambda <$ 4.5 nm. At about 600 °C, the remainders of the MLs were still detected. Moreover, the growth of an intermetallic following intermediate crystalline phases was not observed during annealing of MLs with $\Lambda <$ 22.4 nm. Furthermore, Woll [4] observed that the first phase growing in MLs with Λ = 178 nm was $RuAl_6$, whereas the single-phase RuAl appears after subsequent Ru_4Al_{13} and $RuAl_2$ growth [4]. This behaviour has been also observed in other systems, such as NiAl, FeAl and TiAl films [27,29,91]. The nanometric character of the Ru-Al ML studied here (with periods from 2nm to 3 nm) allows the stable phase RuAl to be directly formed at low temperatures (280 °C), without

producing intermediate crystalline phases as would be formed for larger periods [3]. This might occur due to the Al being almost completely consumed at the intermixed zones and interfaces. Consequently, the Al content drops too low for Al-rich phases to nucleate (i.e. $RuAl_2$, $RuAl_6$), as proposed by Noro et al. during the study of NiAl ML [27].

4.2.4. Microstructural characterisation of the annealed samples

The ML morphology of the as-sputtered samples (Figure 4.2) was completely eliminated after annealing, even at temperatures as low as 280 °C. The micrographs in Figure 4.8 show the equiaxed microstructure of the samples annealed at 280 °C (a), 400 °C (b) and 600 °C (c). A complete transformation into RuAl occurred and no other phase or compound was identified, as shown in the diffractograms of Figure 4.9. After annealing at 600 °C for 1 h, the B2 RuAl films presented a preferential crystallographic orientation, with the {100} planes parallel to the sample surface (Figure 4.9, see also Annexe). The SAD pattern in Figure 4.8c shows the diffraction rings for the single-phase RuAl and a texture along the [100] direction, perpendicular to the film surface.

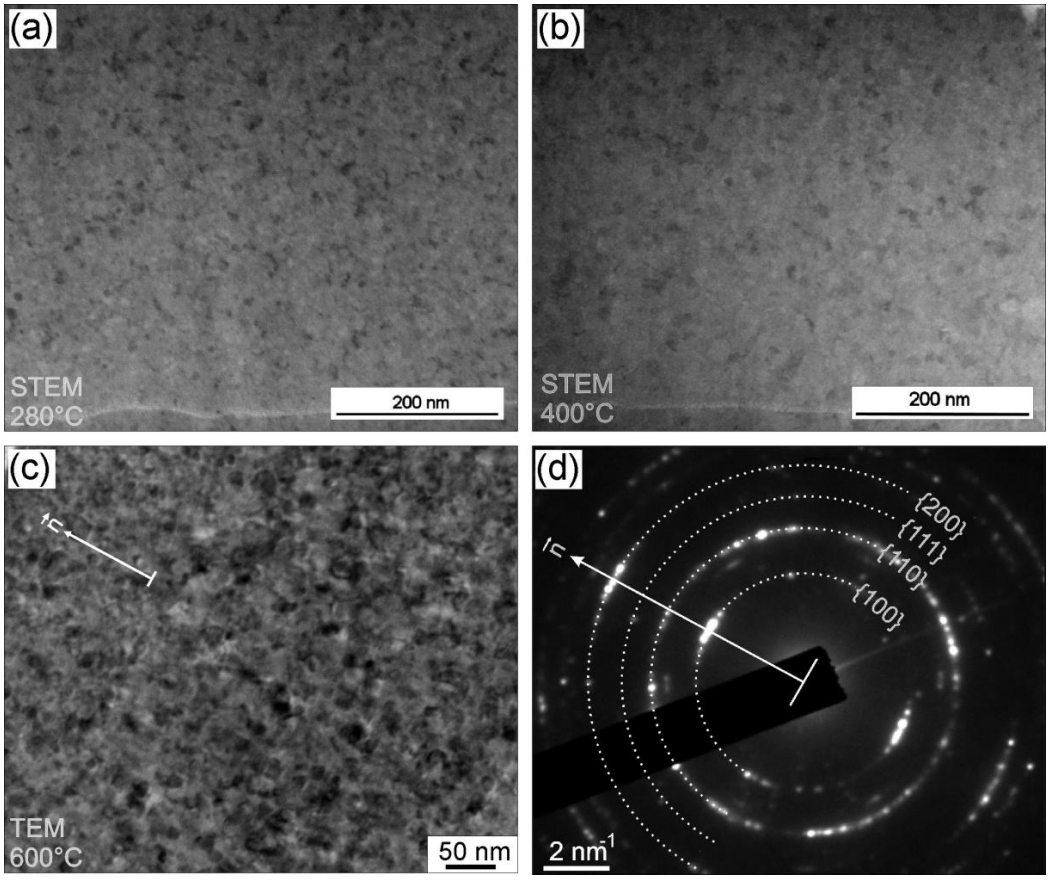

Figure 4.8: Cross-section images of the annealed samples (a) and (b) Bright field STEM micrographs of the single-phase RuAl after annealing in vacuum at 280 °C and 400 °C, respectively; (c) Bright field TEM (JEOL JEM 2011) micrograph of RuAl after annealing at 600 °C and (d) SAD shows the reflections for the RuAl phase with a [100] preferential orientation normal to the film surface. The sample normal direction ($\vec{n}$) is indicated by the arrow in the TEM images.

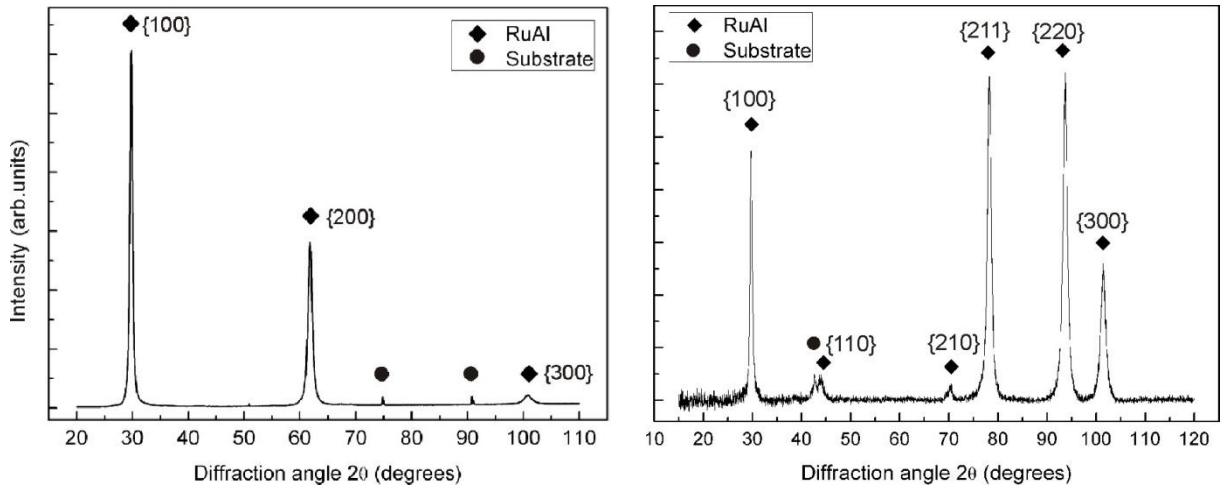

Figure 4.9: XRD phase analysis of annealed samples at 600 °C for one hour: (a) Bragg-Brentano (θ-θ), showing intense {100} and {200} peaks of RuAl phase; and (b) GI configurations.

After deposition and annealing processes, the RuAl thin films resulted in non-stoichiometric compounds possessing excess of about 4 at.% Ru. Despite the deviation in the stoichiometry (see also APT analysis, Figure 4.4), the films lie in the RuAl phase domain. No indication of a Ru-rich second phase was detected either by XRD or TEM analysis. The boundaries of single-phase RuAl were established by Gobran *et al.* [30], ranging from 49.7 up to 53.8 at.% Al. Excess Ru or Al in off-stoichiometric intermetallic compounds is generally relocated in the form of point defects, in order to maintain the B2 structure [31]. The major structural defect in the Al-rich side is due to the Al antistructure defect (ASD), i.e. one Al atom replaces one Ru atom in the lattice [31].

Besides the off-stoichiometry of the films, the presence of ~2.5 at.% Fe and ~0.8 at.% Cr was detected by EDX in TEM foils of the annealed RuAl films (600 °C/1 h), as a consequence of diffusion from the substrate. The isothermal section of the Ru-Al-Fe phase diagram [92] shows a solubility of up to 15 at.% of Fe in RuAl, therefore, the formation of compounds at the impurity concentration found in this work is not expected. The impurities probably remained segregated at grain boundaries or in the form of RuAl(Fe) and/or RuAl(Cr), as observed by Liu *et al.* [93]. Furthermore, Bax *et al*. [94] observed B2 structures with an iron content of approximately 30 at.%, formed by rapid solidification during laser cladding.

The residual stresses in the annealed RuAl films (600 °C/1 h) were determined using a multiple-{hkl} $\sin^2\psi$ stress analysis from GI-XRD measurements [72] and with the help of the PANalytical X'Pert Stress Plus software v.2.1. In-plane residual stress was found to be compressive, with an average value of -1.61 ± 0.04 GPa. The stress resulting from the mismatch in CTE between the RuAl and SS was calculated using Equation 4.1 [95] and it was found to be close to -1.9 GPa.

$$\sigma_{th} = -\frac{\varepsilon_{th} E_f}{(1-\upsilon)} = -\frac{E_f \int_{T_0}^{T} [\alpha_f - \alpha_s] dT}{(1-\upsilon)} \cong -\frac{E_f (\Delta\alpha)(\Delta T)}{(1-\upsilon)} \qquad (4.1)$$

In Equation 4.1, ε_{th} corresponds to the thermal strain, E_f is the elastic modulus of the film, α_f and α_s are the linear CTE ($\alpha_{RuAl} \approx 7x10^{-6}$ K^{-1} and α_{SS} $16x10^{-6}$ K^{-1}) [46] and υ is the Poisson coefficient. The E (276 GPa) and υ (0.286) values used for the stress calculation were those of bulk RuAl [2]. The effects of texture and off-stoichiometry were not considered for this calculation. The total stress in a film is commonly composed of the thermal stresses, resulting from the difference in the CTE between film and substrate material, and by intrinsic stresses, given the accumulation of microstructural defects [62]. The difference between the theoretical and measured values corresponds to further stresses being generated during the production of the films and their phase transformation during annealing at 600 °C.

4.2.5. Adhesion improvement of the RuAl/SS system

In order to achieve an optimal adhesion as the required for the application (see 1.3.4), this was improved by *sputter cleaning*[8] the substrate and by depositing a *Ti adhesion layer*[9] (50 nm), prior to the Ru-Al deposition. The *sputter cleaning* is used to remove oxides and contaminated surface layers by ion bombardment, increasing the surface reactivity as detailed in the literature [96]. Deposition of a metallic interlayer improves the film/substrate adhesion by minimising stresses gradient at the interface and dissolving contaminants [96–98]. Ti and Cr are the most common metals used for this propose [97]. In the particular case of Ti, it shows high oxygen affinity reducing the Cr_2O_3 on the SS surface by forming Ti oxides (TiO or TiO_2) with strong chemical bonds to the substrate [99].

Table 4.2: Critical load (L_c) values determined from 5 measurements by microscopy methods for RuAl thin films, deposited onto stainless steel, with thickness of 650 and 1200 nm.

	L_c [mN] (t = 0.65 µm)	**L_c [mN]** (t = 1.2µm)
Ti adhesion-layer	20 ± 3	52 ± 3
Sputter-cleaned	15 ± 1	42 ± 2

The mechanical response of the RuAl films (650 and 1200 nm) to the substrate was evaluated identifying the critical load (L_c), which is defined as the minimum load at which some level of damage is observed in the coating [100]. The L_c for RuAl films containing a Ti adhesion-layer showed higher values than for the sputter-cleaned samples. The corresponding values are listed in Table 4.2. L_c also varies with the coating thickness, being lower for thinner films. It was demonstrated [81] that L_c depends on several parameters related to the testing conditions and the

8) *Sputter cleaning parameters*: under an Ar plasma for 10 seconds at 4 x 10^{-3} mbar, with a power of 1000 W.
9) *Ti-layer deposition parameters*: 300 W power at 3 x 10^{-3} mbar (2 nm/sec deposition rate)

coating/substrate combination, such coating thickness, substrate hardness and friction between stylus and coating, among others.

A detailed adhesion-failure classification after scratch tests were proposed by Burnett and Rickerby [80]. From this, the damage in the RuAl films was classified as *tensile cracking failure,* which is a ductile type of failure. It is characterised by the coating remaining fully adhered to the substrate, as shown in Figure 4.10. In this failure mode, the load on the diamond stylus is transferred to the front half of the indenter once the sliding starts. Material piles ahead of the stylus, causing the bending of the coating (which puts its surface under tension). Loss of RuAl/SS adhesion was not observed in any of the cases studied here. The cracks in the film are formed as a result of the tensile frictional stresses present behind the trailing edge of the stylus. These balance the compressive frictional stresses ahead of the stylus, as detailed in [80].

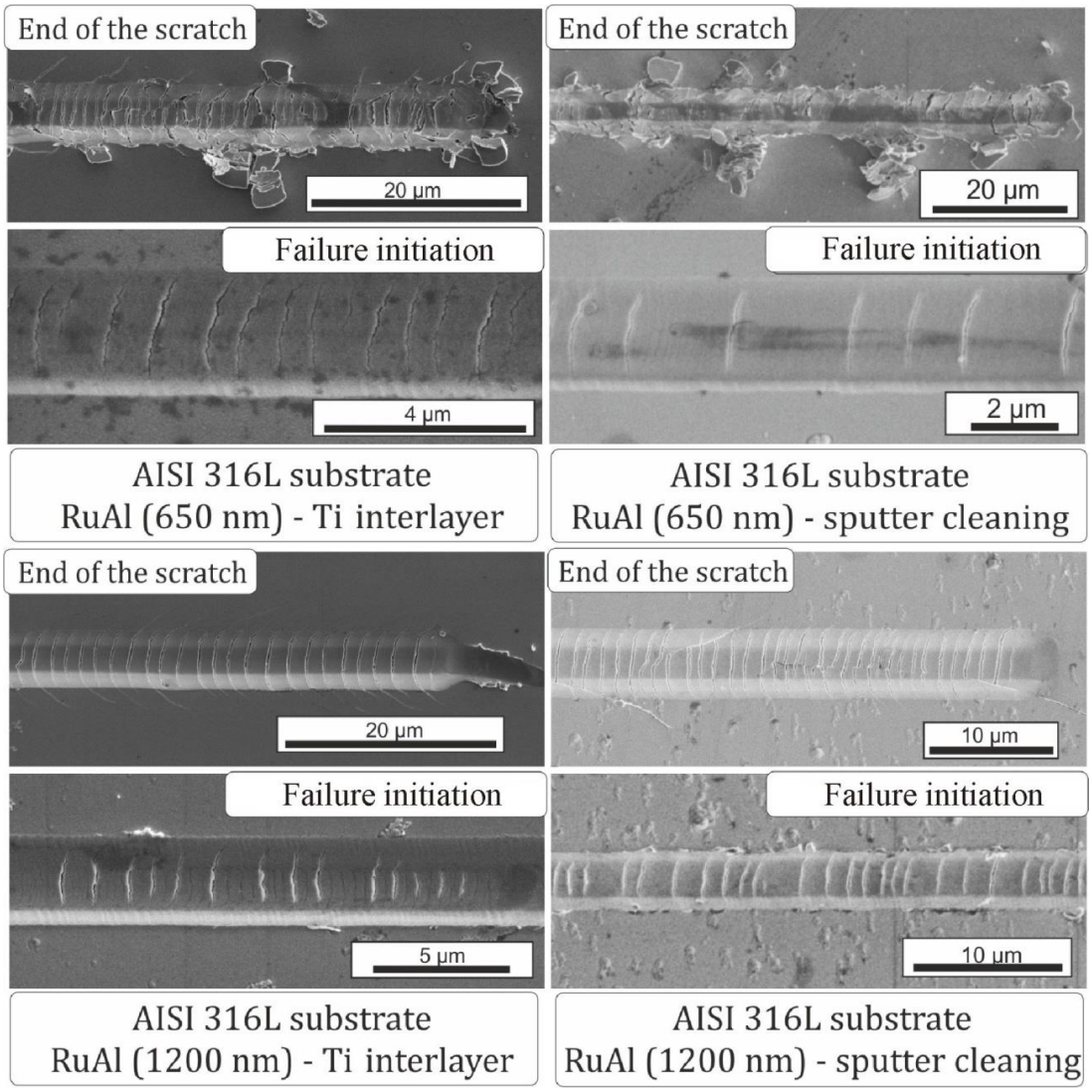

Figure 4.10: SEM images of the scratch tracks on RuAl thin films. These were deposited onto stainless steel, with thickness of 650 nm and 1200 nm using a Ti adhesion layer and sputter cleaning. In all cases, the stylus direction was from the left to the right. No detachment or adhesion loss was also observed at the end of the scratch.

4.3. Summary and outlook

By using sequential Ru-Al deposition and a subsequent annealing it was possible to synthesise a single-phase RuAl intermetallic compound onto technically relevant substrates at low temperature. The as-sputtered films were composed of Ru/Al MLs with individual thickness around 1-2 nm and reaction zones identified as RuAl. The latter was formed, in part, due to the creation of a co-deposition region between the Al and Ru targets, given the high-spatial distribution of the sputtered material. Furthermore, interdiffusion at the Ru/Al and Al/Ru interfaces was evidenced by a broadening of diffraction peaks in XRD and diffraction rings in SAD analyses. By annealing the samples, the multilayer structure quickly disappeared and single-phase RuAl was obtained. The small bilayer period leads to rapid homogenisation of the multilayers, thus avoiding intermediate intermetallic phases to grow and allowing the B2-RuAl to form at temperatures as low as 280 °C. The formation of ~4 at.% Ru off-stoichiometric RuAl films is noteworthy, expanding the existence range of the single-phase in comparison to bulk materials.

Texture with a {100} crystallographic orientation was created during the annealing of the films. The appearance of in-plane compressive stresses of about 1.6 GPa occurred mainly due to the CTE mismatch between the SS substrate and RuAl. No significant difference in stress values was found for the RuAl films using a Ti adhesion layer or sputter cleaning. However, higher L_c was observed during scratch testing of the film with a Ti adhesion layer but not on the sample with a sputter-cleaned surface.

5

Thermal stability and grain growth

This chapter focuses on the study of the grain growth and the thermal stability of nanocrystalline (nc) RuAl thin films, deposited onto austenitic stainless steel at elevated temperatures in non-oxidising environment (vacuum, in this case). As an introduction, previous studies about grain growth and thermal stability of RuAl are summarised. A theoretical background of grain growth in NC materials and thin films is also presented.

The second part of the chapter shows the results obtained from the study of the grain growth behaviour of the RuAl/SS system at three different temperatures. This includes microstructural and kinetic aspects, followed by thorough discussion and conclusions.

The results here exposed have been published in the peer reviewed journal *Thin Solid Films* (*Study of grain growth and thermal stability of nanocrystalline RuAl thin films deposited by magnetron sputtering* – M.A. Guitar, K. Woll, E. Ramos-Moore, F. Mücklich – Thin Solid Films 527 (2013).

5.1. Introduction

Grain growth results in changes in the microstructure and, thereby, strongly influences mechanical and other material properties. In NC materials (grain size up to 100 nm), a significant volume fraction of the microstructure corresponds to grain boundaries. This results, in several cases, in material properties which are significantly different from those of the coarse-grained (CG) polycrystall. Through grain growth, a nanocrystalline state can evolve, along with its properties, into the conventional CG state.

Many structural and functional characteristics of NC materials depend strongly on the thermal, chemical or phase stability. In particular, the thermal stability of NC materials is especially important in high-temperature applications [38,101]. Such fine structures are not thermodynamically stable over time at elevated temperatures, because of the large driving force for grain growth derived from the high energy stored at grain boundaries. Thermal stability of nano-grained RuAl produced by mechanical alloying was previously studied by Liu et.al [93,102]. However, no studies on the thermal stability on RuAl thin films have been carried out so far. For application of thin-film intermetallic RuAl, the phase, grain size and also stability at elevated temperatures are of high interest. It is also of great importance to be able to control the microstructure, in particular the grain size and texture which develop during deposition and post-deposition annealing processes.

Grain growth can develop in normal or in abnormal form. Normal grain growth is characterised by a unimodal grain size distribution with the annealing time, while abnormal growth is bimodal. In the last case, some large grains in a matrix of fine grains can be observed. Both behaviours are evaluated in the present chapter.

5.2. Theory of grain growth

The dominant driving force for grain growth is the reduction of grain boundary (GB) area and therefore the total GB energy of the system. This process results in a reduction of the total number of grains and an increase in its average size during annealing, due to GB migration [103].

The driving force for grain growth is expected to be high in NC materials, given the large and highly disordered interfacial component [104]. Grain growth in CG polycrystals commonly occurs through grain boundary migration and coalescence. The GB curvature acts as a driving force for the grain growth. The atoms on both sides of a curved GB are under different pressures. This difference (ΔP) is given by $2\gamma_{gb}/r$ and acts towards the centre (Figure 5.1) [105], where r is the curvature radius of the GB and γ_{gb} the GB energy per unit area.

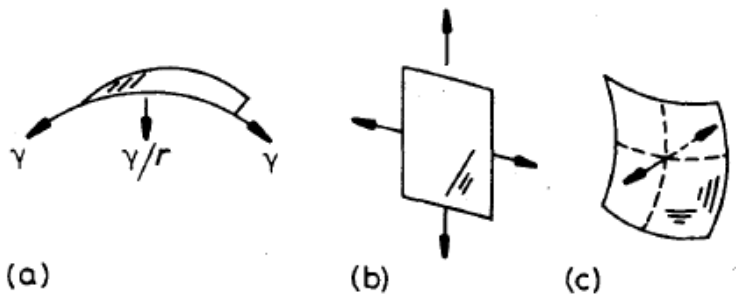

Figure 5.1: Grain boundary curvatures: (a) cylindrical boundary with curvature radius r and acting force γ/r; (b) planar boundary with no net force; (c) twofold-curved boundary with no net force [105].

Since curvature is the main driving force for GB migration, grains possessing six or more sides and concave GB tend to grow, while grains with less than six sides and convex GB tend to shrink and disappear, due to the effect of curvature (Figure 5.2). The atoms in shrinking grains detach from the lattice on the high-pressure side of the boundary, relocating into the lattice of the growing grain.

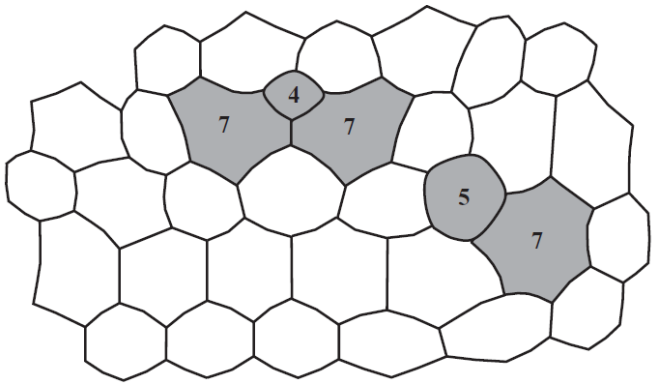

Figure 5.2: Array of grains with convex and concave boundaries. Grains with six or more boundaries (grey coloured) will tend to grow [103].

5.2.1. Grain growth kinetics

The grain growth theory described elsewhere [103,106], shows that the growth rate of the averaged grain size $\bar{d}$ must be proportional to the average velocity $\bar{v}$ of GB movement, as indicated by Equation 5.1, where α is a geometric constant, M[10] is the average GB mobility and γ_{gb} is the GB energy per unit area.

$$\bar{v} = \frac{d\bar{d}}{dt} = M\alpha\frac{2\gamma_{gb}}{\bar{d}} \qquad (5.1)$$

Furthermore, the rate of grain growth is inversely proportional to $\bar{d}$ and increases rapidly with the temperature, due to higher boundary mobility. Integration of Equation 5.1 results in Equation 5.2 where K incorporates the mobility, energy and the geometry of GBs, having the form $k = k_0 exp\left(\frac{-Q}{RT}\right)$.

$$\bar{d}^2 = d_0^2 + Kt \qquad (5.2)$$

Equation 5.2, showing a grain growth exponent n = 2, is a particular case describing the kinetics of normal grain growth in very pure materials. The general case is given by the power law shown in Equation 5.3, where the experimentally determined values of n are usually higher than 2, adopting this value only for highly pure metals or at very high temperatures [38,107]. In a single-phase metal, the rate growth of the mean grain diameter $\bar{d}$ depends on the GB mobility and the driving force for boundary migration.

10) M has the form $M = M_0 exp\left(\frac{-Q}{RT}\right)$ and it takes into account the diffusion coefficient across GBs, GB thickness and atom volume [109].

$$d_{(t)}^n - d_0^n = k\ t \qquad (5.3)$$

The *n* value is known as the driving force exponent [108] and it is, as well as the growth rate, determined from the evolution of grain size in time. Moreover, the grain growth activation energy is calculated from the temperature dependence of *k*. By assuming a very small value, the initial grain size d_0 can be neglected and the grain growth law can be manipulated to exhibit the form of Equation 5.4, where the time exponent for grain growth $m = 1/n$.

$$d = k\ t^m \qquad (5.4)$$

During normal grain growth, some grains expand and others shrink according to Equation 5.1. The increase in the average grain size leads to a corresponding decrease in the total grain boundary area. As a consequence, the energy of the system decreases due to the reduction of the excess free energy associated with GBs.

In NC materials it is commonly accepted that pinning forces act causing grain growth stagnation. This case is described by Equation 5.5 [93], where d_m is the maximum grain size.

$$\frac{d_0 - d}{d_m} + ln\left(\frac{d_m - d_0}{d_m - d}\right) = k\ t \qquad (5.5)$$

The discrepancy often found between theory and experiment results could be in part attributed to impurity drag of grain boundaries. In NC materials and thin films, triple junctions and thermal groove drag also influence the boundary mobility and thus the grain growth. Some of these mechanisms are detailed next.

5.2.2. Inhibition of grain growth

The factors affecting GB mobility include the drag of solute, pores, second phases (Zener), triple junctions and thermal grooves, as described in [103,106]. In some cases, grain growth inhibition can lead to the development of a microstructure with abnormal grains, as a consequence of only those grain subpopulations growing, that have lower GB energy and specific crystallographic orientation.

a) Grain growth stagnation due to the presence of second phase particles: Zener effect.

Moving boundaries tend to attach to second-phase particles that they come across. The boundary motion is restricted by the pulling force exerted by these particles. This pinning force depends on the second-phase particle size and its angle θ with the boundary, which changes as it advances [105].

The drag force F_d of a single particle against boundary movement (Figure 5.3) is given by Equation 5.6, and it leads to a reduction in the total GB energy.

$$F_d = \gamma_{gb}\sin(\theta)2\pi r cos(\theta) = \pi r \gamma_{gb}\sin(2\theta) \qquad (5.6)$$

By assuming constant particle radius *(r) and* volume fraction *(f_v)* and considering that the maximum drag force is reached at $\theta = 45°$ (from Equation 5.6), then the maximum pinning force restricting GB movement is represented by Equation 5.7:

$$F_d = \frac{3}{2}\frac{f_v \gamma_{gb}}{r} \qquad (5.7)$$

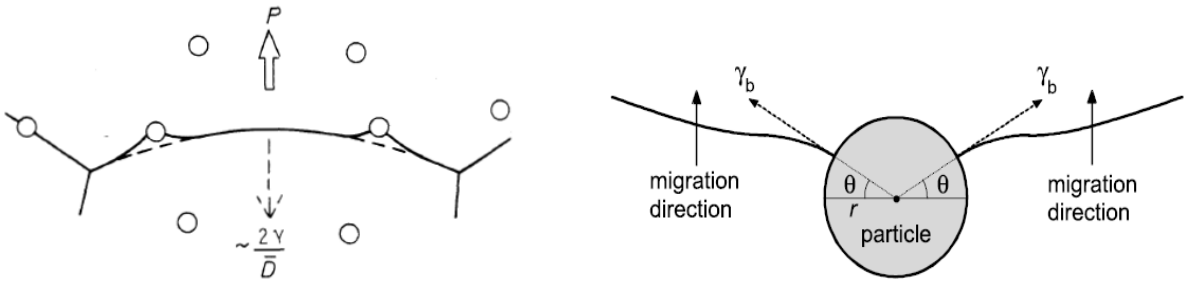

Figure 5.3: grain boundary dragging by second-phase particles [109].

b) Grain growth stagnation due to the presence of impurities (solute drag)

Segregation at GBs occurs when the local sites for solute atoms have lower energy than at the bulk. The movement of GBs in the presence of solute particles depends on the impurity concentration at the grain boundary, $C_b = C_0 \exp(-E/kT)$, where C_o is the solute concentration in the bulk material; E the activation energy for solute migration; k the Boltzmann constant and T the absolute temperature. Solute particles tend to migrate together with the boundary, acting as drag forces against their displacement. Thus, the boundary migration is as fast as the slowest moving impurity [106,109]. The force P_v exerted by the impurities is given in Equation 5.8 [106], where n_0 is the number of sites per unit area of the GB; n ($=n_0 C_b$) the number of sites of the GB occupied by impurities; and f the force exerted by one particle alone.

$$P_v = n f = n_0 C_b f = n_0 C_0 \exp\left(-\frac{E}{kT}\right) f \qquad (5.8)$$

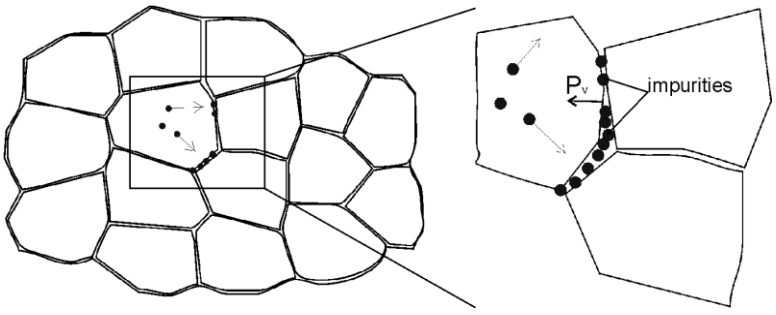

Figure 5.4: Drag force exerted by impurities segregated at GBs.

c) Triple junction drag

Grain growth in NC materials is highly influenced by the drag effect of triple junctions. When the limited mobility of triple junctions is lower than that of GBs, a hampering force for grain growth appears. This behaviour causes deviations from the triple-junction equilibrium angles (120°).

The triple-junction movement (Figure 5.5) is accompanied by transformations of grain-boundary dislocations and re-arrangement of point defect distribution in the vicinity of the triple junction. These processes are slow and/or need to overcome energetic barriers, thus the triple-junction movement can be much slower than that of GBs.

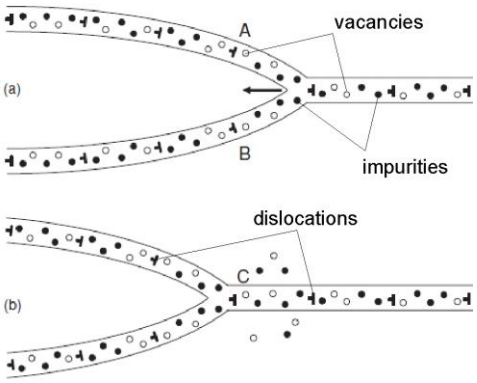

Figure 5.5: Triple junction movement: (a) initial and (b) final positions. This movement is accompanied by re-arrangement of vacancies and impurities and the convergence of grain-boundary dislocations [103].

d) Thermal groove drag

Thermal grooves formed by the intersection of a GB with the surface of the film can cause grain growth stagnation, if it is assumed that the only driving force for growth is GB energy reduction [107]. This effect is normally observed in thin films.

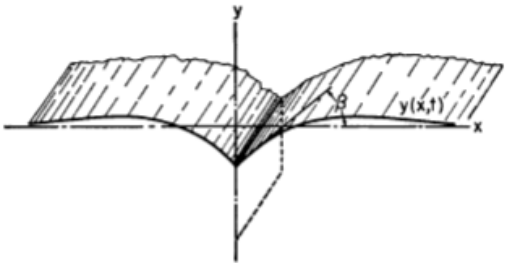

Figure 5.6: surface grooves formed as a consequence of grain boundary intersection with the surface of the material [106].

5.2.3. Grain growth in thin films

The theory of grain growth and the study of microstructure and texture evolution in polycrystalline thin films has been widely developed by Thompson [107,110–112]. He related the surface and strain energies to the abnormal grain growth in thin films and to the texture evolution.

Grain growth can occur either during film deposition or post-deposition processing, resulting in a dramatic increase in the average grain size and changes in crystal orientation. Depending on the material and the deposition conditions, the as-deposited grain size can be smaller than the film thickness ($d < h$). By depositing at 20 to 30% of their melting point (T_m), metals generally develop near-columnar fibre-like microstructure, with a considerably smaller average grain size when measured in planes parallel to the film surface (d_i) rather than perpendicular ones (d_p) (Figure 5.7a) [107]. Equiaxed microstructures can also be obtained in as-deposited metallic films, with similar d_i and d_p (Figure 5.7b). In this case and if the grain size is smaller than the film thickness, three-dimensional (3D) normal grain growth can occur, as previously described by Equation 5.3. Figure 5.7 shows schematic cross-sections of as-deposited films and the result of normal grain growth. 3D grain growth generally stops once the average grain size is similar to the film thickness. From there onwards, completely columnar grain structure develops [107].

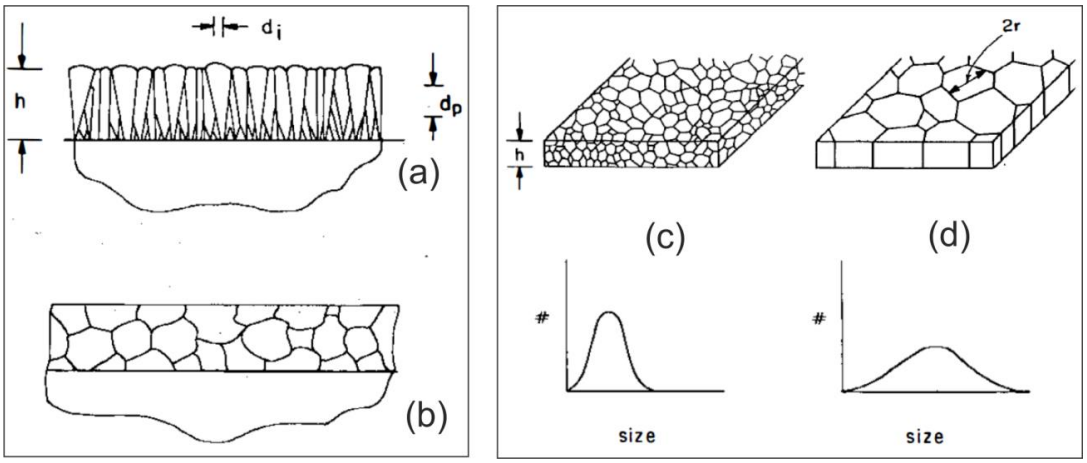

Figure 5.7: Schematic cross-sectional view of as-deposited films with (a) near-columnar, fibre-like and (b) equiaxed microstructure. Schematic microstructure and grain size distribution from (c) a film with equiaxed grains smaller than the film thickness and (d) a film with stagnant columnar grains after three-dimensional normal grain growth [107].

5.2.4. Abnormal grain growth

Abnormal grain growth is characterised by few grains achieving very large diameters within a matrix of fine slowly growing grains. The large grains expand, consuming the surrounding fine grains until these become entirely replaced by a coarse-grain array (Figure 5.8) [103]. In normal grain growth, the range of sizes and shapes is relatively narrow. This is not the case for abnormal growth, where these features show time dependence (Figure 5.9).

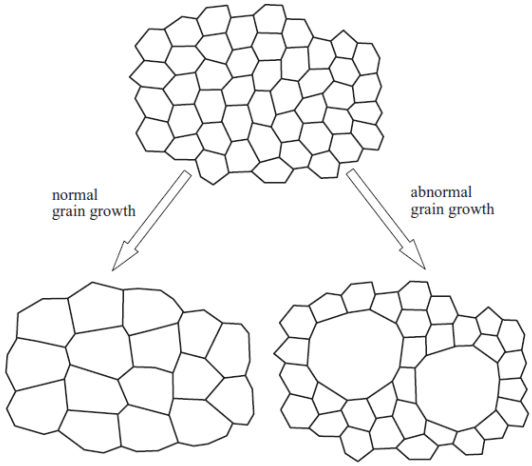

Figure 5.8: Normal and abnormal grain growth regime [103].

In case of thin films, abnormal grains tend to have specific crystallographic planes parallel to the substrate surface, due to the energy anisotropy at the free surfaces of grains [8]. Abnormal growth in thin films is driven by the difference in the surface and strain energies between neighbouring grains. Many factors lead to abnormal growth in thin films, such as the presence of second-phase precipitates, high concentration of impurities and high anisotropy in interfacial energy.

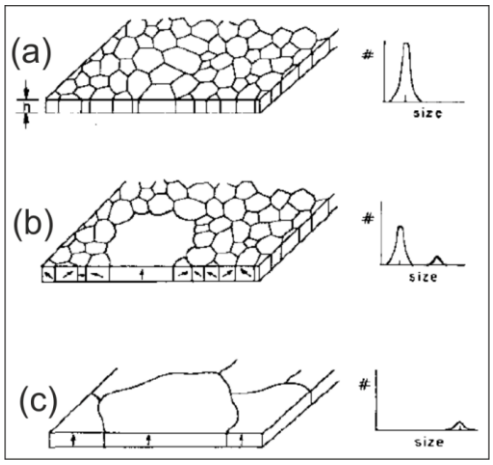

Figure 5.9: Microstructure and grain size distributions for films undergoing secondary grain growth [8]. (a) normal grain size showing a monomodal distribution; (b) abnormal growth presenting a bimodal distribution and (c) monomodal distribution of large grown grains.

5.3. Experimental

The RuAl/SS samples were fabricated as detailed in section 4.2. The thermal treatments were carried out using the parameters listed in Table 5.1. Image analysis (I-A) of STEM micrographs and XRD peak broadening were used to analyse the grain size evolution. Electron backscatter diffraction (EBSD) was employed for cross-checking purposes, measuring at 15 kV and with a step size of 20 nm. The total surface analysed by this technique was 20 x 20 μm^2 and the average grain

size obtained was compared to those from I-A and XRD. The kinetics of grain growth was also studied in an isothermal regime.

Table 5.1: Thermal treatment parameters used to study grain growth and thermal stability of RuAl thin films on SS substrates. One different sample was used for each condition. The temperatures were selected considering the process parameters for glass moulding (see section 1.3.4).

Thermal treatment conditions			
Temperature	**Time**	**Heating and cooling rate**	**Atmosphere**
650 °C - 700 °C - 750 °C	From 1 to 6 h (1 h steps)	20 °C/min	Vacuum (~10^{-5} mbar)

5.4. Results and Discussion

Phase stability was observed in the single-phase RuAl films after annealing for 6 h at 650 °C, 700 °C and 750 °C (Figure 5.10). The diffractograms (Bragg-Brentano configuration) of Figure 5.10 exhibit the {100} and {200} peaks for all the temperatures during the whole duration of the annealing process, indicating no phase transformation.

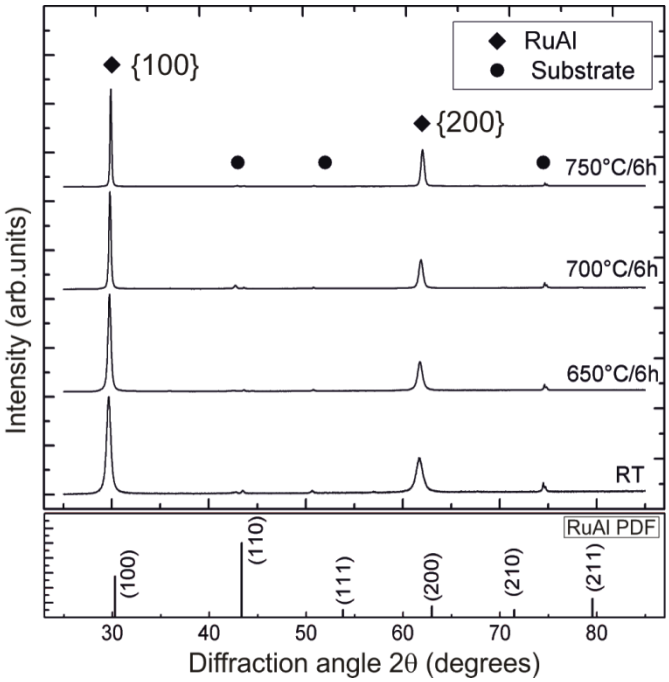

Figure 5.10: XRD pattern[11] (Bragg-Brentano configuration) of RuAl powder (PDF); non-treated (RT) and isothermally annealed RuAl/SS samples. The curves were normalised using the most intense peak {100}.

5.4.1. Grain growth evolution

At the beginning, RuAl films present equiaxed grains with an average size of 24 ± 2 nm, as shown by the STEM micrograph of Figure 5.11a.

11) Published: **M.A. Guitar**, K. Woll, E. Ramos-Moore, F. Mücklich, Thin Solid Films 527 (2013).

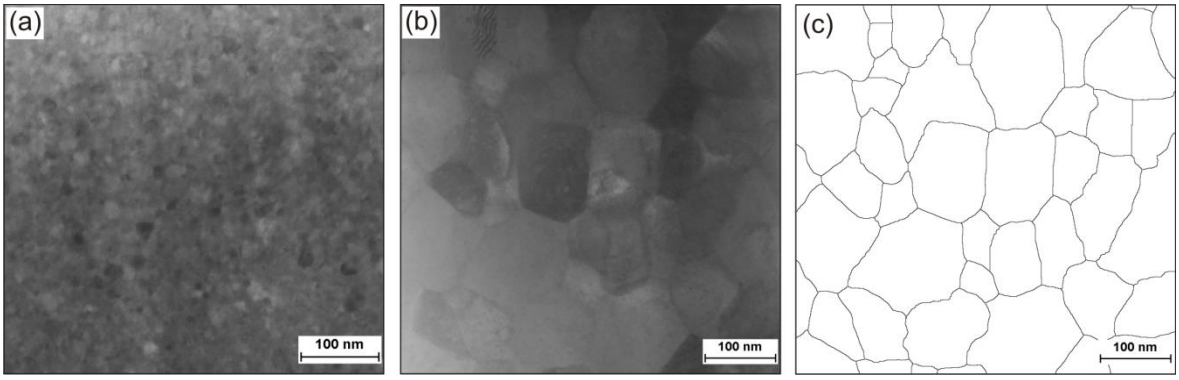

Figure 5.11: (a) STEM image[12] of a RuAl sample after 1 h at 600 °C to induce single-phase formation; (b) STEM image of an annealed sample at 750 °C for 3 h and (c) its grain boundary reconstruction using the software A4i.

The grain size of RuAl films annealed at 650 °C, 700 °C and 750 °C and for different times was calculated by grain boundary reconstruction of the STEM images (Figure 5.11b and c), providing relevant and reliable information such as average grain area and grain size distribution. The results are plotted in Figure 5.12 where an increase in the mean grain size with increasing temperature is observed.

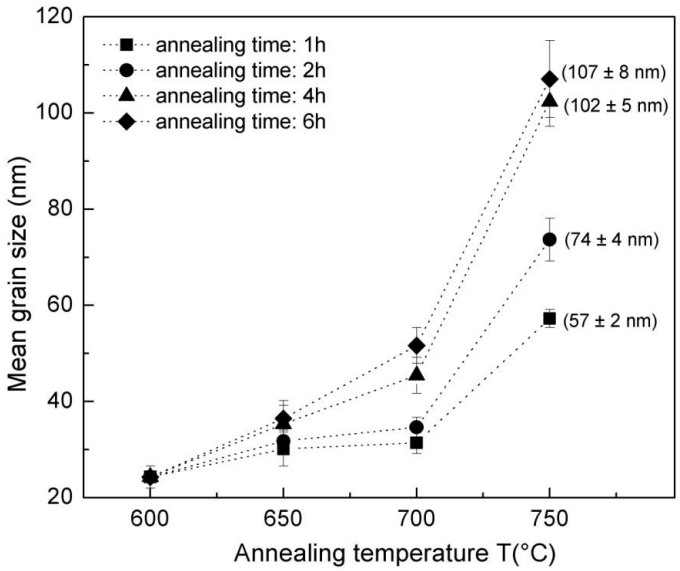

Figure 5.12: Grain size calculated with the software A4i, as a function of annealing temperature[13].

The grain size distribution in NC materials, *f(d),* is usually fitted using the log-normal function described by Equation 5.9 [107].The corresponding histograms for RuAl grain size distribution are shown in Figure 5.13.

$$f(d) = \frac{1}{d.\sigma\sqrt{2\pi}} \exp\left[\frac{-(\ln d - \mu)^2}{2.\sigma^2}\right] \qquad (5.9)$$

12) and 13) Published: **M.A. Guitar**, K. Woll, E. Ramos-Moore, F. Mücklich, Thin Solid Films 527 (2013).

The parameter d is the grain size, while μ and σ are fitting parameters corresponding to the mean value and standard deviation of $ln(d)$, respectively. All fitted curves showed a correlation (r^2) higher than 92%.

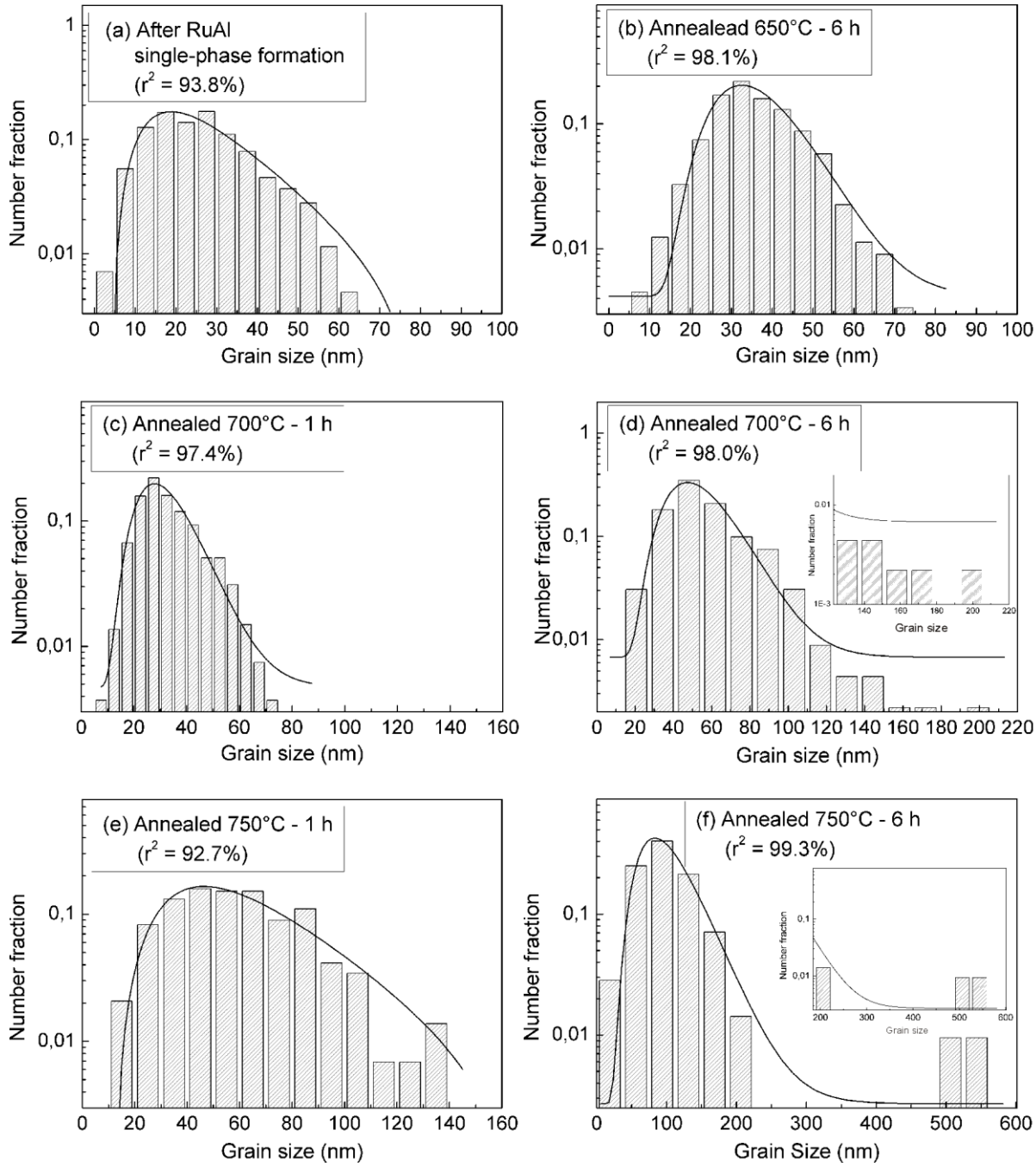

Figure 5.13: Grain size distribution[14] after: (a) RuAl single-phase formation; (b) annealing at 650 °C for 6 h; at 700 °C for 1 h (c) and 6 h (d); at 750 °C for 1 h (e) and 6 h (f).

A log-normal grain size distribution is typical for many NC materials in initial and annealed states [113,114]. Normal grain growth was observed for all the samples treated at 650 °C (Figure 5.13b). Those annealed up to 4 h at 700 °C and up to 3 h at 750 °C have shown the same behaviour (Figure

14) Published: **M.A. Guitar**, K. Woll, E. Ramos-Moore, F. Mücklich, Thin Solid Films 527 (2013).

5.13c and e, respectively). However, abnormal growth was present in the films for annealing times longer than 3 hours at 700 °C and 4 hours at 750 °C (Figure 5.13d and f, respectively).

Abnormal grains were identified through STEM images, as observed in Figure 5.14 Both normal and abnormal grains occasionally reached sizes exceeding half the thickness of the film (Figure 5.14c and d).

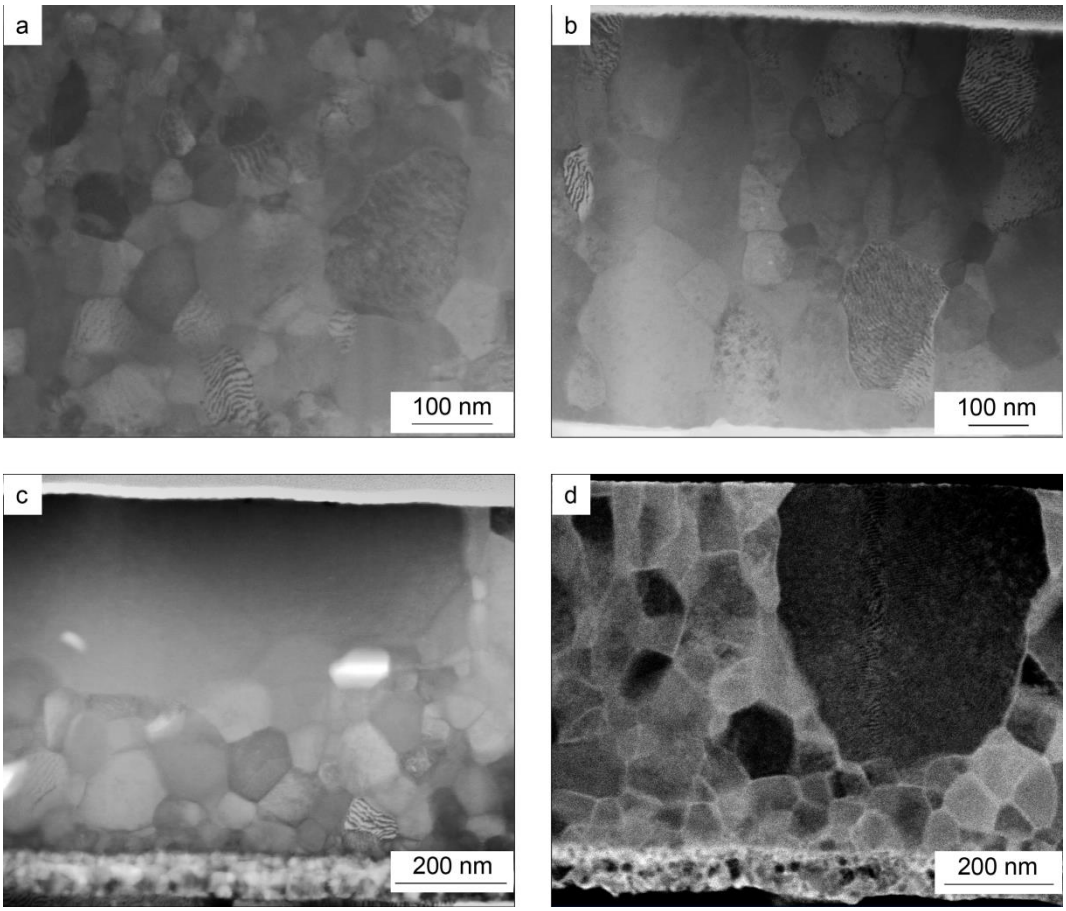

Figure 5.14: STEM micrographs[15] showing films with abnormal grain growth: (a) BF image of a sample annealed 6 h at 700 °C; (b) and (c) display BF images of samples annealed at 750 °C for 3 h and 4 h, respectively; (d) DF image of a sample annealed for 6 h at 750 °C.

5.4.2. Grain growth kinetics

The isothermal grain growth data obtained by I-A and its corresponding fitting, using Equation 5.3 ($d_{(t)}^n - d_0^n = k\,t$), are shown in Figure 5.15. The samples annealed at 650 °C show only a weak increase in grain size. However, at 700 °C and 750 °C, it becomes more pronounced, with grain sizes up to 55 and 107 nm, respectively. The grain growth exponent n was found to be temperature dependent, being 6.1 ± 0.1, 4.1 ± 0.1 and 3.2 ± 0.1 at 650, 700 and 750 °C, respectively. For normal growth in CG materials, the parameter n is expected to be 2 (see 5.2.1), but, for NC materials, variations have been observed [112,115,116]. Previous works in other systems showed n to range

15) Published: **M.A. Guitar**, K. Woll, E. Ramos-Moore, F. Mücklich, Thin Solid Films 527 (2013).

between 2 and 10 and a temperature dependency was also observed in some systems [107,115,116].

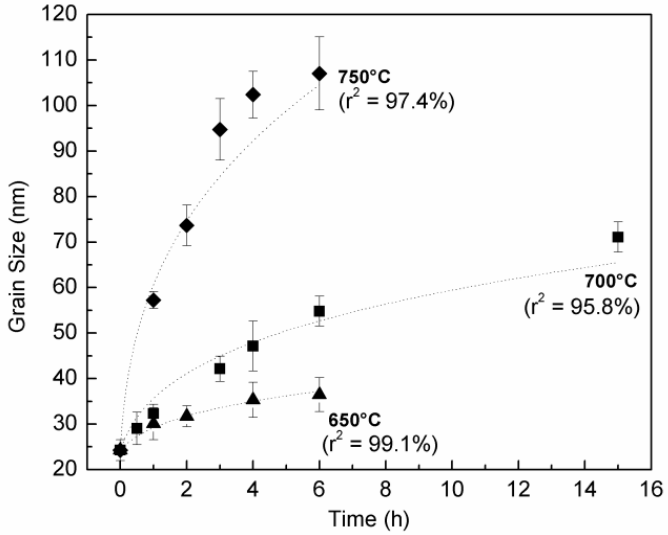

Figure 5.15: Grain size of RuAl thin films as a function of annealing time at different temperatures[16].

Figure 5.16 shows the evolution of the time exponent for the grain growth $m = 1/n$ (Equation 5.4) as a function of the normalised temperature (T/Tm). m increases towards 0.5 (n = 2) with T/Tm, tending to the ideal case of Equation 5.2 ($d^2_{(t)} - d^2_0 = k\,t$) [107]. Many factors influence grain boundary mobility, leading to a deviation of n. These include impurities (solute drag), precipitates or pore drag (temperature sensitive), surface grooving, grain boundary energy anisotropy and initial texture [107,115–117]. Due to the fact that grain growth in NC materials develops differently than in CG polycrystalline materials [118], it may be difficult to identify its mechanism on the basis of the exponent n alone [113,118–120].

Thin films possessing grain sizes much smaller that the film thickness, experiment grain growth induced by a 3D curvature-driven evolution, as observed in bulk materials [107]. The growth is governed by Equation 5.3 and is characterised by a monomodal grain size distribution. The RuAl films studied in this work exhibit a ratio of average grain size (24 nm) to the film thickness (600 nm) of 0.04, thus their grain growth kinetics should adopt this growth mechanism, at least for most temperatures and times. In fact, the grain size distribution showed a fit correlation greater than 92% with the log-normal distribution (Figure 5.13), agreeing with similar experiments performed on NC materials in initial and annealed states [113,114]. For annealing temperatures of 700 °C and times of 6 hours or longer, abnormal growth was observed, depicted by a bimodal grain size distribution. This behaviour was also observed after annealing the samples for 4 h at 750 °C (Figure 5.13).

16) Published: **M.A. Guitar**, K. Woll, E. Ramos-Moore, F. Mücklich, Thin Solid Films 527 (2013).

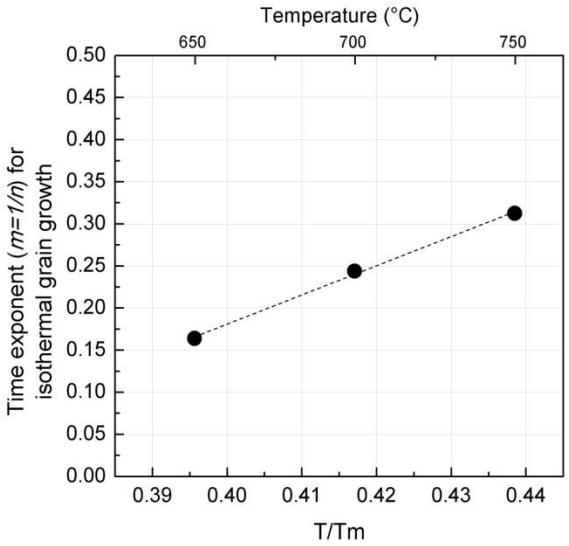

Figure 5.16: Variation of the parameter m = 1/n of NC RuAl thin films for isothermal grain growth according to Equation 5.3 with the normalised annealing temperature.

The I-A of STEM micrographs used in the previous analysis is a direct method which allows only the local study of small regions in the cross-section of the film. Using an indirect method based on XRD, a much larger area of the sample (20 μm x 20 μm in this case) can be analysed, since the information is extracted from the whole X-ray interaction-volume (information from ~1 μm in depth). The grain size was calculated from XRD data using the Warren-Averbach (W-A) method [77,90] and compared to the obtained through I-A. The W-A analysis was carried out using the {100} and {200} peaks shown in Figure 5.10. Grain size distribution was also studied by EBSD at the surface of the samples. This technique provides information from a large area of the sample (up to 1 mm^2). Due to the limitation in lateral resolution of EBSD, the matrix composed by the smallest grains (<40 nm) could not be analysed. The EBSD pattern is composed by unresolved pixels (shown in white) and the indexed region. The comparison of the results from the I-A, EBSD and W-A analysis of the samples annealed at 750 °C is shown in Figure 5.17a. The grain size values obtained by the W-A method are 10 to 12% lower than those calculated by I-A. However, for samples with grain sizes smaller than 35 nm, the W-A method gives larger values than I-A, probably due to grain overlapping in the STEM micrographs.

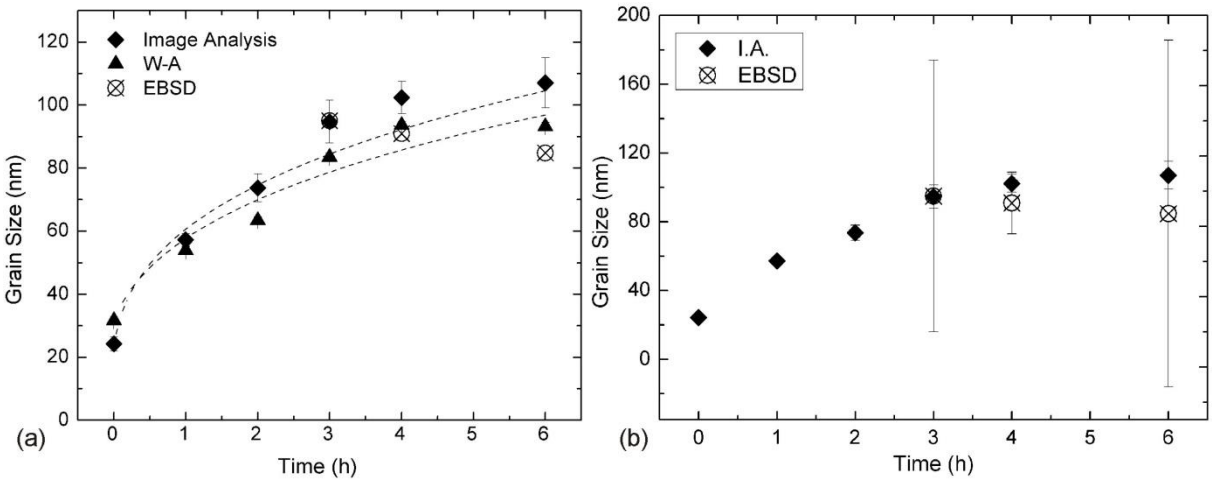

Figure 5.17: Grain size evolution for samples annealed at 750 C[17] (a) estimated by I-A, W-A and EBSD (with no error bar to allow better grain size comparison) methods; (b) the values from I-A and EBSD, showing the large error bars as a consequence of the abnormal grains detected by EBSD.

The mean grain size obtained by EBSD is comparable to those of I-A and XRD, as showed in Figure 5.17a and b. All methods for the grain size determination used in this work provided grain sizes of the same order of magnitude. However, grain sizes calculated through XRD were found to be smaller than those obtained via I-A of STEM pictures. It has been indicated by other authors [77,121] that the grain size obtained by the W-A method results, in most cases, smaller than the size obtained by TEM or STEM observations. A possible reason for this disagreement is that diffraction line broadening is not only given by crystallite size and microstrain, but also due to lattice imperfections [90]. For special case of the results presented here, in which small grains (≤35 nm) measured by the W-A method seem larger than those obtained by I-A, the overlapping of grains in STEM images is likely to be the cause. This is an usual problem in NC materials with grain sizes smaller than the foil thickness (≤100 nm).

Inverse pole figure maps obtained from EBSD analysis are shown in Figure 5.18 for samples annealed at 700 °C and 750 °C. This technique allows detection of bimodal distributions and thus, the average size obtained presents a large standard deviation due to presence of abnormal grains. In fact, 60 to 70% of the grains are concentrated in a range whose upper boundary does not exceed 80 nm and the rest is smaller than 45 nm or larger than 90 nm. Grain sizes larger than 3 μm were observed in samples annealed at 750 °C for more than 4 h, whereas at 700 °C for 6 h and 750 °C for 4 h, values of about 1.7 μm and 1.1 μm were reached, respectively. These grain sizes were, in some cases, up to four times larger than those observed by STEM. This was probably due to the cutting direction and location of the STEM foil, which could result in a smaller image projection of the abnormal grains.

17) Published: **M.A. Guitar**, K. Woll, E. Ramos-Moore, F. Mücklich, Thin Solid Films 527 (2013).

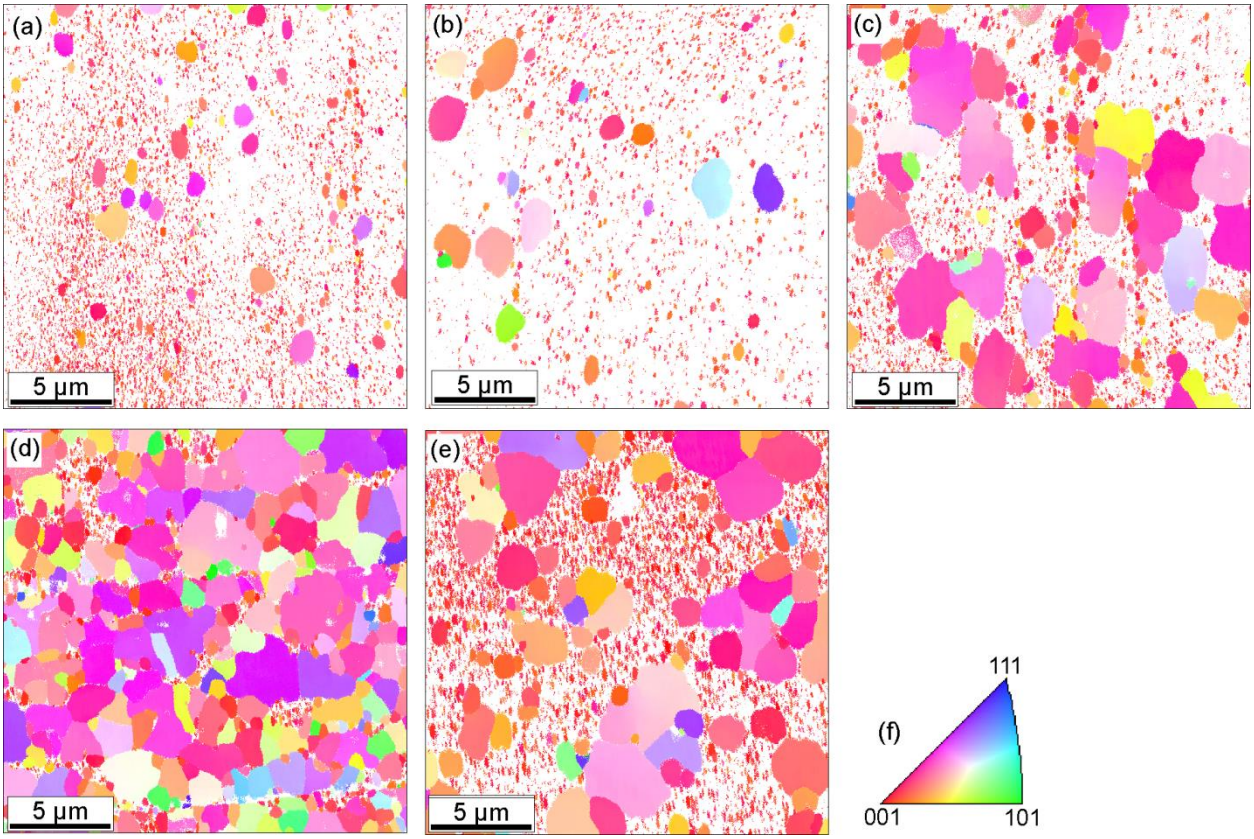

Figure 5.18: EBSD scans[18] of the surface of samples annealed at 700 °C for 6 h (a) and at 750 °C for 2 (b), 3 (c) 4 (d) and 6 h (e). A cleanup filter was applied to the scans and data with a confidence index >0.09 were used for the analysis. Their crystallographic orientation is indicated by the inverse pole figure (f) colour index.

Texture evolution of the RuAl films was analysed using the EBSD results. From the bimodal distribution acquired by this technique, the grains exceeding 1.3 µm, 0.4 µm and 0.6 µm were considered as abnormal for samples annealed at 750 °C for 3 h, 4 h and 6 h, respectively. For the sample annealed at 700 °C for 6 h, grains exceeding 0.3 µm were regarded as abnormal. Inverse pole figures of these samples are shown Figure 5.19. It is worth noting that, regardless of the annealing conditions, abnormal grains show different planes parallel to the surface with respect to normal grains, going from <001> through <114>, <113> and <112> directions, as if tending to the <111> orientation.

18 Published: **M.A. Guitar**, K. Woll, E. Ramos-Moore, F. Mücklich, Thin Solid Films 527 (2013)

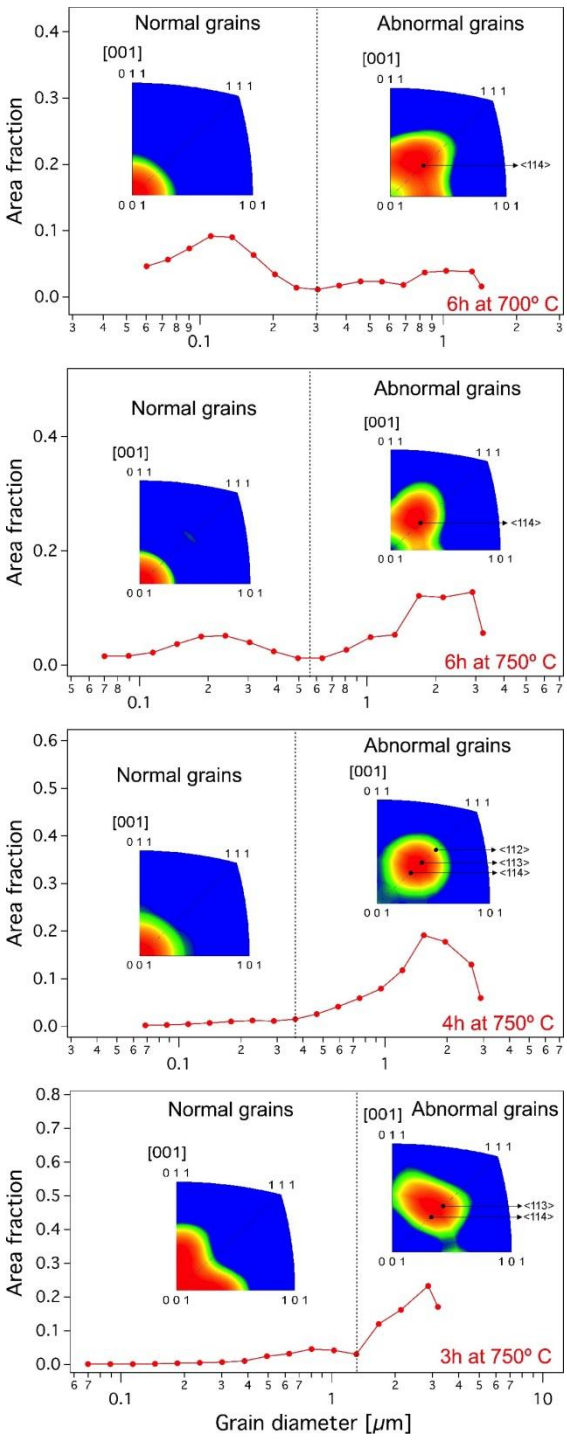

Figure 5.19: Grain size distributions and inverse pole figures obtained by EBSD analysis[19], considering bimodal distribution with normal (left) and abnormal (right) grain growth. The [001] direction corresponds to the normal of the sample surface and the normalised intensity scale is linear between blue (minimum) and red (maximum).

Abnormal grain growth in RuAl/SS could be the result of a change in grain boundary energy at the surface and film/substrate interface [105,107]; the presence of impurities and/or precipitates [93,112]; and grain-orientation-specific driving forces. From STEM analysis (Figure 5.14), it is

19) Published: **M.A. Guitar**, K. Woll, E. Ramos-Moore, F. Mücklich, Thin Solid Films 527 (2013)

worth noting that abnormal grains did not reach the film/substrate interface. Therefore, energy minimisation could not be the mechanism responsible for the abnormal growth here. The presence of even a small concentration of impurities or second phase particles could also modify the mobility of grain boundaries [109], allowing the growth of an individual subpopulation of grains. In this case, abnormal growth appears when the mobility of grain boundaries between abnormal and normal grains is much higher than between normal grains. Most grains in a strongly textured material show low-angle boundaries and consequently low mobility. Grains whose crystallographic orientation significantly differs from that of the normal matrix grains show high-angle boundaries with high mobility, making grain growth in different directions more probable [110,122]. In the case of RuAl films, grains with normal growth presented low angle boundaries (≤10°), whereas those growing abnormally showed high-angle boundaries (≥15°), as also determined from EBSD analysis, partially confirming the higher GB mobility related to the abnormal grains.

A grain boundary intersecting the film surface may lead to the formation of grooves, producing grain growth stagnation [106,110,123]. Moreover, grains possessing different surface energies which meet the surface will compete for growth [123]. Therefore, grains whose crystallographic orientation minimise surface energy tend to grow preferentially, and can reach sizes up to 4 times the film thickness [123]. Minimum surface energy was determined for the {110} orientation in B2-NiAl [124], since it shows a uniform stoichiometric composition. Given that RuAl possesses the same crystallographic structure as NiAl, abnormal grains might be expected to grow following the <110> direction, in order to minimise the total surface energy. However, EBSD measurements in RuAl films did not evidence this texture generation of the abnormal grains, but a tendency for the <111> direction (Figure 5.19). Thompson and Carel [110] argued that texture, developed as result of surface-energy minimisation, might not be the same as that from strain-energy minimisation. They developed a texture map resulting from grain growth in thin films (Figure 5.20). At low temperatures, grain growth in thin films leads to texture evolution resulting from surface-(interface)-energy minimisation. Otherwise, for thicker films at elevated temperatures, texture develops in order to minimise strain energy. An extrapolation of the map was incorporated in Figure 5.20, in order to include the conditions for the RuAl films. From this, it can be argued that the texture generated by abnormal grains evolve reducing the strain-energy density. However, this should be confirmed in further studies.

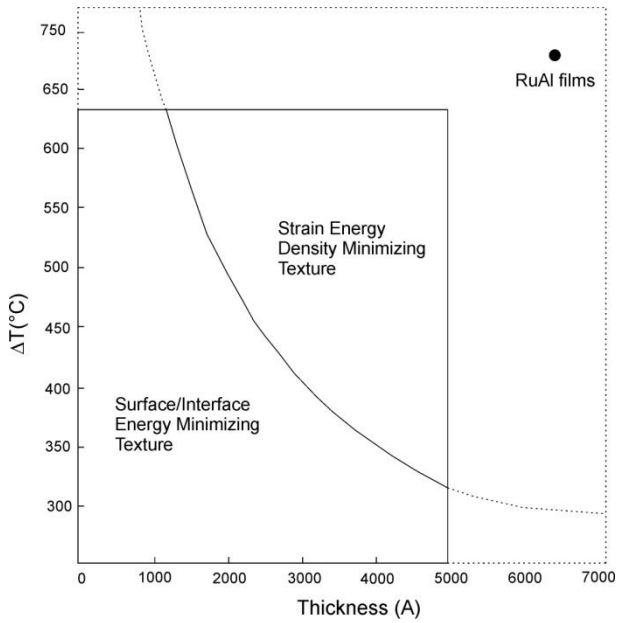

Figure 5.20: texture map for grain growth in films of thickness *h*. At low ΔT and h, surface and interface-energy minimising textures are favoured. At high ΔT and *h*, strain-energy minimising textures are favoured [110]. An extrapolation of the map was made including the conditions for RuAl films.

A relatively high level of impurities was measured in the RuAl films after the annealing process. A preliminary EDX analysis performed on the centre of RuAl thin films showed the existence of ~3.0 at.% to 3.5 at.% of Fe and ~1.5 at.% to 2.0 at.% of Cr in the samples annealed at 700 °C and ~6.0 at.% of Fe and ~3.0 at.% of Cr when annealed at 750 °C. Fe and Cr in the RuAl films content is a function of the temperature and time, and are consequence of a diffusion process of substrate elements through the Ti adhesion interlayer from the substrate. Nevertheless, no precipitates containing Fe or Cr were observed throughout the performed analysis. The isothermal section of the Ru-Al-Fe alloy diagram [92] shows solubility up to 15 at.% of Fe in RuAl, thus the formation of compounds is not expected at the impurity concentration found in this work. Therefore, impurities might remain segregated at grain boundaries or in the form of RuAl(Fe) of RuAl(Cr) [93]. The presence of impurities at GBs can induce grain growth stagnation and abnormal growth [109]. When GBs move, the segregated atoms attempt to remain with them, forcing the grain borders to drag its impurity load. Therefore, they can only migrate as fast as the slowest moving impurities [106]. The presence of impurities slows down or even stops the normal behaviour and, with sufficient time, the abnormal grains can change the complete crystallographic orientation of the sample, as shown in Figure 5.19:. In NC RuAl produced by mechanical alloying, the grain growth stagnation was attributed to impurity drag-controlled grain boundary migration, given the increased concentration of impurities along grain boundaries during this process [93].

As previously mentioned, impurities can be located not only at GBs but also occupy sites in the RuAl lattice. For this reason, the variation in the lattice parameter, as a result of impurity (Fe and Cr)

diffusion into the RuAl lattice, was analysed by in situ HT-XRD measurements. RuAl films deposited onto Al_2O_3 substrates were also analysed (see Annexe for more information), in order to avoid the effect of impurities in the lattice parameter evolution. The {100}, {200} and {300} XRD reflections were considered for the calculation of the lattice parameter using the method for *precise lattice parameter determination* (using the Nelson-Riley equation) [125].

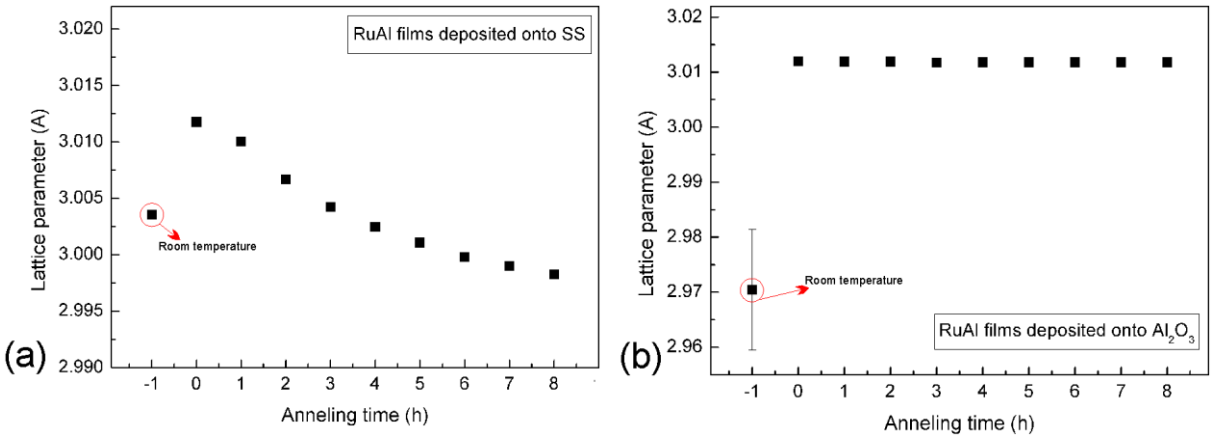

Figure 5.21: lattice constant as a function of annealing time, measured in-situ at 750 °C. The measurements at t = -1 and t = 0 correspond to the sample being at room temperature and arriving at the measurement temperature (750 °C), respectively. (a) RuAl/SS influenced by impurity diffusion and (b) impurity-free RuAl/Al_2O_3. The respective error bars are too small to be devised.

At room temperature, the lattice parameters of RuAl on SS and Al_2O_3 were 0.300 nm and 0.297 nm, respectively, which differ from that of the bulk (0.299 nm) [2,31]. An increase in the lattice parameter has been observed in both samples when the temperature was raised from RT to 750 °C. Since the lattice parameter of both samples was found to be almost the same when reaching 750 °C (point at t = 0), their difference at RT should be attributed to stresses present in the samples (compressive for RuAl/SS and tensile for RuAl/Al_2O_3), which are mostly due to the mismatch in the CTE (see section 4.2.4) and thus, should relax by reaching the annealing temperature. During the annealing, a continuous decrease in the lattice constant of the RuAl/SS sample was observed. However, for the RuAl/Al_2O_3 it remained constant during the whole process, as shown in Figure 5.21. Considering that the atomic sizes of Cr (0.139 nm) and Fe (0.123 nm) are smaller than that of Ru (0.189 nm), the decreasing of lattice constants with time in the RuAl/SS samples (and consequently with grain size) indicates the transfer of Fe and Cr into the RuAl grains. Liu [93] determined the presence of Fe as a substitutional atom in the Ru position, when studying the thermal stability of NC RuAl produced by MA. However, he observed diffusing Fe leaving the RuAl matrix during grain growth. Additional APT experiments in RuAl/SS films (see section 6.4.1) show that Fe and Cr are also present at RuAl grain boundaries.

The activation energy for grain growth Q can be estimated by measuring the growth rate k of the average grain size at different temperatures. k is ruled by the Arrhenius relationship presented in

Equation 5.10 [119], where k_0 is a constant, R is the universal gas constant and T is the temperature in Kelvin.

$$\mathbf{k = k_0\ exp(\frac{-Q}{RT})} \qquad \text{or} \qquad \mathbf{ln(k) = ln(k_0) + (\frac{-Q}{RT})} \qquad (5.10)$$

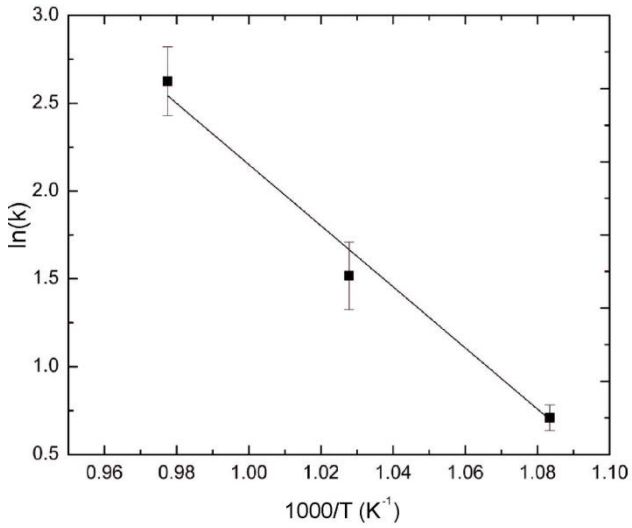

Figure 5.22: Arrhenius plot for the estimation of the activation energy of grain growth[20].

In the present work, k was calculated considering the samples annealed at 650 °C, 700 °C and 750 °C, for 6 h. Figure 5.22 shows the plot of ln(k) as a function of 1/T. The activation energy of grain growth has been estimated from the slope of the linear least-squares fit shown in Figure 5.22, and it was found to be $Q_{NC\ RuAl}$ = 145 ± 14 kJ/mol, which is comparable to the value observed in NC NiAl (166.7 kJ/mol) [119]. Lower values of Q have been previously found by Liu *et al*. [93] for NC RuAl produced by mechanical alloying. They observed that growth stagnation occurs after annealing for 3 h due to the presence of impurities (Mn, Cr and Fe), which retard grain growth by "solute drag" of grain boundary movement. They stated that impurity segregation on grain boundaries reduces the specific grain boundary energy and, therefore, the driving force for grain growth. Data regarding to activation energy of grain growth in NC materials is often compared to the activation energy associated with diffusion in the lattice (Q_l) and grain boundaries (Q_{gb}) of the CG compound, in order to determine the mechanisms involved in the grain growth process. For most pure-metals, the ratio Q_{gb}/Q_l ranges between 0.4 and 0.6 [126]. The activation energy for grain growth which has been determined in this work is much lower than the activation energy for lattice interdiffusion of conventional CG RuAl (236 ± 18 kJ/mol) [34]. The ratio $Q_{NC\ RuAl}/Q_{CG\text{-}RuAl}$ is 0.61 ± 0.01, suggesting that grain growth in NC RuAl is dominated by grain boundary diffusion. This is expected to be the case, since in NC films the volume fraction of grain boundaries is much higher than in CG materials.

20) Published: **M.A. Guitar**, K. Woll, E. Ramos-Moore, F. Mücklich, *Thin Solid Films 527* (2013)

5.5. Summary and outlook

Phase stability of RuAl thin films was observed after thermal treatments at 750 °C for 6 hours. XRD measurements on RuAl thin films annealed at 650 °C, 700 °C and 750 °C for 6 h showed only B2-RuAl intermetallic, presenting a preferred crystallographic orientation along the {100} planes being parallel to the surface. This preferred orientation has been maintained, in all cases, after annealing during 6 h at 650, 700 and 750 °C.

Thermal studies showed that temperatures as low as 650 °C are not sufficient to activate grain growth. However, annealing at 700 °C and 750 °C increased the grain size, going from about 24 nm at room temperature up to 54 nm and 107 nm, respectively. The isothermal grain growth in RuAl thin films obeys the generalised power model and its exponent *n* was found to depend on the temperature. For most of the temperatures and times used, normal grain growth of RuAl films has occurred. However, abnormal growth was observed when annealing for 6 h at 700 °C and for 4 h and 6 h at 750 °C. From the available mechanisms of abnormal growth, we conclude that the presence of impurities and grain-orientation-specific driving forces were responsible for the observed behaviour. Furthermore, the film texture evolves tending to minimise the strain energy density.

The diffusion of Fe and Cr from the substrate and their subsequent incorporation into the RuAl lattice as substitutional elements has been verified by the variation of the lattice parameter, which reduces its value as the impurity level increases with annealing time. The corresponding activation energy for grain growth in NC RuAl has been found to be 145 ± 14 kJ/mol, in agreement with reported values for other B2 NC intermetallic compounds. The ratio of the activation energy for lattice diffusion (from literature) and the obtained from this work was 0.61 ± 0.01. This indicates that grain growth in NC RuAl is highly dominated by grain-boundary diffusion, given the high volume fraction of grain boundaries in comparison to CG-materials.

6

Oxidation behaviour of RuAl thin films

The present chapter details the studies performed on the oxidation behaviour of NC RuAl thin films deposited onto austenitic SS (RuAl/SS). The possibility of chemical interaction at the substrate/film interface at high temperatures has also been considered. In particular, diffusion of Cr and Fe from the SS substrate is likely to occur during oxidation at high temperature. By using Al_2O_3 as a substrate (RuAl/Al_2O_3), which avoids impurity diffusion into the RuAl film, the influence of impurities on the oxidation behaviour could be evaluated. Additionally, the effect of diffusion barriers (Al_2O_3 and W films) deposited between the substrate and the RuAl film was analysed.

The results exposed in the present chapter gave rise to two peer reviewed publications: **M.A. Guitar**, F. Mücklich; *Isothermal Oxidation Behaviour of Nanocrystalline RuAl intermetallic thin films,* Oxidation of Metals 80 (2013); and **M.A. Guitar**, E. Ramos-Moore and F. Mücklich; *The influence of impurities content in the formation of protective aluminium oxides on RuAl thin films,* Journal of Alloys and Compounds (2014), DOI: 10.1016/j.jallcom.2014.01.137.

6.1. Introduction

The oxidation resistance depends on the formation of a protective surface oxide. Materials for high temperature applications are designed to form α-Al_2O_3, Cr_2O_3 and SiO_2, which are stable and low-growth rate oxides. The physical, chemical and structural properties of metals, as well as the specific oxidation conditions, might affect the final oxide formed at the metal surface. It must act as a barrier keeping the oxygen and metal atoms separated from each other, thus reducing the rate at which they react. Ideally, the oxide layer should be highly stable, continuous, slow growing, free from cracks or pores, adhesive and coherent. α-Al_2O_3 comes close to satisfying these requirements.

Its slow growth rate is related to the highly stoichiometric composition and large band gap, which makes electronic conduction difficult [95].

The RuAl intermetallic compound (IMC) has shown good oxidation resistance up to at least 1100 °C, due to the formation of a dense and compact Al_2O_3 scale (see also section 1.3.2) [61,127]. The coefficient of thermal expansion (CTE) mismatch between Al_2O_3 and RuAl is practically negligible in a wide temperature range [46]. Consequently, the corresponding generation of thermal stresses is avoided, or at least minimised, and the adherence of the protective layer increases during thermal cycling and cooling from high temperatures.

The physical and mechanical properties of IMCs are highly dependent on chemical composition. Hence deviation from stoichiometry can affect their oxidation resistance. The excess of one element in off-stoichiometric intermetallic phases is accommodated in the form of point defects, affecting their conductivity, diffusion mechanisms or slip behaviour, among other properties [18,128]. In the particular case of RuAl and other aluminides (e.g. NiAl), the oxidation behaviour is very sensitive to microstructure and chemical composition [37,43,129]. This is because IMCs existing in a narrow composition range tend to show second-phase precipitation at grain boundaries (GBs) when deviating from stoichiometry, which is also detrimental for oxidation resistance. Previous studies on the oxidation of bulk RuAl-based alloys showed that two-phase microstructure (i.e. RuAl + δ-Ru) and non-stoichiometric composition (Ru-rich) affect negatively the oxidation behaviour [37,43,127,130]. This is due to the formation of volatile Ru oxides [42,43], whose evaporation alters the growth of a compact Al_2O_3 layer, as observed by Bellina *et al*. [130]. On the other hand, an enhancement of the oxide adherence during exposure to thermal-cycles was observed by Cao *et al*. [131], by adding platinum to RuAl-based alloys.

During oxidation at elevated temperatures, some components of the alloy can be incorporated into the growing Al_2O_3 scale, in form of oxides formed at the first stages of the oxidation process or by later segregation at GBs. These impurities added to the oxide layer could affect the transport rates of oxygen and/or aluminium, altering the Al_2O_3 growth process [132]. The influence of the Fe and Cr content in the formation of α-Al_2O_3 from one of its transient oxides has been presented in several works [133–136]. Most of them referred that the presence of Cr in some alumina-forming alloys and IMCs allows the growth of α-Al_2O_3 instead of transient oxides. Although it is clear that oxidation behaviour in IMCs is affected by the presence of reactive elements or impurities, there is still a lack of studies regarding oxidation kinetics and stress on the aforementioned system.

Bulk intermetallics usually show different oxidation rates in comparison to thin films. Consequently, for future application of RuAl thin films, knowledge of the kinetics and oxidation behaviour of this IMC is required.

6.2. Fundamentals of oxidation of metals

6.2.1. Thermodynamic fundamentals of oxidation

The study of oxidation in metals is related to determining which reactions are energetically possible. The thermodynamic equilibrium is defined in terms of Gibb's free energy variation, ΔG (Equation 6.1), which depends on the variation of enthalpy and entropy [95].

$$\Delta \boldsymbol{G} = \Delta \boldsymbol{H} - \boldsymbol{T}\Delta \boldsymbol{S} \qquad (6.1)$$

A chemical process occurs spontaneously by releasing energy ($\Delta G<0$); it remains in equilibrium if $\Delta G=0$; and is thermodynamically impossible if $\Delta G>0$.

For a certain oxidation reaction $\left(M + O_2 \rightarrow MO_2\right)$ where a metall atom (M) combines with oxygen, the variation in free energy is given by Equation 6.2.

$$\Delta \boldsymbol{G} = \boldsymbol{G_{MO_2}} - \boldsymbol{G_{O_2}} - \boldsymbol{G_M} \qquad (6.2)$$

The free energy of a component can be described as in Equation 6.3, where R is the universal gas constant, T the absolute temperature and a_i the thermodynamic activity.

$$\mathbf{G_i} = \mathbf{G_i^0} + \mathbf{R\ T\ ln(a_i)} \qquad (6.3)$$

The oxidation reaction can then be expressed in terms of free energy, as shown in Equation 6.4.

$$\Delta \mathbf{G} = \Delta \mathbf{G^0} + \mathbf{R\ T\ ln}\left(\frac{\mathbf{a_{MO_2}}}{\mathbf{a_M a_{O_2}}}\right) \qquad (6.4)$$

In equilibrium, the free energy of the system is given by Equation 6.5. The term in parentheses is known as the equilibrium constant (K) and is used to describe the equilibrium state of the reaction system.

$$\Delta \mathbf{G^0} = -\mathbf{R\ T\ ln}\left(\frac{\mathbf{a_{MO_2}}}{\mathbf{a_M a_{O_2}}}\right)_{\mathbf{eq.}} \qquad (6.5)$$

When more than one element is able to oxidise in an alloy, the determination of the most stable corrosion product is of high technological importance. Elligham diagrams (Figure 6.1) allow a direct comparison of the relative stability of each compound. They show the standard free energy of formation (ΔG^0) versus temperature for the most common oxides.

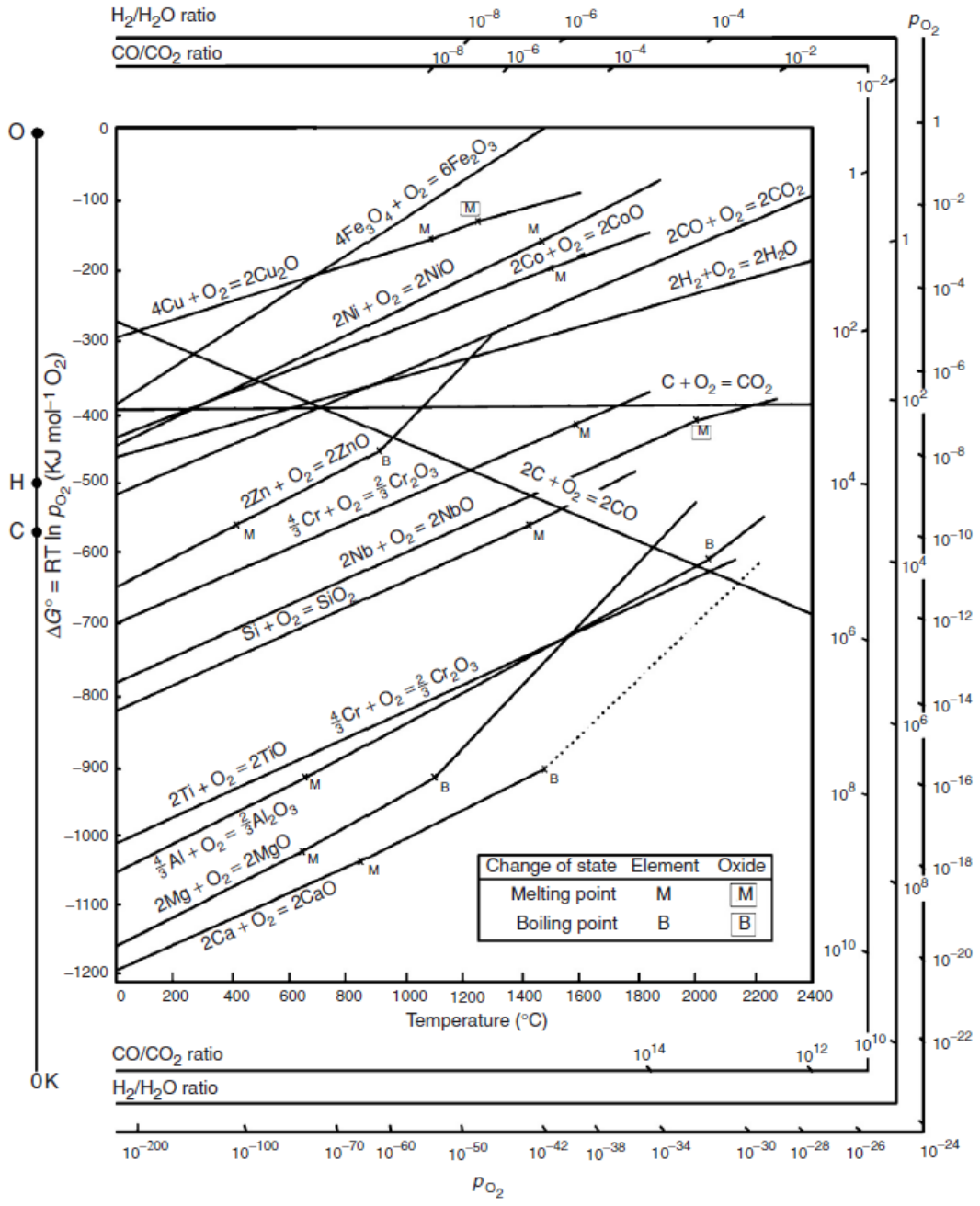

Figure 6.1: Ellingham diagram showing the standard free energy of formation of selected oxides as a function of temperature. The lower the position of the line on the diagram, the more stable the oxide [95].

In the case of the RuAl system, the stable oxides are RuO_2 and Al_2O_3. However, at the current analised temperatures (750 and 900 °C), aluminium oxide is thermodynamically favoured against Ru oxide, as indicated by the free energy of formation [137]:

$$Ru + O_2 \rightarrow RuO_2 \qquad \frac{4}{3}Al + O_2 \rightarrow \frac{2}{3}Al_2O_3$$

$$\Delta G^{750}_{RuO_2} = -143.25\ \text{kJ/mol} \qquad \Delta G^{750}_{Al_2O_3} = -912.75\ \text{kJ/mol}$$

$$\Delta G^{900}_{RuO_2} = -110.75\ \text{kJ/mol} \qquad \Delta G^{900}_{Al_2O_3} = -869.25\ \text{kJ/mol}$$

Metal and oxide coexist at a determined vapour pressure namely, the dissociation pressure:

$$\mathbf{P_{O_2}^{M/MO_2} = exp\frac{\Delta G^0}{RT}} \qquad (6.6)$$

The equilibrium vapour pressure varies with temperature. At elevated temperatures, the formation of volatile oxides can strongly affect the oxidation behaviour. The relation between vapour pressure and partial pressure for a determined oxide is given by the vapour/pressure diagrams. In the case of ruthenium, three oxides can be formed at elevated temperature: one solid (RuO_2) and two gaseous (RuO_3 and RuO_4). Figure 6.2 plots the vapour species-diagram for Ru_xO_y at 750 °C and 900 °C.

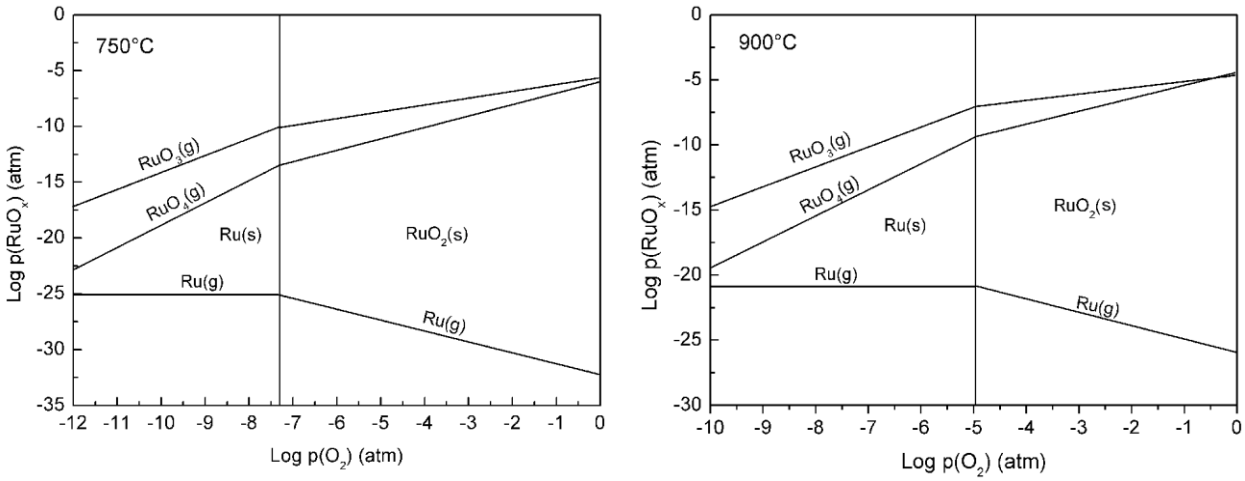

Figure 6.2: Vapour species diagram of the RuO_x system at 750 °C and 900 °C [137].

6.2.2. Oxidation kinetics fundamentals

Ellingham diagrams show the thermodynamics of reactions and give information about oxide formation under determined conditions of temperature and oxygen partial pressure. However, it does not consider the kinetics of the reaction. In some cases, even if the reaction is thermodynamically possible, the kinetics of the processes is so slow that it would take too long to finish. A combination of thermodynamic and kinetics information gives a better understanding of the oxide behaviour.

The oxidation kinetics are determined by the transport processes in the growing scales. There are four characteristic behaviours that can be identified (Figure 6.3): linear, parabolic, logarithmic and inverse logarithmic [138].

a) **Linear oxidation:** the formed oxide layer is not protective. The oxidation proceeds at a constant rate and is independent of the amount of metal previously consumed in the reaction (Eq. 6.7).

$$\mathbf{\frac{dx}{dt} = K_l\, t} \qquad \mathbf{x = K_l\, t + D} \qquad (6.7)$$

b) **Parabolic oxidation**: the result is the formation of a continuous and dense oxide layer. Its growth occurs with a decreasing oxidation rate, which is inversely proportional to the scale thickness or the weight of the formed oxide (Eq. 6.8).

$$\frac{dx}{dt} = \frac{K_p}{x} \qquad x^2 = 2\,K_p\,t + C \qquad (6.8)$$

c) **Logarithmic oxidation (direct and inverse)**: is the case of most metals heated to low temperatures and it is associated with very thin oxide films (2-4 nm). The reaction rate rises very fast in the beginning and then slows down (Eq. 6.9).

$$x = K\,\log\,(t) + A \qquad (6.9)$$

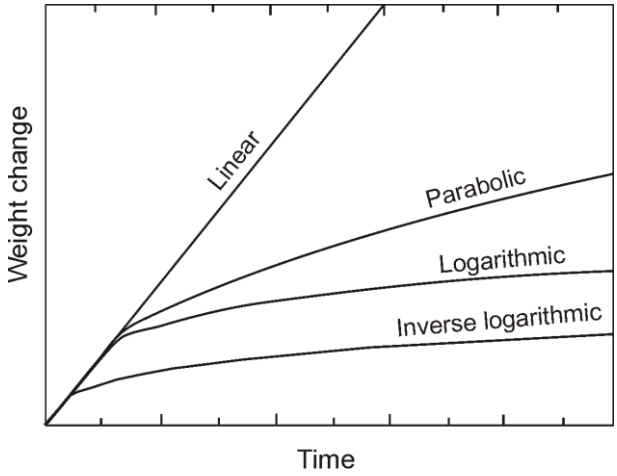

Figure 6.3: Oxidation kinetics obeying different growth behaviours [138]. In some cases, it is not possible differ between the oxidation behaviours at the initial stages of oxidation (short oxidation times).

Most metals forming protective oxide scales follow parabolic kinetics at elevated temperatures. The growth of a protective and continuous oxide scale can be described as the result of an electro-chemical migration of different species (anions, cations and electrons) through the initially formed oxide scale. Diffusion occurs via lattice defects under the influence of an electrochemical potential gradient, as described in Figure 6.4. In this case, thermodynamic equilibrium is assumed to exist at the metal-oxide and oxide-gas interfaces. The mechanisms of parabolic oxide growth involve the outward diffusion of M^{2+} and two electrons through the film to meet the O^{2-}at the outer surface or the inward movement of oxygen (with two electron holes) to meet the M^{2+} at the inner surface [95].

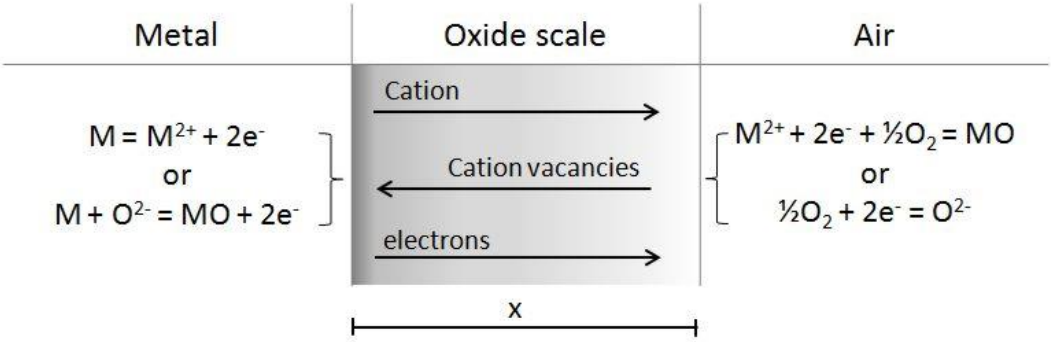

Figure 6.4: Simplified model for diffusion-controlled oxidation [139]. Two steps are needed for the reaction $M + O \rightarrow MO$: first M forms ions, releasing electrons ($M \rightarrow M^{2+} + 2e$). These electrons are then absorbed by oxygen to give an oxygen ion ($O + 2e \rightarrow O^{2-}$).

6.2.3. Oxidation of alloys

Alloy oxidation can be much more complex than that of pure metals. The difference in oxygen affinity of the metals conforming an alloy, can lead to the growth of complex oxides, formation of sub-scales or even internal oxidation. The dissimilar mobilities of the various metals present in the oxide phases and in the alloy can alter the oxidation kinetics. Moreover, the dissolution of oxygen into the alloy may result in internal oxidation of one or more of its elements [95]. In the case of alloys containing noble metals (which do not form stable oxides under normal conditions) and elements such as Cr, Cu, Fe, Al, Ti, etc. (which form stable oxides), the less noble metal will oxidise.

At the first oxidation stages, oxygen begins to dissolve into the alloy. However, due to the low oxygen solubility in noble metals, the oxide cannot nucleate internally. Hence the most reactive metal (B) diffuses outward to form a continuous BO layer [95]. Simultaneously, the most noble metal (A) concentrates at the scale/oxide interface, as shown in Figure 6.5. Therefore, the reaction rate is limited by the supply of B atoms from the alloy to the oxide/metal interface or by the migration of B ions through the oxide to the scale/gas interface. The first case is rate-determining when the concentration of B in the alloy is low, whereas the last is rate-determining when the concentration of B is high. Both processes are diffusion-controlled and, therefore, lead to parabolic kinetics.

The minimal concentration of reactant B required to grow a continuous oxide layer by diffusion in the alloy is given by Equation 6.10 [140], where V_M is the molar volume of the alloy, Z_B the valence of B atoms, M_{ox} the atomic weight of the oxide, D_B the diffusion coefficient of B in the alloy and k_p the parabolic rate constant for oxidation.

$$\mathbf{N_B} = \frac{\mathbf{V_M}}{\mathbf{z_B\, M_{0x}}}\left(\frac{\pi \mathbf{k_p}}{\mathbf{D_B}}\right)^{\mathbf{1/2}} \qquad (6.10)$$

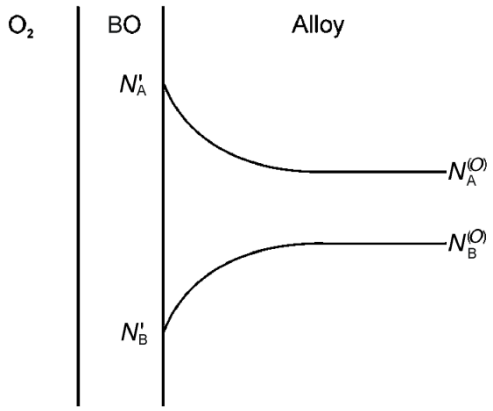

Figure 6.5: Schematic concentration profiles for the oxidation of an AB alloy, being A and B the most noble and reactive metal, respectively [95].

The oxidation mechanism becomes more complex when an alloy possesses two or more elements prone to oxidise, as is the case with Ti-Al compounds or Ti-Cr-Al alloys [8]. They form oxides of different stability and at different rates, where the formation of ternary products can also occur.

Considering an AB alloy with oxidisable components, B forming stabler oxides than A: several oxide morphologies might be observed depending on the concentration of each element and their variation during the scale thickening, as shown in Figure 6.6.

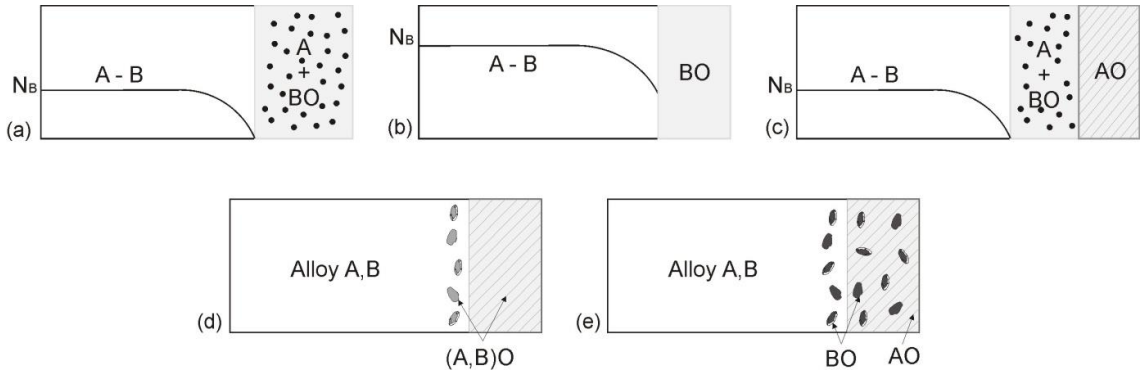

Figure 6.6: Schematic diagram of the oxidation of an A-B alloy, for which both elements are able to form oxides. (a) Only minor element B oxidises, producing internal oxide BO within a matrix of A; (b) only minor element B oxidises, resulting in the growth of a continuous external layer of BO; (c) external oxide A and internal oxidation of minor B; (d) A and B oxidise to produce single solid solution or compound of variable composition (A,B)O; (e) A and B oxidise, resulting in insoluble oxides, with BO within a matrix of AO [95].

Alloys with low solute concentration allow inward diffusion of oxygen, which results in internal oxidation. For high solute contents, the outward diffusion of solute results in the formation of a continuous external layer of oxide. The critical solute concentration for the transition between internal and external oxidation is given by Equation 6.11 [141], where N_0D_0 is the oxygen permeability in A, D_B the solute diffusivity, g^* a factor determined by the volume fraction of oxide

required for the transition and V_M and V_{ox} are the molar volumes of the metal and the oxide, respectively.

$$\mathbf{N_B^* = \left(\frac{\pi g^* N_0 D_0 V_M}{2 D_B V_{ox}}\right)^{1/2}} \qquad (6.11)$$

In the particular case of IMCs, other mechanisms must also be considered. Internal oxidation as described in Figure 6.7c and d is not commonly found due to the negligible oxygen solubility of most intermetallics [141]. Furthermore, the limited composition existence region of an intermetallic phase (for RuAl see section 1.3.2) leads to selective oxidation of one of its components. This results in the formation of a less stable compound immediately below the oxide. Therefore, the ability of the alloy to maintain the growth of the protective oxide is determined by the properties of that compound. The concentration of the oxidised element must be sufficient for the formation and continuous growth of the oxide layer.

Figure 6.7: Schematic diagrams showing the special features involved in the oxidation of intermetallic compounds with narrow ranges of stoichiometry. (a) Growth of external oxide layer of element B and formation of the sub-stoichiometric intermetallic beneath the oxide (e.g. $MoSi_2$ system); (b) growth of stable B oxide, leading to the formation of a mixed oxide (e.g. $NbAl_3$); (c) oxides of A and B compete to grow, leading to the formation of mixed oxides (e.g. TiAl) [141].

6.2.4. Diffusion barriers

Diffusion barriers (DB) act as an obstacle, protecting one of the components (RuAl films in this case) from being degraded by the other (substrate elements diffusing into RuAl). They are generally thin layers (from nm to μm thickness) of a metal or compound synthesised between a substrate and a coating or between two elements composing the coating architecture, as shown in Figure 6.8.

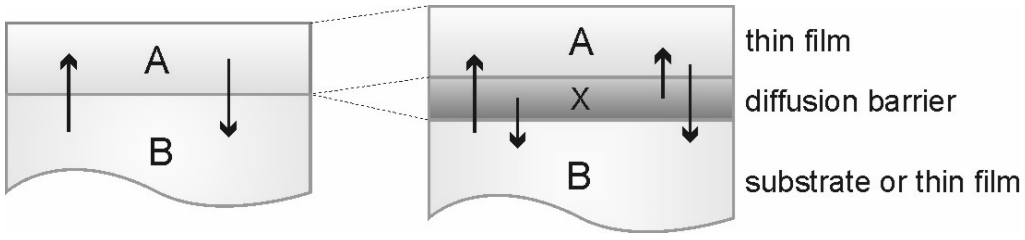

Figure 6.8: Diffusion barrier between thin film and substrate preventing their intermixing [142].

An ideal DB physically separates materials A and B via an interposed layer of material X, chosen so that under given external conditions the undesirable intermixing of A and B is suppressed (Figure

6.8). The atomic transport rate of A and B across X should be close to zero, just as that of X into A and B. Moreover, X should be thermodynamically stable in presence of A and B [142].

6.3. Experimental

The present work studies the oxidation behaviour of RuAl films deposited (Section 4.2.1) onto SS (RuAl/SS) and Al_2O_3 (RuAl/Al_2O_3) substrates. Before oxidation, RuAl films present a grain size of about 24 nm (see section 5.4) and non-stoichiometric composition, as shown in Table 6.1. The oxidation experiments have been carried out isothermally in air at **750 °C** and **900 °C** for the **RuAl/SS** samples, and only at 900 °C for the **RuAl/Al_2O_3**, during 10 min to 60 min. The activation energy for oxidation was calculated using an Arrhenius model with data from samples oxidised for 20 min at temperatures between 750 °C and 1000 °C (with 50 °C steps). The samples were placed in the furnace at the oxidation temperature for the desired time and then removed and cooled down to room temperature. No special atmosphere was used. Microstructural and stress analysis was performed using STEM, TEM (preparation by FIB milling, see Section 3.1.3) and XRD (Cu Kα radiation at 40 kV and 40 mA in a PANalytical X'Pert Pro MPD X-ray diffractometer). EDX measurements were done on the 100 nm thin STEM foils. Pulsed laser atom probe tomography (APT) was performed to analyse the impurity content in both the oxide scale and metallic film (see 3.4).

Table 6.1. Chemical composition before oxidation of the RuAl films deposited onto SS and Al_2O_3 substrates. The error in the measurement corresponds to that of the EDX instrument (~1%).

	Chemical composition		
	$RuAl_{(Ru\text{-}rich)}$/SS	**$RuAl_{(Ru\text{-}rich)}/Al_2O_3$**	**$RuAl_{(Al\text{-}rich)}/Al_2O_3$**
Ru	51 at.%	54 at.%	48 at.%
Al	45 at./	46 at.%	52 at.%
Fe	~3 at.%	-	-
Cr	~1 at.%	-	-

6.4. Results and Discussion

6.4.1. Microstructural analysis of the oxidised RuAl films deposited onto SS substrates

During oxidation at 750 °C and 900 °C, a regular, compact, homogeneous oxide layer was formed at the surface of the RuAl films, covering the whole sample. Samples oxidised for less than 30 min showed a smooth oxide surface (Figure 6.9a). However, at 900 °C after 30 min, the oxide acquired a blade-like morphology and after 60 min, ca. 250 nm long platelets were observed (Figure 6.9b). The oxide was identified by XRD as α-Al_2O_3, with no transient alumina detected for any of the

temperatures and times studied here (Figure 6.10). Bladelike morphology was also observed in bulk RuAl after isothermal oxidation at 1000 °C for 300 h [127], the result of a rapid local outward diffusion of Al cations [9,127,143]. This morphology has been associated in NiAl and other aluminides with the growth of transient θ-Al_2O_3,which precedes the formation of α-Al_2O_3 [10,144,145]. In NiAl and FeAl, metastable Al_2O_3 is formed at temperatures below 900 °C [9,10]. At 750 °C, γ-Al_2O_3 is expected to grow in NiAl, whereas at 900 °C, θ-Al_2O_3 is present. The nucleation of α-Al_2O_3 is only observed at 1000 °C [9]. The transformation of transient oxides (θ-Al_2O_3 or γ-Al_2O_3) into α-Al_2O_3 generates dramatic changes in the scale morphology and leads to the formation of cracks by transformation stresses [146]. However, for the samples analysed in this work and in previous bulk RuAl oxidation studies [127,130], no evidence of the presence of transient θ-Al_2O_3 has been observed, indicating that α-Al_2O_3 can also have a bladelike morphology [127,145,147] and stress generation at the film/oxide interface being minimised.

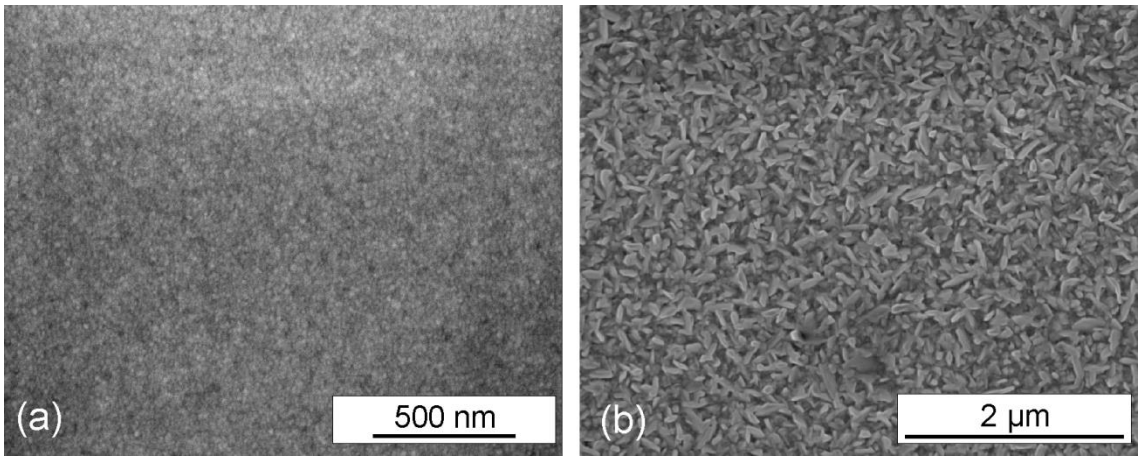

Figure 6.9. SEM images[21] of the surface of samples oxidised for 60 min at (a) 750 °C and (b) 900 °C. The oxide layer is homogeneous and covers the whole surface. A bladelike morphology was observed when oxidising for 30 min or longer at 900 °C.

STEM bright-field images of the cross-section of oxidised samples (Figure 6.11) show very regular oxide layers formed on top of the surfaces, being compact and porosity-free. Moreover, no evidence of internal or intergranular oxidation has been observed, even after 60 min at 900 °C (Figure 6.11). Beneath the oxide scale, an Al-depleted zone was observed in most of the specimens and was, as well as the bladelike morphology, a consequence of the outward diffusion of aluminium. This Al-depleted zone was identified in bulk RuAl as δ-Ru [127]. It was formed due to the relatively narrow existence range of the single-phase RuAl [2], detected in oxidised RuAl films by XRD (Figure 6.10). A discontinuous Al-depleted layer was observed beneath the Al_2O_3 in samples oxidised at 750 °C and 900 °C for 10, 20, 30 min. In all cases, this phase followed the GBs, becoming continuous only after oxidation at 900 °C for 40 min or longer.

21) Published: **M.A. Guitar**, F. Mücklich; Oxidation of Metals 80 (2013).

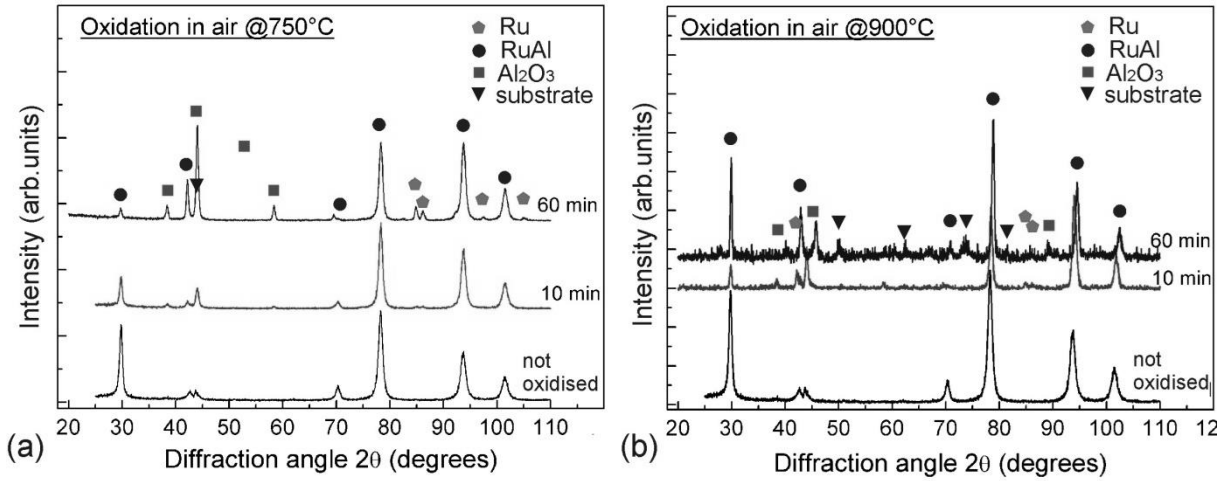

Figure 6.10. XRD diffractograms[22] (GI-configuration) of samples oxidised at (a) 750 °C and (b) 900 °C, showing the presence of only RuAl, Ru and α-Al_2O_3.

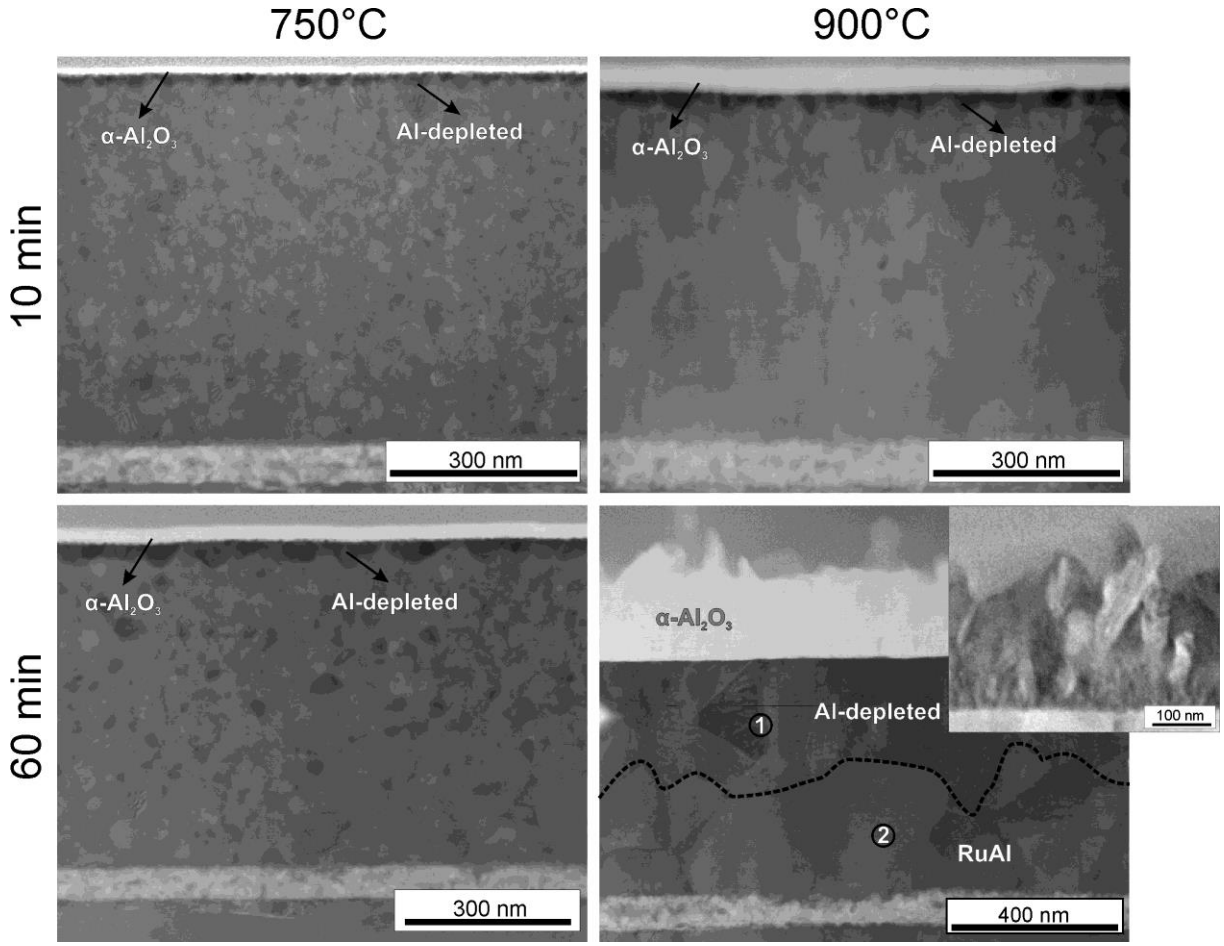

Figure 6.11. Bright field STEM image[23] of the cross-section of RuAl thin films oxidised for 10 and 60 min at 750 °C and 900 °C. The pointed line indicates the transition from the Al-depleted zone (1) to the RuAl phase (2). The inset shows a magnified image from the oxide layer.

22)and 23) Published: **M.A. Guitar**, F. Mücklich, Oxidation of Metals 80 (2013).

In XRD measurements (Figure 6.10) only RuAl, Ru and α-Al_2O_3 peaks were identified, with no RuO_2 detected. The intensity of α-Al_2O_3 peaks increased with the oxidation time, while Ru peaks showed relatively low intensity. The formation of volatile RuO_3 or RuO_4 can be dismissed due to the absence of pores in the Ru-rich layer, which are characteristic of oxide volatilisation. An Al-depleted zone has also been observed beneath the oxide layer in other aluminides [9,130,148]. However, in the particular case of NiAl, this region corresponded to NiAl phase possessing an excess of Ni, given the wide range of existence of this phase [149]. The excess Ni leads to the formation of voids and cavities in contact with the Al_2O_3 scale, as a result of Ni diffusion into the material, affecting the adherence with the subsequent detachment of the protective oxide.

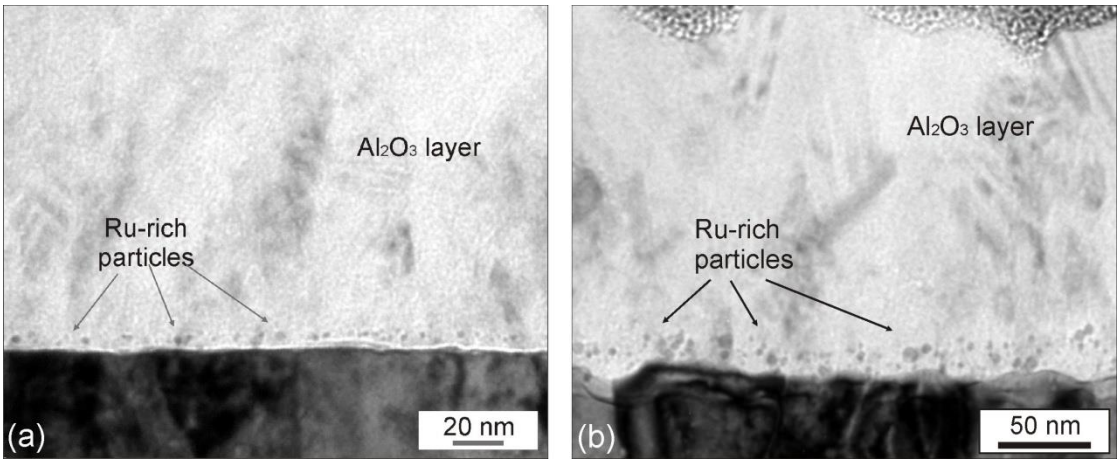

Figure 6.12: TEM image (BF) showing Ru-rich particles at the oxide/metal interface, formed at the initial stages of oxidation in a sample oxidised at 900 °C (a) for 60 min using SS substrate and (b) for 50 min using Al_2O_3 substrate.

Some particles of about 5 nm in diameter were detected at the oxide/metal interface (Figure 6.12). They were identified by Bellina *et al.* [130] as Ru-rich particles, formed at the initial stages of oxidation, when the RuAl surface was directly exposed to the oxidising atmosphere [130] and their location indicates the position of the surface before oxidation. Bellina *et al*. [130] observed them in oxidised bulk-RuAl delimiting two regions of columnar and equiaxed grains inside the oxide scale. Both types of grains grew during the oxidation reaction, suggesting simultaneous inward diffusion of oxygen and outward diffusion of Al, forming columnar and equiaxed grains, respectively. For the NC RuAl/SS studied in this work, the precipitates were located at the oxide/metal interface, indicating that the surface has not been displaced. However, the α-Al_2O_3 grown on NC RuAl/SS showed a columnar morphology (Figure 6.11), which is commonly associated to oxide growth by inward diffusion of oxygen along GBs in the columnar-grained oxide [150,151]. However, it was proposed that whiskers forming θ-Al_2O_3 are a product of the outward diffusion of Al^{3+} [152]. As previously mentioned, evidence of α-Al_2O_3 existing in form of whiskers has been observed in nanocrystalline (present work) and coarse-grained (CG) RuAl [127] and also in Fe-based and Ni-

based alumina formers and oxidised Al [145,147]. α-Al_2O_3 existing with columnar morphology (as in NC RuAl/SS) together with oxide particles, formed at the beginning of the oxidation reaction, located at the metal/oxide interface suggest that oxide growth was dominated by outward diffusion of Al.

Some level of impurity diffusion from the substrate into the RuAl layer was expected during exposure to high temperatures. The presence of impurities, especially in the oxide scale, might be detrimental for the oxidation resistance and could also affect the transport of aluminium to the intermetallic/oxide or oxide/gas interfaces. The oxide growth mechanism and the oxidation rate might also be affected by impurities (see section 6.4.4) [132,153,154]. The most abundant contaminants in a growing Al_2O_3 scale are the alloy base metals, incorporated during the initial stage of oxidation. It is believed that they segregate at oxide GBs, thus influencing the growth rate of scales. Hou *et al.* studied the impurity distribution during the oxidation of a FeCrAl alloy [155]. Before heat treatment, the native oxide contained Fe, Cr and Al. Then, a complete Al_2O_3 surface layer grew during exposure to high temperature, which fully incorporated the initially formed Fe and Cr oxides. The Fe was detected at the oxide GBs, with a higher concentration near the scale/metal interface. Additionally, in NiAl compounds, certain quantities of Cr (less than 10 at.%) can be beneficial to the formation of α-Al_2O_3, according to the observations made by Klumpes *et al.* [133]. The growth of Cr_2O_3 nuclei benefits the formation of α-Al_2O_3 at the expense of θ-Al_2O_3 by acting as a nucleation point for the θ/α transformation and resulting in finer oxide grains than in pure NiAl. Moreover, the growth of α-Al_2O_3 is also affected by the increment in grain boundary diffusion rates in presence of impurities [9].

In order to determine the impurity content in the oxide scale of RuAl/SS samples, an analysis at the atomic level was performed using APT (Figure 6.13). The only elements detected were Al and O, with no traces of Fe and Cr being found in the Al_2O_3 scale. The O/Al ratio of atoms was found to be 1.2, instead of the theoretical 1.5. This difference arose given the limited quantification capability of the detector when dealing with high percentages of multiple events (54% in this case) [156].

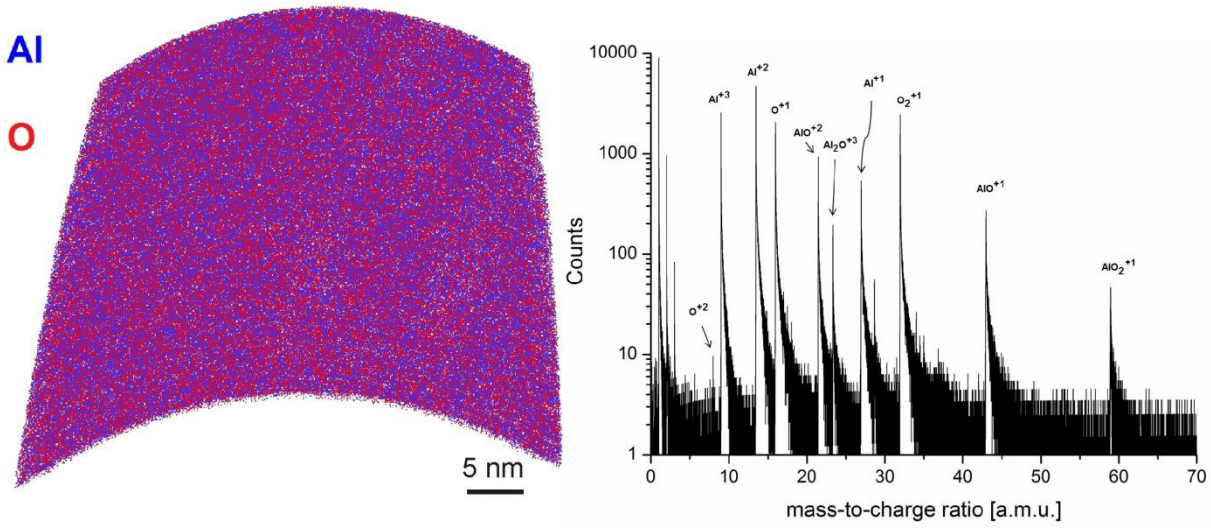

Figure 6.13: APT reconstruction of the oxide scale grown after 60 min at 900 °C (left) and mass spectrum showing only Al, O and complex ions arriving at the detector (right). No Fe or Cr impurities were detected.

Complementary chemical analysis using EDX and APT (Table 6.2) revealed that the Al-depleted zone beneath the oxide layer contained ~20 at.% Cr and ~63 at.% Fe; and the remaining RuAl phase about 11 at.% Cr and 18 at.% Fe after oxidation for 60 min at 900 °C. The corresponding APT reconstruction and chemical distribution are shown in Figure 6.14. The high concentration of Cr and Fe found in both regions of the sample was the result of element diffusion from the substrate. Additionally, excess Ru diffused from the B2-RuAl into the SS substrate was also detected by EDX.

Table 6.2: Chemical composition of the film after oxidation for 60 min at 900 °C. High levels of diffused Fe and Cr from the SS substrate were detected. The balance is given by the minor presence of other elements from the substrate. The measured locations (1 and 2) are indicated in Figure 6.11.

	Oxidised samples (900 °C/60min.)	
Position	**1**	**2**
Al	~1 at.%	~25 at.%
Ru	~12 at.%	~43 at.%
Fe	~63 at.%	~18 at.%
Cr	~20 at.%	~11 at.%

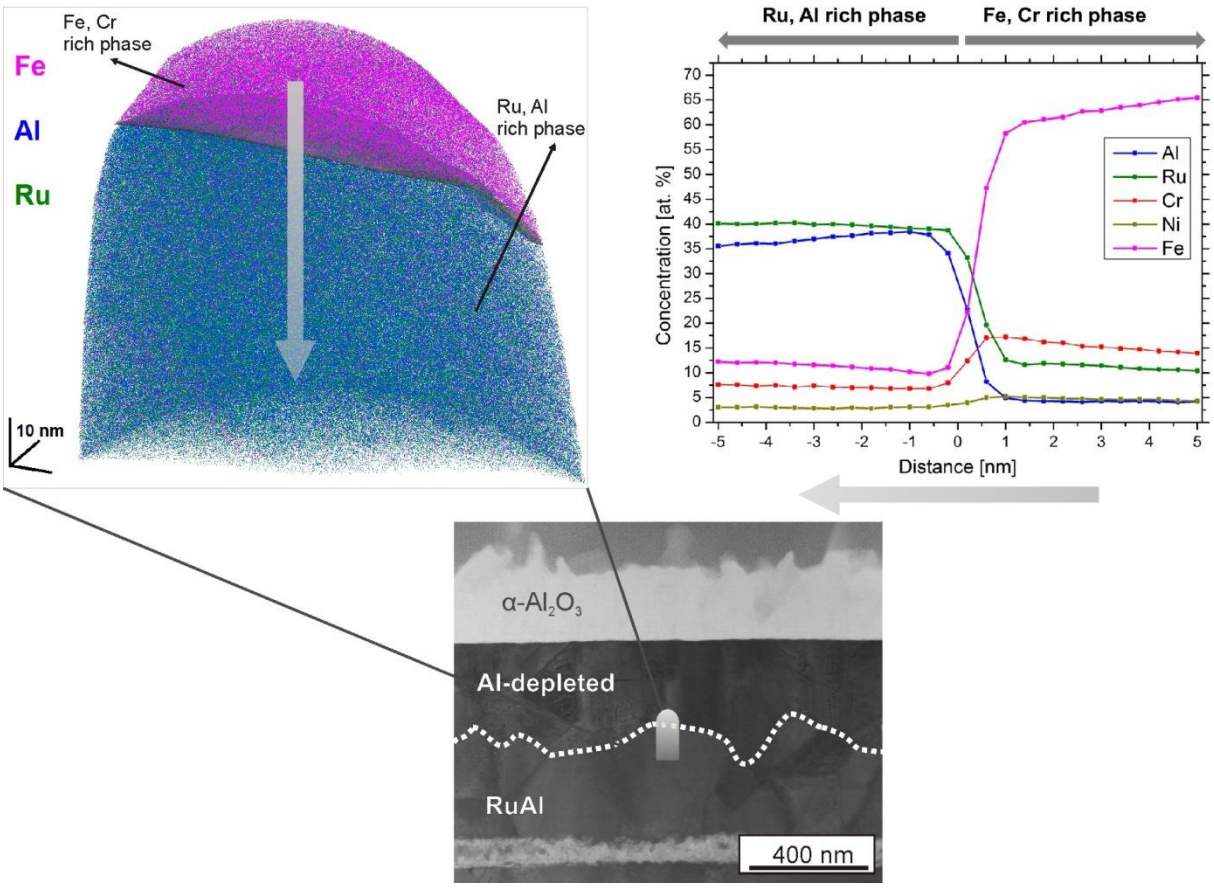

Figure 6.14: Chemical analysis at the Al-depleted and RuAl regions of a sample oxidised for 60 min at 900 °C. The area analysed is indicated in the STEM image. The 1D profile of atomic concentration indicates the distribution of each element.

It is known that the Ru phase is able to incorporate more than 60 at.% Fe or 35 at.% Cr as solid solution [157]. However, because of the high content of Fe and Cr detected in the Al-depleted zone, it might change the hcp structure of δ-Ru to one of the Fe-Cr alloys. A single bcc or a bi-phase (hcp+bcc) structure was expected according to the Cr-Ru and Fe-Ru alloy phase diagrams [157]. TEM analysis (Figure 6.15 and Figure 6.16) confirmed the hexagonal structure of the Al-depleted zone. This result agreed with those from XRD (Figure 6.10). From the aforementioned evidence, it is clear that Ru is able to contain high levels of both Fe and Cr in form of solid solution, probably alternating its composition (i.e. adjusting the Fe and Cr concentration in order to maintain the hcp structure).

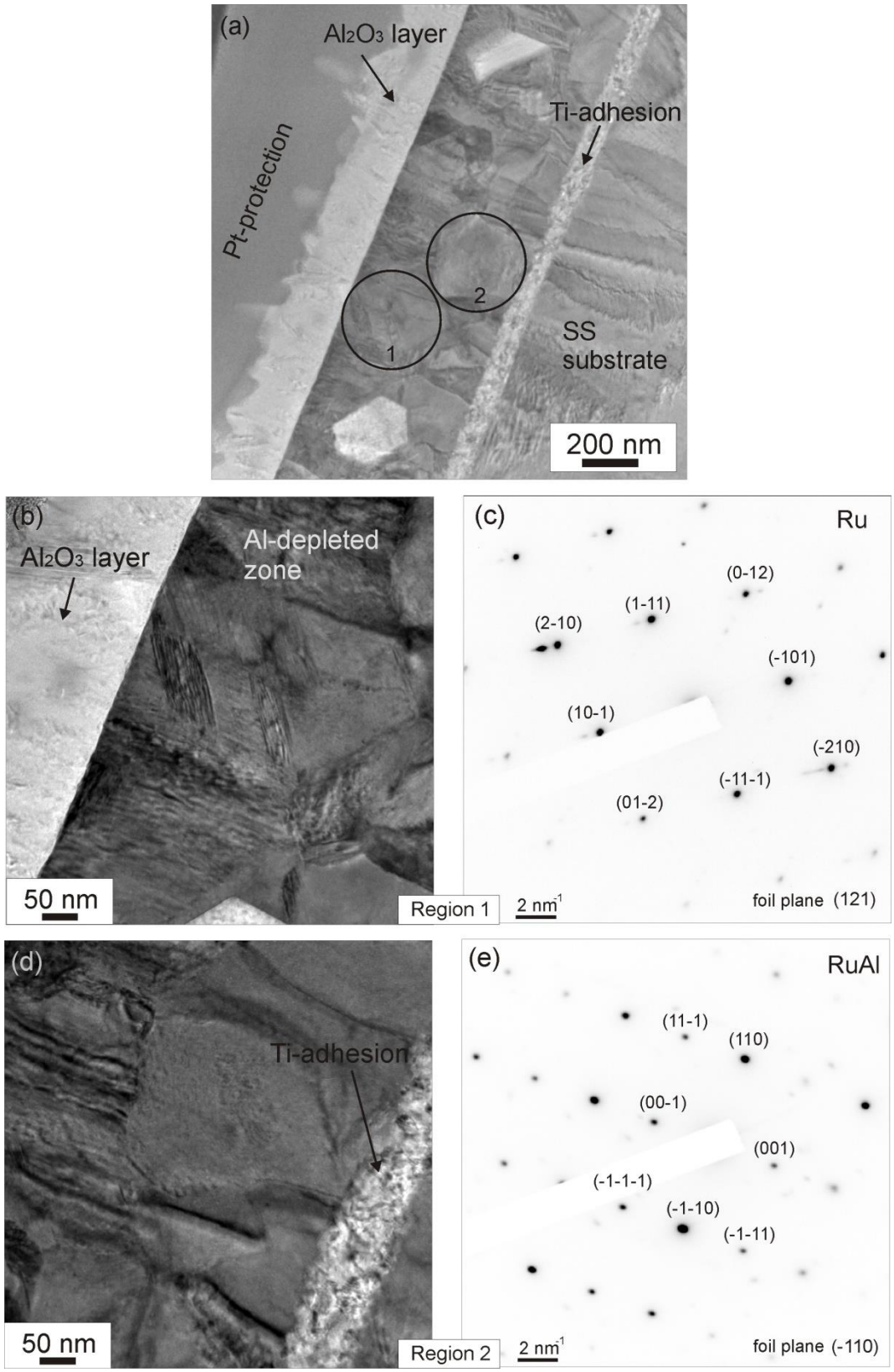

Figure 6.15: (a) TEM image of the sample oxidised at 900 °C for 60 min, showing two regions in the film: the Al-depleted (1) and RuAl (2) zones; (b) and (c) show the Al-depleted zone and its corresponding SAD pattern, respectively; (d) and (e) display the remaining RuAl zone and its SAD pattern, respectively. The d-spacing used for indexing the Ru-hcp was about 4% smaller than the one corresponding to the JPCDS-Ru: 06-0633.

Some satellite spots accompanying the principal reflections are also observed in the SAD patterns (Figure 6.15c and Figure 6.16c), probably related to compositional modulations inside the crystal structure [158]. This has also been observed in ternary and quaternary phases containing mostly In-Ga-X (X = As, N, P, etc) [159,160]. Additionally, fringes and diffused streaks were observed near and across the Bragg reflections in the TEM image and SAD pattern, respectively (Figure 6.15c and Figure 6.16). These could be associated to stacking faults, which are indicated by the arrows in Figure 6.16b and d.

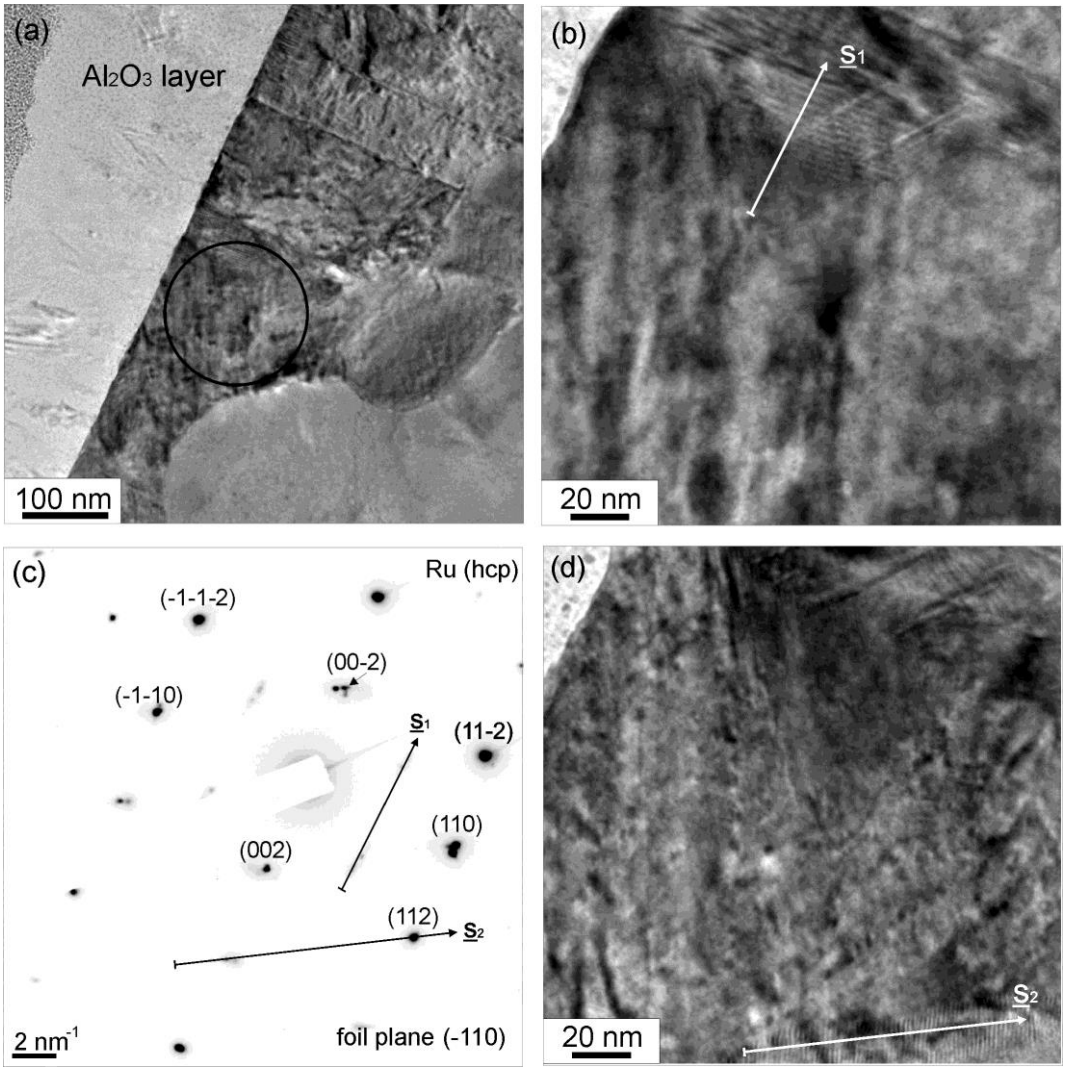

Figure 6.16: TEM images of the sample oxidised at 900 °C for 60 min, showing the Al-depleted zone (a, b and d); and SAD pattern indicating a hexagonal phase (c).

In the remaining RuAl layer (position 2 in Figure 6.11), neither phase transformations nor precipitates appeared, as derived from TEM (Figure 6.15) and XRD (Figure 6.10) analysis. The impurities were then located as substitutional atoms (see also section 5.4), resulting in RuAl(Fe) and RuAl(Cr) [93]. These remained segregated at GBs, as confirmed by APT measurements (Figure 6.17). Fe and Cr content increased, while that of Al and Ru decreased at GBs. This points out that

GBs were the main diffusion path for impurity transport. For this reason, Fe and Cr might affect the transport of Al to the metal/oxide interface but not through the Al_2O_3 layer.

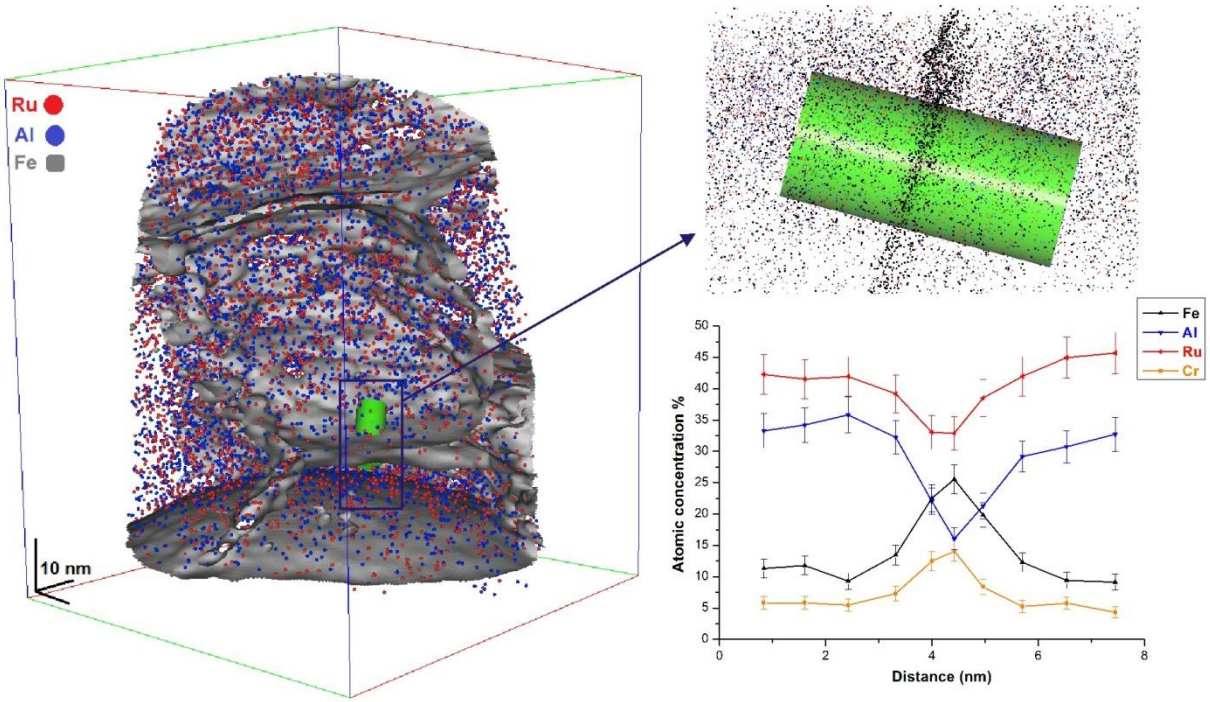

Figure 6.17: Chemical analysis of the RuAl region of an oxidized sample showing the increment of Fe and Cr at GBs. The iso-surface shows Fe content with a composition of 16.5 at.%.

6.4.2. Microstructural analysis of the oxidised RuAl films deposited onto Al_2O_3 substrates

Alumina substrates were employed in order to evaluate the oxidation behaviour of RuAl films in absence of impurities. RuAl films possessing two non-stoichiometric compositions were evaluated: Ru-rich ($RuAl_{(Ru\text{-}rich)}/Al_2O_3$) and Al-rich ($RuAl_{(Al\text{-}rich)}/Al_2O_3$), as shown in Table 6.1.

The samples oxidised for 50 min (Figure 6.18) showed a regular and compact oxide layer at their surface. The Al-depleted zone was identified as δ-Ru and resulted from the outward diffusion of Al, which reacted with oxygen to form the protective α-Al_2O_3 scale. The same morphology has already been observed in the RuAl/SS samples (Figure 6.11).

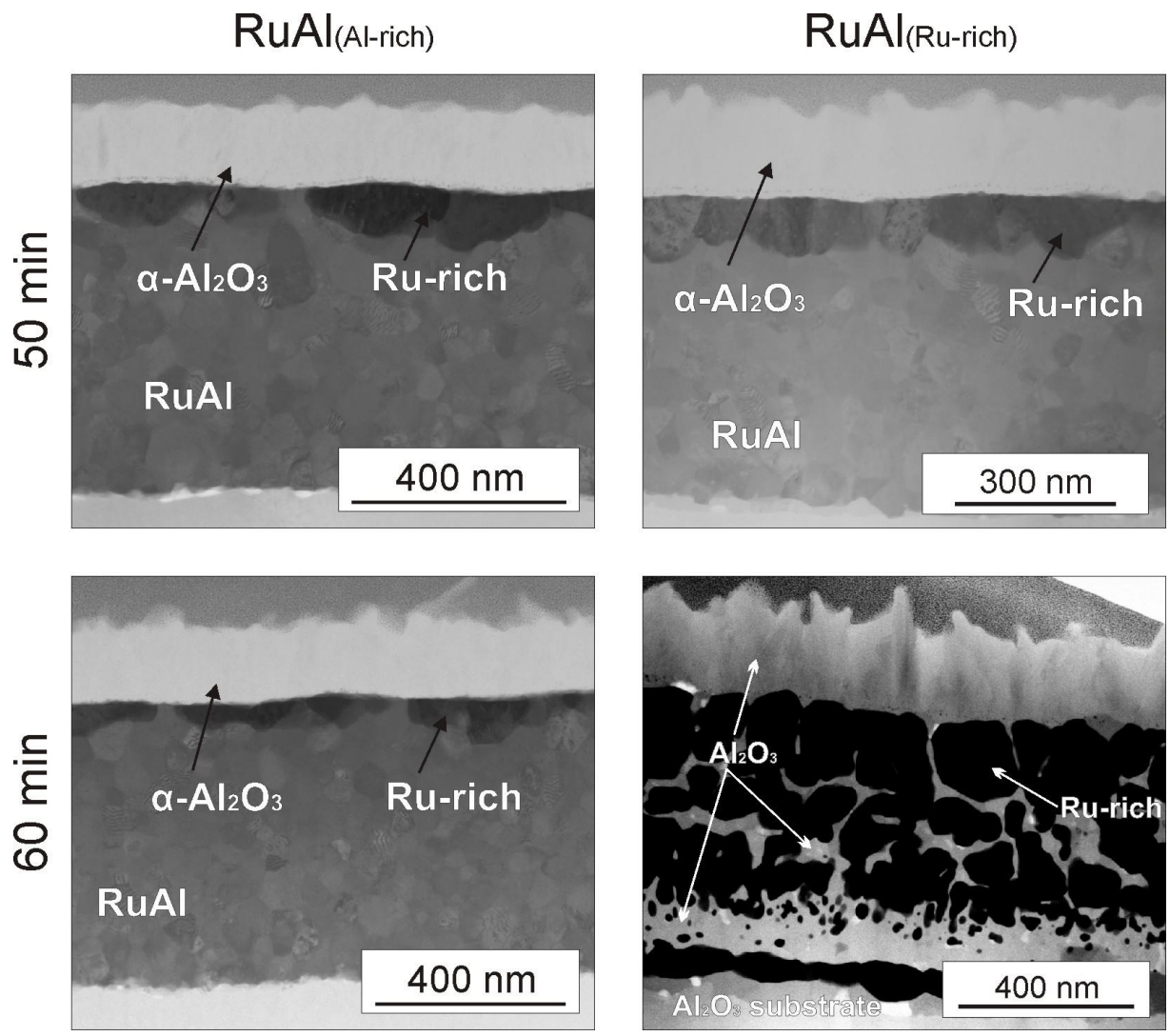

Figure 6.18: BF-STEM images[24] of the RuAl/Al_2O_3 samples with Ru-rich and Al-rich compositions oxidised at 900 °C for 50 and 60 min. $RuAl_{(Ru\text{-}rich)}$ film oxidised for 60 min presents a mixed microstructure composed of Al_2O_3 (bright areas) and Ru-rich (dark areas) phases.

The $RuAl_{(Ru\text{-}rich)}/Al_2O_3$ sample oxidised for 60 min showed a completely different microstructure than $RuAl_{(Al\text{-}rich)}/Al_2O_3$ and RuAl/SS oxidised for the same time. It presented an α-Al_2O_3 scale at the surface, with the RuAl layer completely transformed into a mix of Al_2O_3 and Ru-rich layers, as shown in Figure 6.18. This kind of morphology was also observed in $RuAl_{(Al\text{-}rich)}/Al_2O_3$ when oxidising at 1000 °C for 20 minutes (not depicted here).

It is known that the new phase formed beneath the protective oxide scale influences its subsequent stability and adherence [141]. Stresses generated at the oxide/Al-depleted zone due to oxide growth and δ-Ru formation are expected to promote cracking in the δ-Ru, especially at the thin zones of the layer [130,161]. On the other hand, if the transport of Al to the metal/scale interface is

24) Published: **M.A. Guitar**, E. Ramos-Moore, F. Mücklich, Journal of Alloys and Compounds (2014) DOI: 10.1016/j.jallcom.2014.01.137

slower than the inward diffusion of O through the oxide layer, the Al_2O_3 layer cannot continue to grow and the oxygen penetrates the oxide layer through rapid diffusion paths (e.g. grain boundaries, pores, cracks, etc.). At sufficiently high temperatures (T > 1300 °C), volatile Ru oxides are formed, leaving a porous interface-structure [162]. The contact of the oxygen with the single-phase RuAl region allows the formation of a new Al_2O_3 layer. Simultaneously, another Al-depleted zone is created, giving rise to a banded-layer morphology. In the $RuAl_{(Ru\text{-}rich)}/Al_2O_3$ samples, since GBs are paths for O and Al diffusion, the Al_2O_3 grows at these points, as shown in Figure 6.18. The mechanisms that produce the discontinuous formation of the Al_2O_3 layer, as observed in the $RuAl/Al_2O_3$ sample oxidised for 60 min, are not completely clear, but might include repeated cracking and healing of the oxide scale during the oxidation process. Cracks and pores in the Al_2O_3 and δ-Ru layer act as diffusion paths for oxygen to reach new RuAl material. The oxygen-aluminium reaction results in the growth of an Al_2O_3 layer and a corresponding Al-depleted zone, giving origin to a multilayer morphology, as observed by Bellina *et al.* [130] in bulk RuAl and by Chou in IrAl [129].

The long-term oxidation behaviour of a high-temperature alloy is determined not only by the effectiveness of the oxide scale as a reactant-transport barrier, but also by its resistance to mechanical failure. The protective Al_2O_3 scale formed at high temperature is an effective transport barrier for oxygen, but is also susceptible to cracks and spalls during thermal cycling or when cooling from working conditions down to room temperature. The addition of small amounts of reactive elements reduces mechanical failure in thermally grown oxides [134,163], but the mechanisms behind this are still unclear.

6.4.3. Stress analysis

Residual stresses in the RuAl film (on SS and Al_2O_3 substrates) annealed at 600 °C for one hour (initial condition for oxidation) were measured using the $\sin^2\psi$ plot method and compared to the calculated values using Equation 6.12, in order to quantify the effect of thermal stress due to CTE mismatch.

$$\sigma_{th} = -\frac{\varepsilon_{th}\, E_f}{(1-\upsilon)} = -\frac{E_f \int_{T_0}^{T} [\alpha_f - \alpha_s]\, dT}{(1-\upsilon)} \cong -\frac{E_f\, (\Delta\alpha)\, (\Delta T)}{(1-\upsilon)} \qquad (6.12)$$

In Equation 6.12, ΔT is the temperature difference between treatment and room conditions, Δα is the difference in linear CTE between substrate and film, E_f is the elastic modulus and υ is the Poisson's coefficient of the film. The E (276 GPa) and υ (0.286)values used for the stress calculation were those obtained for bulk RuAl [2]. The effects of texture and chemical composition were not considered for this calculation. Values for the CTE can be found in the Annexe. Thermal stresses estimated using the CTE-mismatch equation (Equation 6.12) reached values of -1.9 GPa and 0.2 GPa

for the RuAl/SS and RuAl/Al_2O_3 samples, respectively. Furthermore, residual stresses in RuAl films were determined using the multiple-{hkl} $\sin^2\psi$ stress analysis from GI-XRD measurements [72], with the help of the PANalytical X'Pert Stress Plus software v.2.1. Results found compressive stress in RuAl/SS (-1.61 ± 0.04 GPa), yet tensile stress in RuAl/Al_2O_3 (0.51 ± 0.08 GPa). Both experimental and theoretical values agree within 30% accuracy. The thermal stresses in the RuAl films were generated during cooling after deposition, while intrinsic growth stresses were developed during the formation of the single-phase RuAl.

As discussed in the previous section, α-Al_2O_3 is susceptible to cracking and spalling due to stresses generated during oxide growth or temperature changes, given the CTE mismatch between alloy and oxide. Several mechanisms have been proposed to explain the origin of growth stresses [164]. Some models indicate that oxide growth is produced by simultaneous diffusion of Al (outward) and O (inward) and thus, stresses in the oxide scale would be a consequence of the formation of new oxides along GBs lying perpendicular to the interface [161]. The stress generated in the α-Al_2O_3 phase was determined by measuring the strain (ε_ψ) in the crystal lattice for different directions (ψ) perpendicular to the interplanar spacing (d_ψ) of the selected {*hkl*} planes using Equation 6.13, where S_1 and $½S_2$ are the X-ray elastic constants [71]. In the $\sin^2\psi$ method the stress σ is calculated from the slope of the d_ψ vs $\sin^2\psi$ plot; S_1 and $½S_2$ from the C_{ij} constants [165] for α-Al_2O_3 using the Reuss approximation [69].

$$\varepsilon_\psi = \frac{d_\psi - d_0}{d_0} = \left(\frac{1}{2}S_2^{hkl} sin^2\psi + 2S_1^{hkl}\right)\sigma \qquad (6.13)$$

The $\sin^2\psi$ method was performed using the reflections {214} and {300} of α-Al_2O_3 to measure residual stresses in the oxide scale of RuAl/Al_2O_3. For RuAl/SS, the {202} and {211} were used due to peak convolution of the phase formed at the Al-depleted zone. Since the same XRD measurement time and optical parameters were used to measure RuAl/Al_2O_3 samples before and after oxidation, the increase in the peak intensities of reflections {214} and {300} was due to the presence of the α-Al_2O_3 scale at the surface of the sample.

The average strains of the RuAl/Al_2O_3 (unoxidised and oxidised), and RuAl/SS (oxidised) samples are shown in Figure 6.19. Since the strain in the Al_2O_3 substrate was found to be within the measurement error, it can thus be neglected, and does not affect the values obtained from the oxidized samples. On the other hand, the oxide scale on the RuAl/Al_2O_3 sample showed tensile stress (51.1 ± 10.5 MPa), whereas the one on the RuAl/SS surface presented compressive stress (-1277 ± 107 MPa).

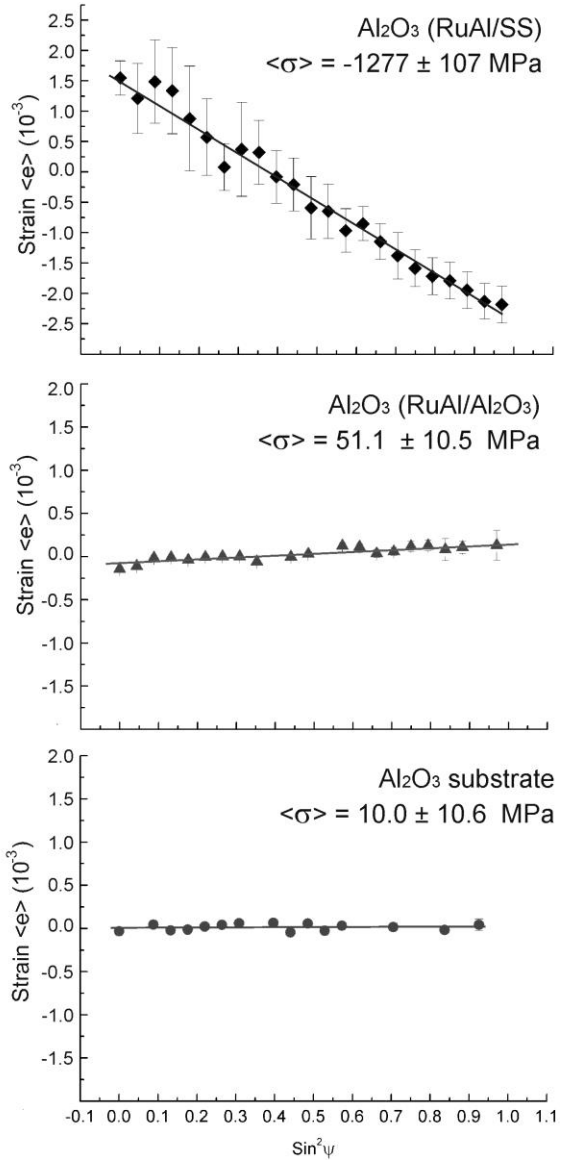

Figure 6.19: $Sin^2\psi$ plots[25] from α-Al_2O_3 using the {214} and {300} reflections. The curves show the average weighted by the multiplicity factor of each reflection [166]. For the unoxidised sample, the strain was measured in the substrate.

Stresses generated during oxidation can be relaxed by several mechanisms, like cracking or plastic deformation, among others[95,164]. Oxide cracking occurs when tensile stresses appear [95], having severe consequences for the material stability because of the exposure of fresh material to the oxidising atmosphere. Additionally, if the elastic-strain energy stored in the scale exceeds the fracture resistance of the interface, spallation of the compressively stressed oxide might occur [95]. However, if the metal beneath the scale can plastically deform, the stresses can be relaxed by simultaneous deformation of the scale and alloy. The new alloy formed in the RuAl/SS samples at the Al-depleted zone (containing high quantities of Fe and Cr) might be more ductile than δ-Ru,

25) Published: **M.A. Guitar**, E. Ramos-Moore, F. Mücklich, Journal of Alloys and Compounds (2014) DOI: 10.1016/j.jallcom.2014.01.137

thus avoiding damage to the scale. Alloys and compounds containing Fe, Cr and Ru are not available in the literature. Therefore, there are no reference values for mechanical and thermal properties to compare with. However, microstructural analysis of oxidised RuAl/Al_2O_3 samples has shown no cracking or spallation (Figure 6.18). Furthermore, the diverse analyses did not present evidence of stress relaxation and thus, it is not possible to evaluate the effect of the Fe-Cr-Ru alloy on the preservation of the microstructure. For this reason, further studies are needed in order to characterise this phase and understand its influence on the stability of the protective Al_2O_3 scale, with the aim of tailoring the thermal and mechanical properties of the layer.

6.4.4. Oxidation kinetics

The growth kinetics of the oxide layer have been studied by measuring the thicknesses of the α-Al_2O_3 scale, at several oxidation times, using STEM images. Figure 6.20 shows the scale thickness as a function of time of $RuAl_{(Ru\text{-}rich)}/Al_2O_3$, $RuAl_{(Al\text{-}rich)}/Al_2O_3$ and RuAl/SS oxidised at 900 °C; and RuAl/SS oxidised at 750 °C. The data corresponding to RuAl/Al_2O_3 oxidised for 60 min was not included in the oxidation rate calculation, due to the complex microstructure (Figure 6.18), from which the oxide thickness was not clear. The oxide thickness (x) as a function of time (t) was fitted using Equation 6.14 [95], whose adjusted parameters k_x and C are resumed in Table 6.3.

$$x = k_x\, t + C \qquad (6.14)$$

Table 6.3: Linear fitting parameters obtained from the oxide scale thickness data as a function of time (Figure 6.20)

Sample - Temperature	linear growth	
	k_x (10^{-3}) (nm/s)	C (nm)
RuAl/SS – 750 °C	4.6 ± 0.1	9.3 ± 0. 4
RuAl/SS – 900 °C	57.9± 5.5	8.8 ± 4.9
$RuAl_{(Ru\text{-}rich)}/Al_2O_3$ – 900 °C	46.9 ± 2.8	21.9 ± 3.8
$RuAl_{(Al\text{-}rich)}/Al_2O_3$ – 900 °C	41.6 ± 6.4	20.1 ± 11.0

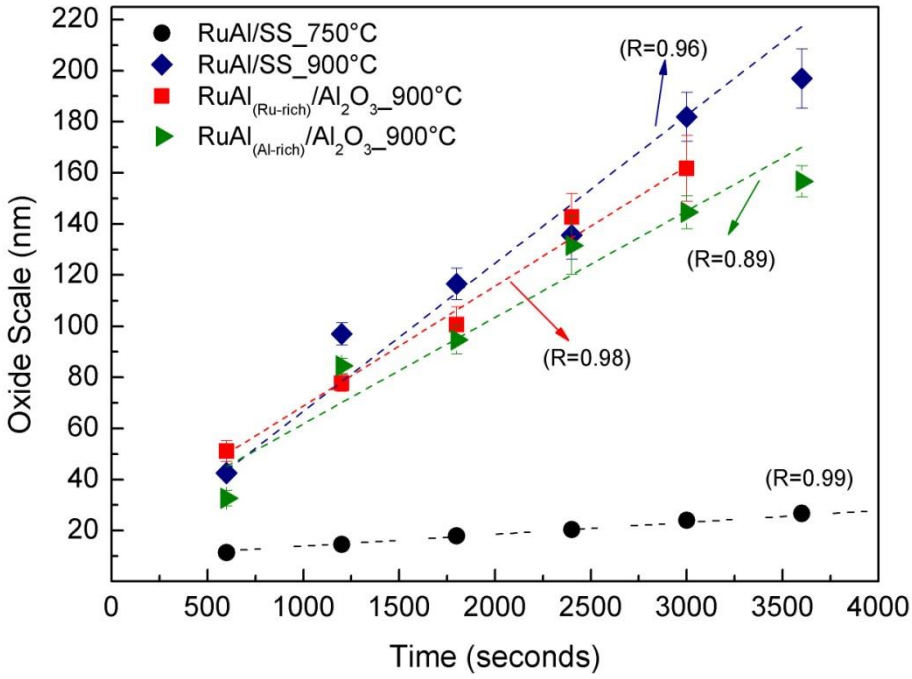

Figure 6.20. Oxide scale thickness as a function of time for RuAl/SS samples oxidised at 750 °C and RuAl/SS and RuAl/Al_2O_3 at 900 °C[26]. A linear fit was performed on all samples, whose adjusted parameters are listed in Table 6.3.

The linear growth behaviour has been observed at the beginning of the scale formation for thicknesses on the order of 100 nm [167,168], which matches the current scale measurements. Based on the theory of the scale kinetics [95,169], at this stage, there is no thermal equilibrium between the metal/oxide and oxide/gas interfaces. Therefore, phase-boundary process is the rate-determining steps of the reaction, instead of ion diffusion through the scale as in the case of the parabolic rate law.

A different analysis from the same results can be found elsewhere [170]. Parabolic and linear oxidation behaviours can be confused at the first oxidation stages. For this reason, further analyses were necessary to arrive at a conclusion for the oxidation behaviour. Figure 6.21 shows the linear and parabolic fit for the RuAl/SS samples oxidised at 750 and 900 °C. The oxide thickness fits a linear behaviour when oxidising for 5 hours at 750 °C (90 ± 4 nm), whereas for 105 minutes at 900 °C (260 ± 20 nm) it fits a parabolic law. These observations suggest that for very thin Al_2O_3 films (< 200 nm), the activity of the metal at the surface remained high. Therefore, the reaction was likely to be controlled by phase-boundary processes, as discussed in the aforementioned paragraph. As the reaction proceeded, the oxide layer thickened and the activity at the surface decreased, giving rise to a diffusion-controlled process following a parabolic law [95].

26) Published: **M.A. Guitar**, E. Ramos-Moore, F. Mücklich, Journal of Alloys and Compounds (2014) DOI: 10.1016/j.jallcom.2014.01.137and **M.A. Guitar**, F. Mücklich, Oxidation of Metals 80 (2013).

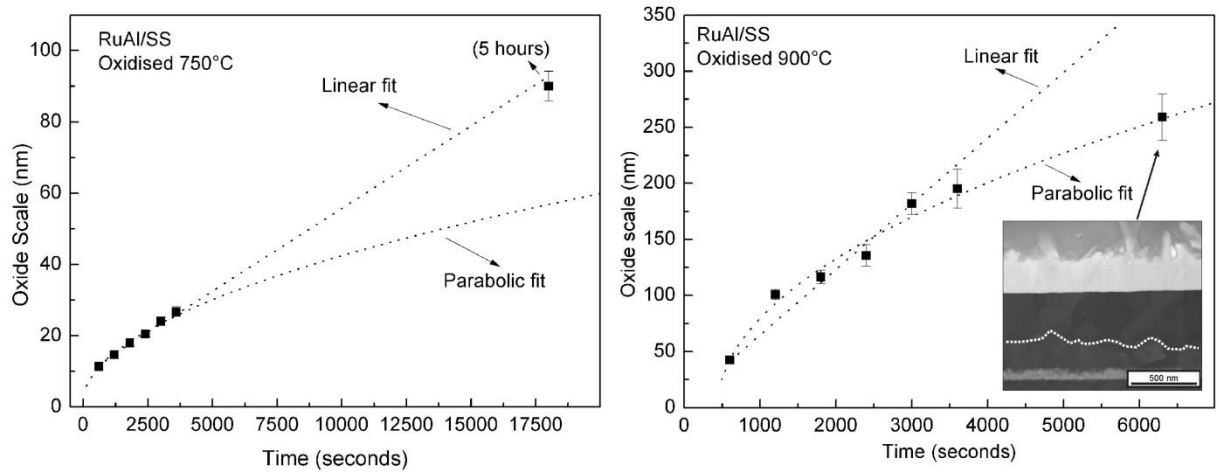

Figure 6.21: Linear versus parabolic fit for the RuAl/SS oxidised at 750 and 900 °C. The inset shows the microstructure of the samples oxidised at 900 °C for 6500 seconds, with remaining RuAl film.

By comparing the parameters in Table 6.3, it is shown that a slightly higher oxidation rate can be observed in the RuAl/SS samples (i.e. with elements coming from the SS substrate), which is in accordance with the oxidation behaviour of aluminides in the presence of reactive elements [153,154]. The parameter C represents the initial scale thickness, which corresponds to the oxide layer after annealing at 600 °C, before the oxidation experiment. Different oxidation behaviours (oxidation kinetics or oxidation rate) cannot be excluded for times less than 10 minutes.

The activation energy for oxidation (Q) was estimated by measuring the growth rate of the oxide scale ($G = \Delta x/\Delta t$) at different temperatures. It was determined from the slope of the curve $log\ G$ versus $1/T$ (Figure 6.22), based on the Arrhenius model shown in Equation 6.15 [24]. The term G_0 is a constant, R is the universal gas constant and T is the absolute temperature.

$$G = G_0 \exp\left(\frac{-Q}{RT}\right) \qquad \text{or} \qquad \ln(G) = \ln(G_0) + \left(\frac{-Q}{RT}\right) \qquad (6.15)$$

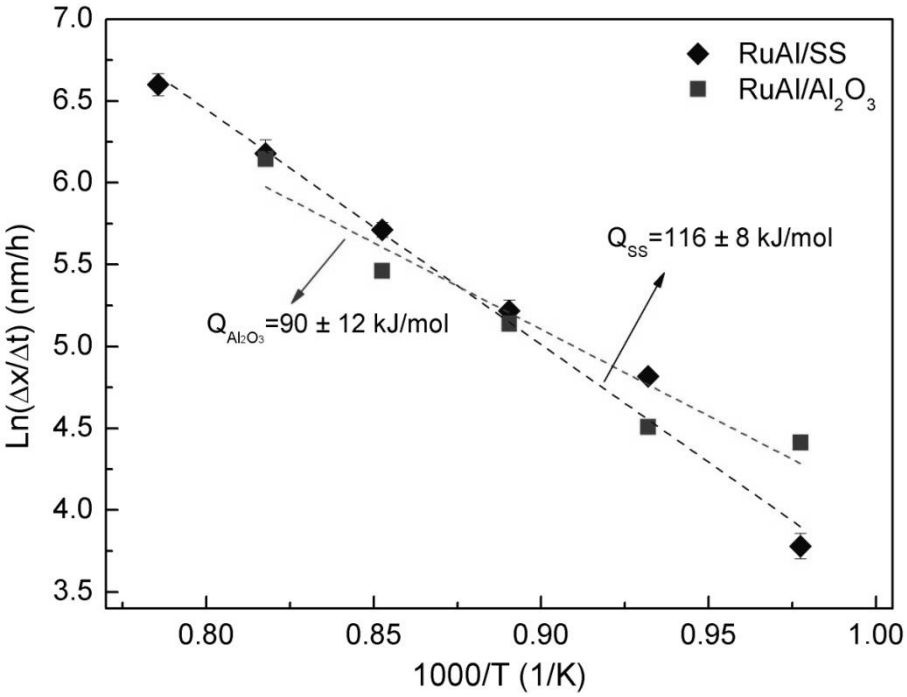

Figure 6.22. Arrhenius plot[27] of the α-Al_2O_3 formation on RuAl thin films (Ru-rich) deposited onto SS and Al_2O_3 substrates, for the temperature ranges 750 °C-1000 °C and 750 °C-950 °C, respectively.

The activation energy of α-Al_2O_3 on RuAl/SS (with Cr and Fe impurities) was 116 ± 8 kJ/mol, whereas on RuAl/Al_2O_3 (impurity-free) it was 90 ± 12 kJ/mol. This value for RuAl/SS was approximately 30% larger than on RuAl/Al_2O_3 (fit error of 7%), indicating that the presence of impurities influenced the kinetic behaviour. Other factor affecting the oxidation kinetics might be the difference in grain size existing between $RuAl_{(Ru\text{-}rich)}$/SS and $RuAl_{(Ru\text{-}rich)}/Al_2O_3$ (Figure 6.11 and Figure 6.18). This also affects the Al supply at the metal/oxide interface [171,172], thus influencing the oxidation kinetics. The activation energy for RuAl (bulk or thin films) oxidation is absent in the literature. However, the obtained values correlated well with the ones observed by Pettit and Wagner [167] for iron oxidation (92 kJ/mol) in the same temperature range and in absence of impurities. Variations in the activation energy and oxidation rates have been observed for other intermetallic compounds as a result of the reactive elements (RE) and impurities, mainly due to the agglomeration of foreign atoms at GBs [44,134,146,154,173]. Particularly, Zhong *et al*. [23] observed a decrease in the activation energy by adding AlN into NiAl films. Other effects to be expected from reactive impurities are changes in the oxide growth mechanism, reduction of the oxidation rate and modification of the scale microstructure [154,163]. Furthermore, one of the biggest advantages of the presence of impurities and RE is the improvement of the scale adhesion and resistance to spallation [134,146,154]. Therefore, the results presented here pointed to the fact that Cr and Fe impurities from the SS substrate modified the kinetics of α-Al_2O_3 formation, acting as

27) Published: **M.A. Guitar**, E. Ramos-Moore, F. Mücklich, Journal of Alloys and Compounds (2014) DOI: 10.1016/j.jallcom.2014.01.137and **M.A. Guitar**, F. Mücklich, Oxidation of Metals 80 (2013).

energy barriers for atom diffusion in the alloy, by concentrating at the RuAl GBs (see APT Figure 6.17). On the other hand, the diffusion of atoms inside the film is modified in presence of compressive stresses and, consequently, so is the oxidation kinetics.

6.4.5. Effect of diffusion barriers in the incorporation of elements from the SS-substrate into the RuAl films

As detailed in the previous sections of this chapter, oxidation at elevated temperatures promoted the diffusion of elements (mainly Fe and Cr) from the SS substrate into the RuAl thin films. The properties of the intermetallic film could be affected by the presence of these elements [9,133,155].

It was previously observed that Fe and Cr remained in the RuAl film as a solid solution or concentrated at GBs. They did not form compounds either with RuAl or with Ru in the Al-depleted zone, as shown in the TEM and APT analysis in section 6.4.1. Fe and Cr came into contact with the oxidising atmosphere after diffusing along macroscopic film defects, as those shown in Figure 6.23a and d. Complex Fe-Al-Cr oxides were formed with high volume change at defect boundaries, damaging the RuAl film (Figure 6.23b). The growing foreign oxides might also have caused the detachment of part of the RuAl film, promoting the formation of non-protective oxides (Figure 6.23c). The defects grown during Ru-Al deposition were non-uniformly distributed over the film surface. Their growth was induced by substrate irregularities or foreign particles (such as dust, polishing residues, etc.) and their size and density depended on the deposition conditions. A classification of different types of defects can be found elsewhere [174]. The defect shown in Figure 6.23a) and d) is known as a *flake defect*. It is a loosely-bound defect and large in size (5-40 μm).

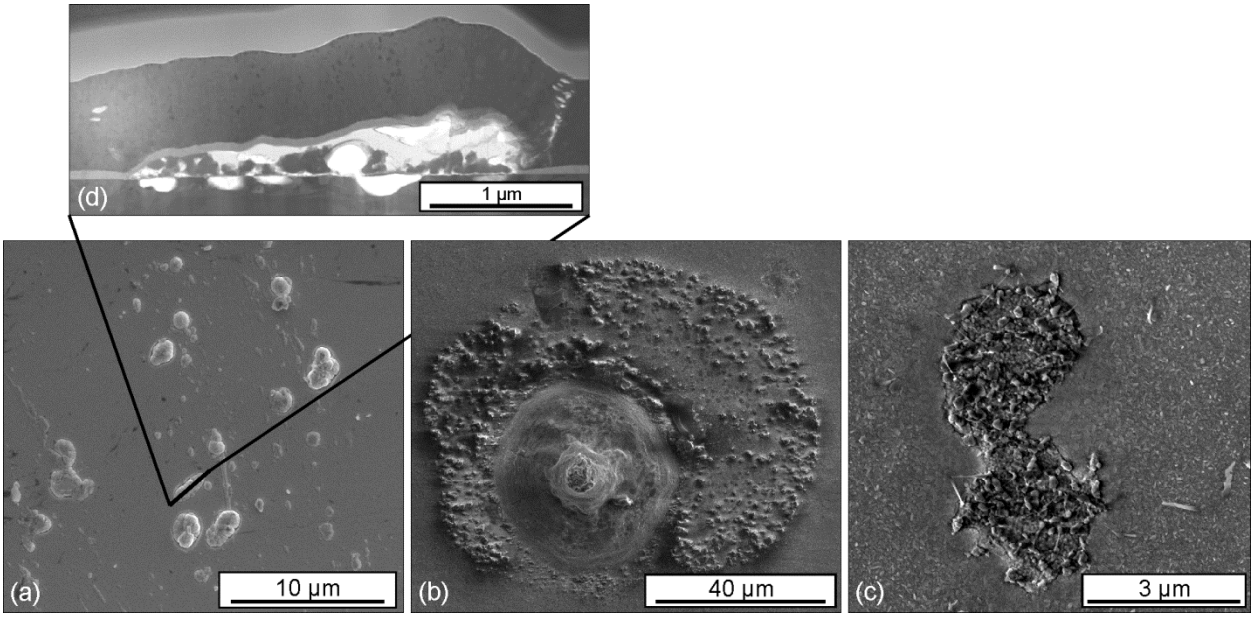

Figure 6.23: Defects in RuAl films grown during deposition. Surface and cross-section view of the show unoxidised samples (a) and (d), respectively; defects after oxidation (b) and (c).

The deposition of diffusion barriers (DB) between the substrate and the RuAl film is a convenient method to inhibit the diffusion of contaminants from the metallic substrate, thus preventing the alteration of the film properties. Al_2O_3 has been found to avoid the diffusion of Fe into Cu(In,Ga)Se_2 thin film solar cells [175], whereas tungsten (W) reduces the diffusion of Cr between Ni-based eutectic alloys and NiCrAl coatings [176].

DBs composed of Al_2O_3 and W were deposited prior to the Ru-Al deposition, using the parameters listed in Table 6.4. Two configurations of DBs were used, listed in Table 6.5.

Table 6.4. Deposition parameters for the Al_2O_3 and W diffusion barriers.

Sputtering targets	**Al_2O_3**	**W**
Current type	RF	DC
Power density	2.0 W/cm^2	0.62 W/cm^2
Deposition rate	~10 nm/min	~20 nm/min
Base pressure	10^{-7} mbar	
Ar flow	60 sccm	
Sputtering pressure	3 x 10^{-3} mbar	
Target to substrate distance	65 mm	

Table 6.5. Diffusion barrier configuration. Al_2O_3 was the first deposited layer in DB-1 and W in the case of DB-2.

	Configuration
DB-1	Al_2O_3 (130 nm) + W (200 nm)
DB-2	W (200 nm) + Al_2O_3 (130 nm)

Oxidation tests were performed at 750 °C and 900 °C for 45 min, under the same conditions detailed in section 6.3. Film composition was analysed by EDX in STEM foils. Oxidising at 900 °C, the concentration of Fe decreased from ~12 at.% (without DB) to ~3 at.%; and Cr from ~7 at.% (without DB) to ~2 at.%. At 750 °C the concentration decreased from ~6 at.% for Fe to ~2 at.%; and from ~2 at.% to ~1 at.% for Cr (Table 6.6).

Table 6.6: Impurity content in RuAl layers with and without DBs.

	750 °C/45 min		**900 °C/45 min**	
	Fe	**Cr**	**Fe**	**Cr**
No DB	~6 at.%	~2 at.%	~12 at.%	~7 at.%
DB-1	~2 at.%	~1 at.%	Not measured – complete layer detachment	
DB-2	~2 at.%	~1 at.%	~3 at.%	~2 at.%

Diffusion of Fe and Cr into RuAl films has been reduced with the presence of DBs, but only partially. Even when a bulk material meets the requirements for diffusion barriers, the presence of GBs and other structural defects in film form, could be counterproductive [142]. However, such barriers usually fail because of extended structural defects in the metal film acting as fast diffusion paths [142].

DBs combining Al_2O_3 and W have reduced Fe and Cr diffusion from the substrate about 70%. However, the adhesion of these layers, both to the substrate and the film, was weak, as evidenced by their detachment during oxidation (Figure 6.24). This weak adherence of the coatings is critical. Growth stresses in DB elements could be reduced by varying the deposition parameters and the final thickness. Moreover, the adherence could be improved by adding an extra adhesion layer between the substrate and DB. Further investigations are needed in order to improve the adhesion of the complete multilayer system.

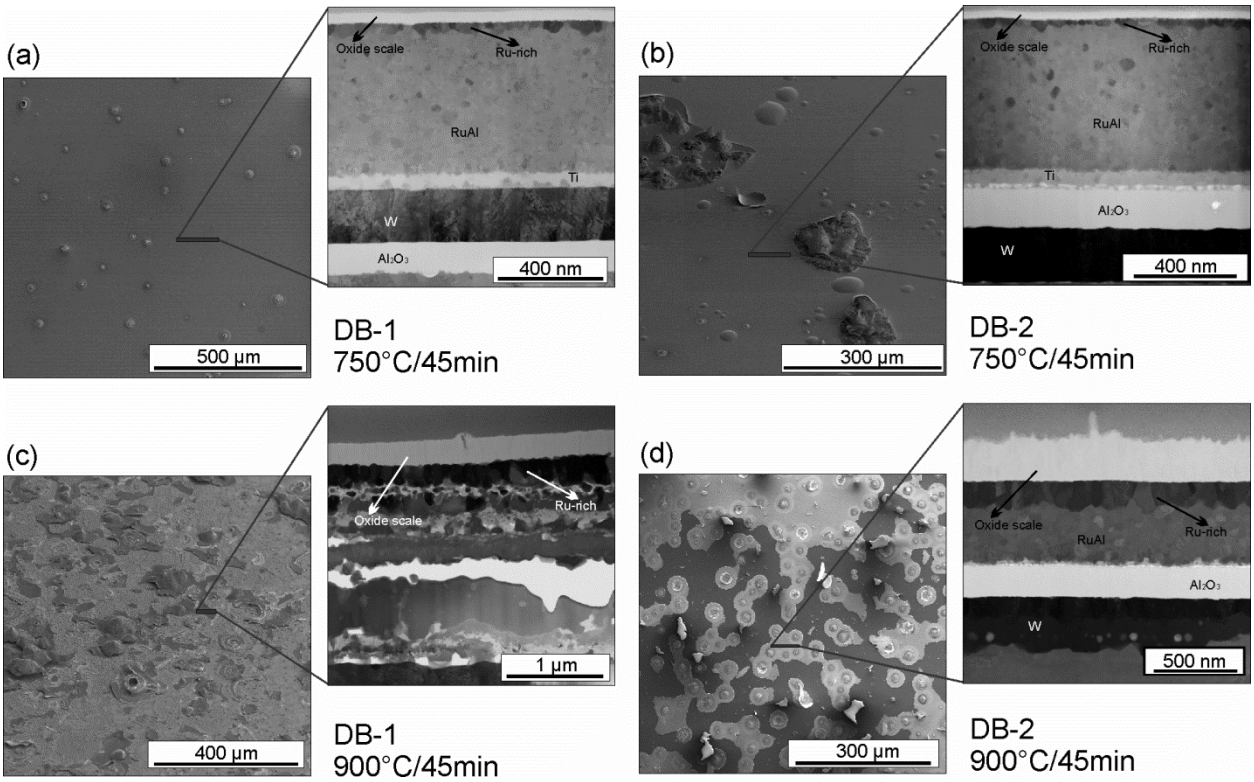

Figure 6.24: SEM and STEM images of samples possessing a DB, after oxidation for 45 min at 750 °C and 900 °C.

6.5. Summary and Outlook

The isothermal-oxidation behaviour of RuAl thin films deposited onto SS and Al_2O_3 substrates was analysed in the present work, at 750 °C and at 900 °C in atmospheric air. Since impurities (Fe and Cr) diffuse only from the SS substrate, their influence on the formation of the protective aluminium oxides was evaluated in comparison with the films grown on Al_2O_3.

The high density of grain boundaries in NC RuAl/SS allowed the rapid outward diffusion of Al through short paths, promoting the formation of the protective α-Al_2O_3 for all temperatures and times used in this work. α-Al_2O_3 was the only oxide detected on RuAl films. It grew linearly in time, controlled by phase-boundary processes. The linear growth-rate was highly temperature dependent, as observed for the RuAl/SS samples oxidised at 750 and 900 °C. The thickening of the oxide scale gave rise to a diffusion controlled process, which followed a parabolic law. A thickness of about 200 nm was proposed here for the transition from the linear to the parabolic oxide growth. This work is the first to report linear kinetics in α-Al_2O_3 growth on intermetallic compounds. Studies on the growth of alumina are generally focused on the long-term stability of the oxide scale, disregarding the early stages of oxidation, when the scale is only a few nanometres thick. Furthermore, these analyses are performed at higher temperatures (>900 °C) and thus, the initial stages become almost imperceptible, displaying only the parabolic part of the reaction.

Despite that oxide growth was dominated by chemisorption processes, a net flux of Al diffusing outward to the surface distinguished the systems here studied. This has been demonstrated by the presence of Ru-rich particles at the oxide/metal interface, formed during the first oxidation stages, which showed that the surface was not displaced before and after oxidation. Furthermore, the outward diffusion of Al led to the creation of an Al-depleted zone beneath the oxide scale, resulting in a new δ-Ru phase, containing high quantities of Fe and Cr (in the case of SS substrates).

Internal oxidation with a multilayer morphology was not completely avoided in non-stoichiometric RuAl films with excess aluminium on Al_2O_3 substrates ($RuAl_{(Al\text{-}rich)}/Al_2O_3$). Said layers also presented this morphology after oxidation at higher temperature (1000 °C). Therefore, the excess of Al only retarded the formation of this type of microstructure. This was avoided using SS substrates. However, the mechanisms acting in this case are not completely clear. The presence of Fe and Cr might avoid this type of microstructure by stabilising the Al-depleted region through the formation of a ternary compound (Fe-Ru-Cr) with hcp structure. Since this compound has been unknown so far, more studies are needed to evaluate the mechanical and chemical stability of this region, in order to determine the reasons behind its good performance as an oxygen diffusion barrier. On the other hand, the excess of Ru from the RuAl phase can be eliminated by diffusing into the SS substrate and thus, avoiding the precipitation of new δ-Ru regions. However, this should be further studied in order to determine how eliminating Ru from the RuAl-phase affects the microstructure stability of the whole system. Similar results might be obtained using other metallic substrates, such as Ni superalloys. Tensile stresses were generated in the scale during oxidation in absence of impurities. On the contrary, compressive stresses were developed in the oxide after Fe and Cr diffused into the RuAl film, enhancing the material stability at high temperatures.

Kinetic and microstructural analysis showed that the oxidation behaviour of non-stoichimetric RuAl films was affected by the presence of Fe and Cr impurities and by the difference in grain size at the oxidation temperature. The activation energy for aluminium oxidation in RuAl/SS (116 ± 8 kJ/mol) was around 30% higher than in RuAl/Al_2O_3 (90 ± 12 kJ/mol). This indicated an influence of Fe (~62 at.%) and Cr (~20 at.%) on the RuAl oxidation, possibly by the generation of energy barriers at grain boundaries, due to the high concentration of these elements at this point.

Preliminary studies using a combination of Al_2O_3 and W layers as DBs have shown a decrease of more than 70% in the diffusion of Fe and Cr into the RuAl layer. However, the adherence of the coating was weak mainly due to stresses generated during their deposition. This could be improved by adding adhesion-interlayers or by varying the deposition parameters of each component.

7

Wetting of RuAl films by molten glass

In this chapter, the wettability of RuAl films deposited onto stainless steel (SS) by molten borosilicate glass at elevated temperatures (up to 1050 °C) is evaluated. Additionally, Contact angle measurements are performed by the sessile drop technique under air and Ar atmospheres. As an introduction to the present chapter, a theoretical overview on wetting is presented. Microstructural and chemical analyses of the glass/substrate interfaces are also provided in this chapter, followed by their discussion and corresponding conclusions.

The results exposed in the present chapter have been submitted to the peer reviewed journal Surfaces and Coatings Technology (M.A. Guitar, M. Eisenbart, U.E. Klotz, F. Mücklich; *High temperature wettability of RuAl films by molten borosilicate glass*)

7.1. Introduction

High precision optical elements with aspherical surfaces or other complex shapes are inevitably manufactured by glass moulding (GM). During precision GM, a glass gob is placed between two precision moulds, heated above the glass softening point, pressed to the desired final shape and, finally, cooled down to room temperature, as indicated in Figure 7.1 and Figure 7.2. The selection of the mould material strongly depends on the nature of the processed glass [55]. Moreover, each glass type possesses a specific softening point (T_g), which defines the process temperature and, consequently, the level of chemical reaction between glass and mould. For low-T_g glasses, moulding processes are usually performed at temperatures between 500 and 700 °C[28]. However, depending

28) Information obtained from Schott AG website: *http://www.schott.com/advanced_optics/german/products/optical-materials/optical-glass/low-tg-glass-for-precision-molding/index.html*

on the nature and chemical composition of the glass, the moulding temperature can reach up to 1000 °C [55]. Low-temperature processing helps to extend the operating lifetime of mould materials, by reducing their chemical interaction.

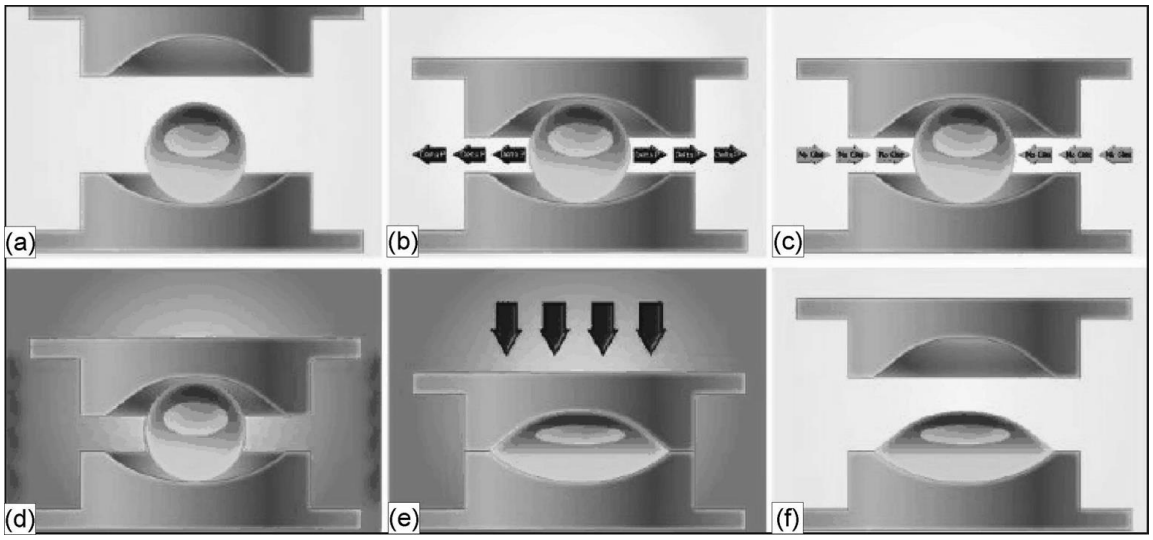

Figure 7.1: Precision glass-moulding process overview[29]**:** a) placing of the glass bead; b) air evacuation from the process chamber; c) flooding with inert gas; d) heating; e) lens moulding; and f) cooling. Depending on the fabrication process, the steps b) and c) might not be necessary.

During moulding, the die surface is exposed to the chemically active glass and to thermo-mechanical loads. This results in three critical problems: *wear*, *oxidation* and *sticking adhesion*, which must be overcome in order to preserve the quality of the final product, as previously mentioned in section 1.3.4. The use of protective coatings is an outstanding way to increase the lifetime of glass moulding dies (GMD) and the quality of glass products. Furthermore, since material selection is strongly influenced by the type of glass the mould and coating materials must be optimised for each particular case. Accordingly, the coating must be stable at high-temperatures, chemically inert to glass at processing temperature, sufficiently hard to avoid scratching and highly resistive against oxidation [55].

In several works [177–180], the analysis of the coating material was focused on its deposition parameters and mechanical properties, whereas no analysis of the coatings in contact with glass was performed. Other studies report the contact angle between coating and glass, but they do not provide any information regarding the glass/coating and coating/substrate interaction [59]. In glass moulding, non-wetting ($\theta > 90°$) between glass and mould is a basic requirement, in order to minimise the adhesion.

29) Image from: *http://images.pennnet.com/pnet/surveys/lfw/molded_fig3.jpg*

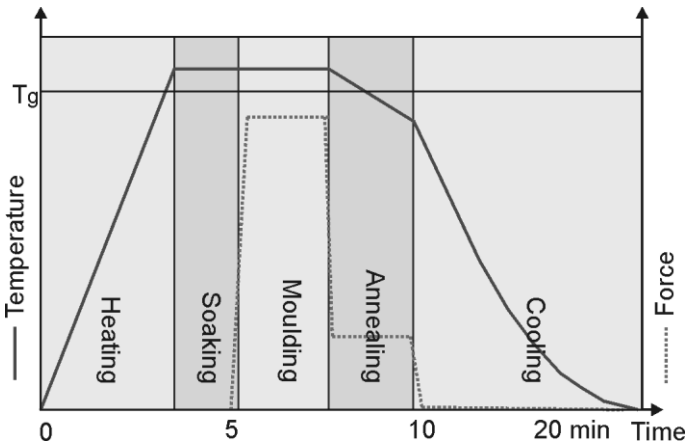

Figure 7.2: Precision glass-moulding process, where the temperature and applied force are indicated as a function of process time. Graphic based on [181].

Multi-component compounds, ceramics and metals have been tested as potential working layers for GMDs and some of them are currently being used for precision glass lenses. Recently, Cheng *et al*. studied CrAlSiN, TiAlSiN and AlTiN onto tungsten carbide (WC), due to their excellent tribological performance and high oxidation resistance at high temperature (800 °C). Wetting with molten low-Tg glasses (K-PG325[30]) showed that CrAlSiN coatings perform better (higher contact angle) than the others [182,183]. Other reports focused on diverse systems as protective coatings for GMDs, such as Ti-Al-N, Ni-Al-N, Ti-B-C-N and Ti-B-C [59,184,185]. The Ti-B-C compound displayed the most suitable non-sticking properties to molten glass of all the systems investigated, whereas Ti-B-C-N coatings showed a good response when operating at relatively low temperatures (up to 700 °C), in vacuum or in protective environments (N_2) [184]. WCrN showed better non-sticking response at low temperature (400 °C) than CrN [180]. However, at higher temperatures (500 °C), residues of K-PG325 glass remained on the WCrN coating surface.

On the other hand, noble metal-based coatings have also shown interesting properties and have been considered as suitable materials for GMDs [55]. Ir-Re films presenting two different compositions ($Ir_{0.77}Re_{0.23}$ and $Ir_{0.53}Re_{0.47}$) were microstucturally analysed after undergoing thermal fatigue (cycles between 270-600 °C) under 1%O_2-Ar atmosphere [186]. The $Ir_{0.77}Re_{0.23}$ alloy displayed better thermal stability and showed low surface roughness (~1nm) after 500 cycles. However, $Ir_{0.53}Re_{0.47}$ films developed cracks and pores on the surface after about 300 cycles, reducing their protection performance. The instability of this alloy was in part attributed to the formation of volatile oxides (Re_2O_7). Another system evaluated as a working layer for GMDs was Mo-Ru, due to the high melting point of both components [177,178]. The different compositions obtained by changing the deposition parameters were microstructuraly analysed, and their micro-hardness was measured, showing values between ~11 to ~13 GPa for $Mo_{11.6}Ru_{88.4}$ and $Mo_{46.3}Ru_{53.7}$, respectively.

30) Low-Tg glass produced by sumita-opt: *http://www.sumita-opt.co.jp/en/optical/optical04.htm*

Pure noble metals such as Ag, Au, Ir, Rh and Pt have been considered in the past as protective coatings for GMDs. However, during wetting analyses, Ag, Au and Pt showed strong adherence to lead-borosilicate glass. Tests with E-glass[31] showed the highest and lowest wetting for Pt and Rh, respectively [187,188]. Pt on M42 steel showed low contact angles at about 900 °C [56]. Additionally, Pt-Ir reacted with Fe from the M42 substrate, deteriorating the anti-sticking properties of the coating [56]. Chao *et al*. [189] have recently studied the behaviour of Pt/Ir, in the form of a Pt/Ir multilayer and as a compound, on a WC/Co substrate, by using different types of glass (N-PK, N-FK, P-SK, L-NB, N-PS)[32] under N_2 atmosphere. The Pt/Ir multilayer films showed severe sticking to P-SK and L-NB glasses. Moreover, glass elements diffused into the film and even some detachment was observed. Pt/Ir compounds displayed better anti-sticking capability. The diffusion of Co from the substrate to the glass/film interface triggers the reaction between glass and coating. This effect was avoided using Ta as a diffusion barrier.

The physical, microstructural as well as molten glass wetting characterizations are essential to determine the suitability of the systems as protective mediums for GMDs, but they are not sufficient to establish the duty life of the coatings. In order to assess the lifetime of the coating, the tests proposed by Klocke [181] are recommended. This method and its equipment have been recently introduced and are still under development. Therefore, the prediction of the lifetime of the RuAl/SS system as glass-mould coating is beyond the scope of this work.

Despite the interesting properties of intermetallic compounds (IMCs) (see section 1.3), they have not been fairly considered as protective coatings for GMDs. Zhong *et al*. [59] tested the wettability of NiAl films with molten borosilicate glass (Tg ~ 820 °C). A desired non-wetting response ($\theta > 90°$) of B2-NiAl films was observed in the whole temperature range studied (600-1150 °C). For this reason, the RuAl IMC is proposed here as a potential candidate material for GMD protective coatings. Due to its high melting point (2060 °C), it offers high thermal stability and oxidation resistance (see section 1.3.2) The RuAl/SS films have shown good stability after annealing for 6 h at 750 °C (see chapter 5). The oxidation resistance is given by the growth of a protective α-Al_2O_3 layer, which possesses a CTE of around the same value than that of RuAl ($\alpha \approx 5 \times 10^{-6}$ K^{-1} and $\alpha \approx 6.6 \times 10^{-6}$ K^{-1} for Al_2O_3 and RuAl, respectively) [46]. α-Al_2O_3 formed at temperatures as low as 750 °C with no growth of transient alumina being detected (see chapter 6). In the present study, the wetting of RuAl films by molten borosilicate glass is evaluated, as well as the microstructural changes induced during the process. This analysis is expected to serve mainly as an evaluation for the possible application of RuAl films as protective coatings in GM tools.

31) *Tg* = 846°C. *Chemical composition*: 56.99 SiO_2 –B_2O_3 6.12 – Al_2O_3 8.78 – MgO 6.5 – CaO 19.64 – Na_2O 0.61 – Fe_2O_3 0.13 – TiO_2 0.44 – F 0.70.

32) Nomenclature of different glass types (Schott AG).

7.2. Fundamentals of wetting

A liquid in contact with a gas forms a minimal interface. Intermolecular forces are balanced inside the liquid, but not at the surface. Forces at the interface act to minimise the surface, giving origin to *surface tensions*, as shown in Figure 7.3. The surface tension σ (in N/m) is defined as the force F_p per unit length acting perpendicular to the perimeter, and it is equivalent to the surface free energy per unit area, γ (in J/cm^2).

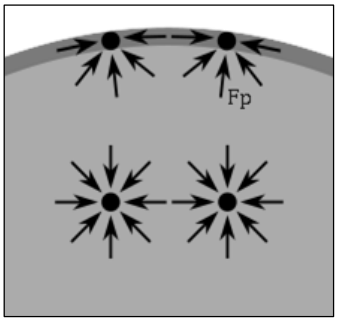

Figure 7.3: Intermolecular forces acting at the surface and inside of a liquid drop.

Each of the solid/liquid, solid/gas and liquid/gas interfaces is represented by a determined surface free energy per unit area (γ_{sl}, γ_{sg} and γ_{lg}, respectively). Direct measurement of γ_{sl} and γ_{sg} is not possible because of the absence of solid-surface mobility. Very useful information can be derived from *sessile drop* measurements, being the simplest method for the characterisation of solid surface energies. A droplet of liquid with known surface energy is placed on the analysed surface and its shape is registered, as shown in Figure 7.4. The surface energy of the solid sample can be estimated from the contact angle θ formed by the liquid droplet and the surface, together with the known surface energy of the liquid. Through θ, the system tends to minimise its free energy and, therefore, it is characteristic of a particular solid/liquid/gas system. Contact angle and interfacial energies on smooth surfaces are related according to Young's equation (Equation 7.1), which indicates the condition of zero net force along the direction tangent to the solid surface [190].

$$\gamma_{sg} = \gamma_{sl} + \gamma_{lg} \cos\theta_Y \qquad (7.1)$$

The boundaries of this restriction lay in the prediction of complete wetting when $\gamma_{sg} > \gamma_{sl} + \gamma_{lg}$ and zero wetting when $\gamma_{sl} > \gamma_{sg} + \gamma_{lg}$.

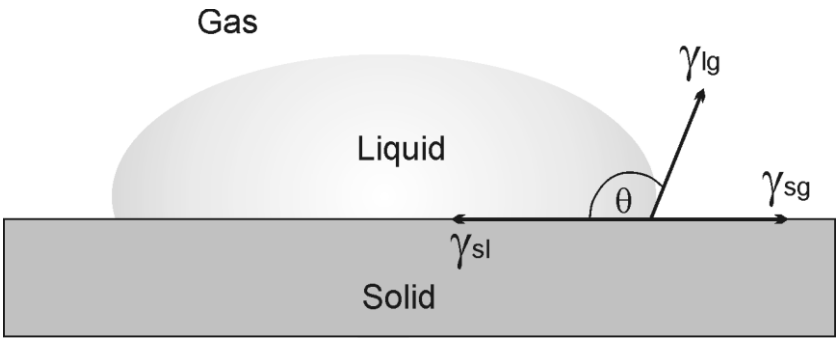

Figure 7.4: Relationship between surface tensions in a solid/liquid/gas system. The angle θ_Y relates γ_{sl}, γ_{sg} and γ_{lg} through Young's equation, adapted from [190].

The adhesion of a liquid to a solid surface can be expressed in terms of the amount of work per unit area necessary to completely remove the liquid from the substrate. This situation is represented by Young-Dupre's equation (Equation 7.2) [190].

$$W_{adh} = \gamma_{lg}(1 + \cos\theta) \qquad (7.2)$$

Young's model is valid for ideal flat surfaces, given that θ is very sensitive to local changes in surface energy and substrate topography. Since real surfaces are not perfectly smooth, the measured contact angle might suffer variations and consequently, in presence of rough surfaces display some level of hysteresis (Equation 7.3), showing higher (advancing angle θ_a) or lower (receding angle θ_r) values than equilibrium (θ_Y).

$$H = \theta_a - \theta_r \qquad (7.3)$$

Wettability refers to the relative adhesion of two fluids (liquid-liquid or liquid-gas) to a solid surface. It can be defined as the preferential tendency of a fluid to wet a solid surface in the presence of another fluid. The wetting is related to the shape of a liquid drop on a rigid surface. Figure 7.5 shows a liquid droplet on a solid surface surrounded by air, for different wetting conditions. A low contact angle (< 90°) indicates wetting of the surface (*hydrophilic surface*), with the fluid spreading over a large area. In this case, the driving force for wetting is the lowered surface energy by the liquid. High contact angles (> 90°) indicate that wetting of the surface is not favoured and thus, the fluid minimises the contact by forming a compact droplet (*hydrophobic surface*) [191].

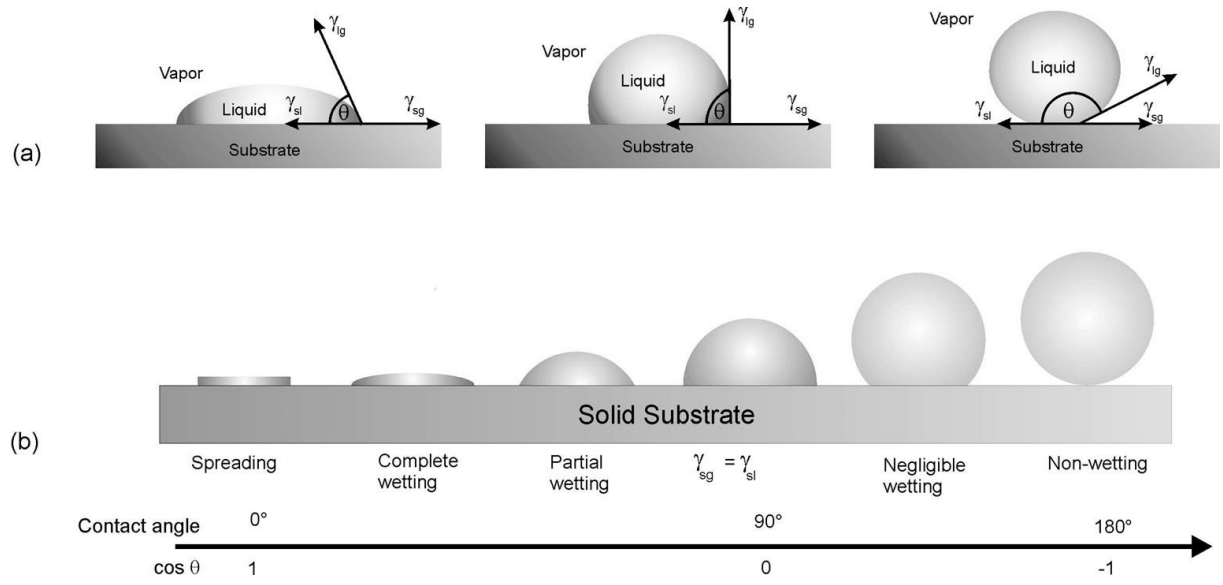

Figure 7.5: a) Wetting conditions for a liquid on a solid surface, b) wetting degrees described by shape and contact angle, adapted from [190].

During wetting studies at high temperature, the contact angle could be affected by the temperature, exposure time, atmosphere, surface roughness, composition, crystal structure and surface pre-treatments. Wetting could also involve the chemical interaction between the liquid and the solid surface. Therefore, different situations can be identified, such as: *homogeneous solid surface* (ideal case and without interface reaction), *heterogeneous solid surface* (without interface reaction), and *homogeneous solid surface* (with interface reaction), among others. In the particular case of wetting on a heterogeneous surface, the apparent contact angle value will be between those which would result from measuring on two different materials (Figure 7.6b). Figure 7.6 shows the most common wetting measurements at high-temperature. More detailed information on heterogeneous and reactive systems can be found elsewhere [190,192].

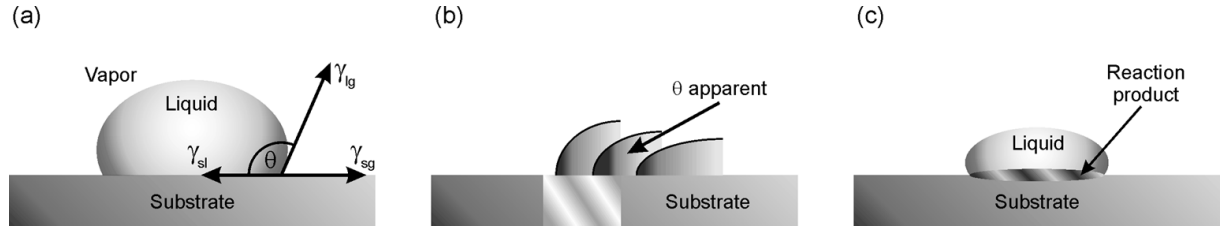

Figure 7.6: Schematic diagrams of the contact angle of a liquid drop on a) a homogeneous solid surface without interface reaction; b) a heterogeneous solid surface without interface reaction; and c) a homogeneous solid surface with interface reaction. Adapted from [59].

7.3. Experimental: contact angle measurements

The molten-glass/RuAl film contact angle measurements were carried out with a modified sessile drop technique. The contact angle measurements using the static sessile-drop technique were performed at the "Research Institute for Precious Metals + Metals Chemistry" (FEM), located in

Schwäbisch Gmünd, Germany. A glass bead was placed on a RuAl/SS sample at room temperature as shown in Figure 7.7. Then, the complete system was heated up to the measurement temperature. The sample was illuminated with white light in order to produce good contrast with the background. In this way, the base line could be easily identified and the error in the contact angle measurement minimised. The contact angle was registered by a CCD camera at 50 °C steps and then determined from the horizon line and the glass bead surface. The measurements were echeloned every 50 °C from 600 to 1050 °C, and isothermally at 1050 °C, heating rate 10 °C/min in both cases, as shown in Figure 7.8. Echeloned measurements allow the determination of the glass/metal wetting temperature, whereas isothermal measurements can determine the time required for contact angle equilibrium.

The tests were carried out in both RuAl/SS and SS samples in order to study the influence of the coating on the wetting properties. The RuAl film thickness was 1.2 µm. The analysis was carried out under air and Ar flux atmospheres. Since the chamber (Figure 7.7) was not connected to a vacuum system, the Ar atmosphere was composed of a mixture of Ar and air. Commercial borosilicate glass beads (T_g ~ 820 °C) with a chemical composition of 81% SiO_2, 13% B_2O_3, 4% Na_2O and 2% Al_2O_3 and 3 mm diameter were used for the wetting experiments. In order to keep the glass beads on the flat substrate surface, they were previously facetted. Since only few works about intermetallic coatings (NiAl) for GMD have been found in the literature [59,184], the test conditions (glass type, temperature, atmosphere, etc.) were selected in order to evaluate the response of the RuAl system in contrast to NiAl.

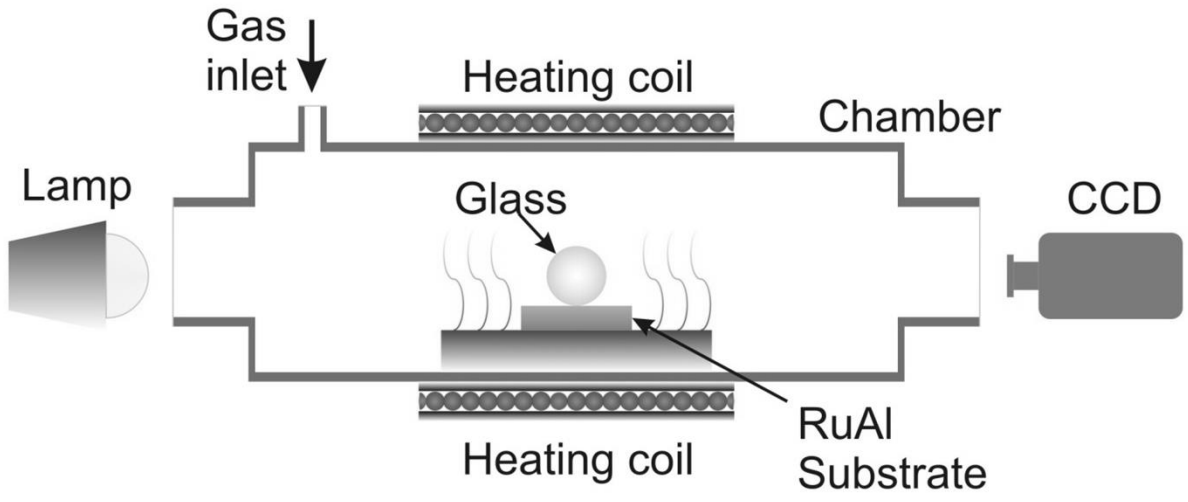

Figure 7.7: Schematics of the experimental set-up for the contact angle measurement at high temperature performed by the sessile drop method.

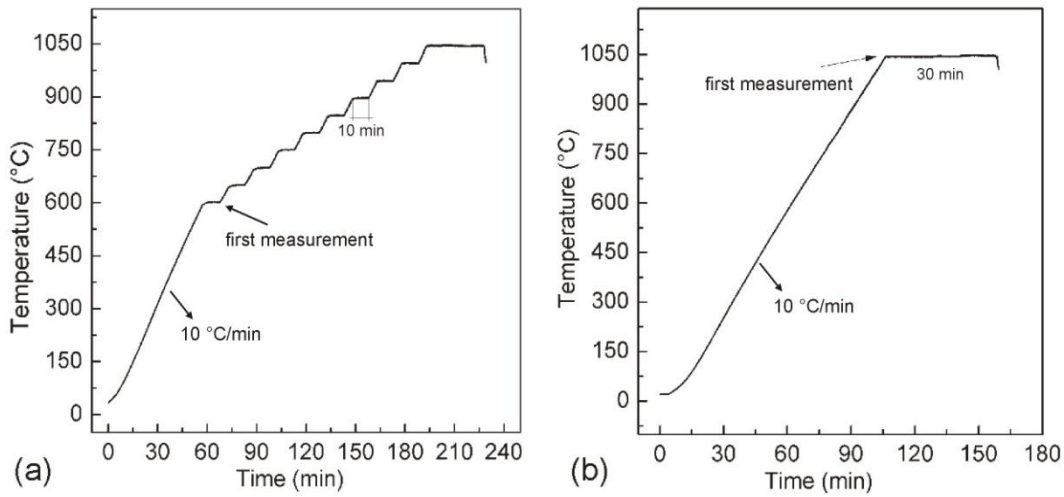

Figure 7.8: Temperature curves for the a) heating steps and b) the isothermal, both heated at 10 °C/min.

7.4. Results and Discussion

7.4.1. Wetting analysis

a) Contact angle measurements

Non-wetting of the mould material is a basic requirement in of glass lenses by moulding manufacture, since it is directly related to the work of adhesion (Equation 7.2). Figure 7.9 shows the variation of the contact angle between molten borosilicate glass and RuAl films, under Ar and Air atmospheres, as a function of the temperature. The wetting condition ($\theta < 90°$) has not been reached under air or Ar atmospheres for the whole analysed temperature range. However, a slight drop in the contact angle was observed at temperatures slightly above T_g. Shape changes in the glass beads due to temperature are also shown in Figure 7.9. The decrease in contact angle and enlargement of contact radius were certainly identifiable. By increasing the temperature, the γ_{lg} of the glass was reduced due to a decline of the attraction forces at the glass surface. Consequently, θ also diminished. The measurement errors resulted from averaging five measurements at each temperature during 10 minutes. No change or only slight variations in the contact angle during measurements indicate contact angle equilibrium, deriving in narrow error values, as observed for most temperatures. For higher temperatures (≥1000 °C), the contact angle is probably not at equilibrium during the analysis, resulting in larger error bars due to the molten glass spreading. Wettability studies performed on NiAl intermetallic films have shown non-wetting behaviour ($\theta > 90°$) with molten borosilicate glass (Tg ~ 820 °C) up to 1150 °C [59]. However, information regarding glass/film interaction and film surface after contact angle measurement is not provided here.

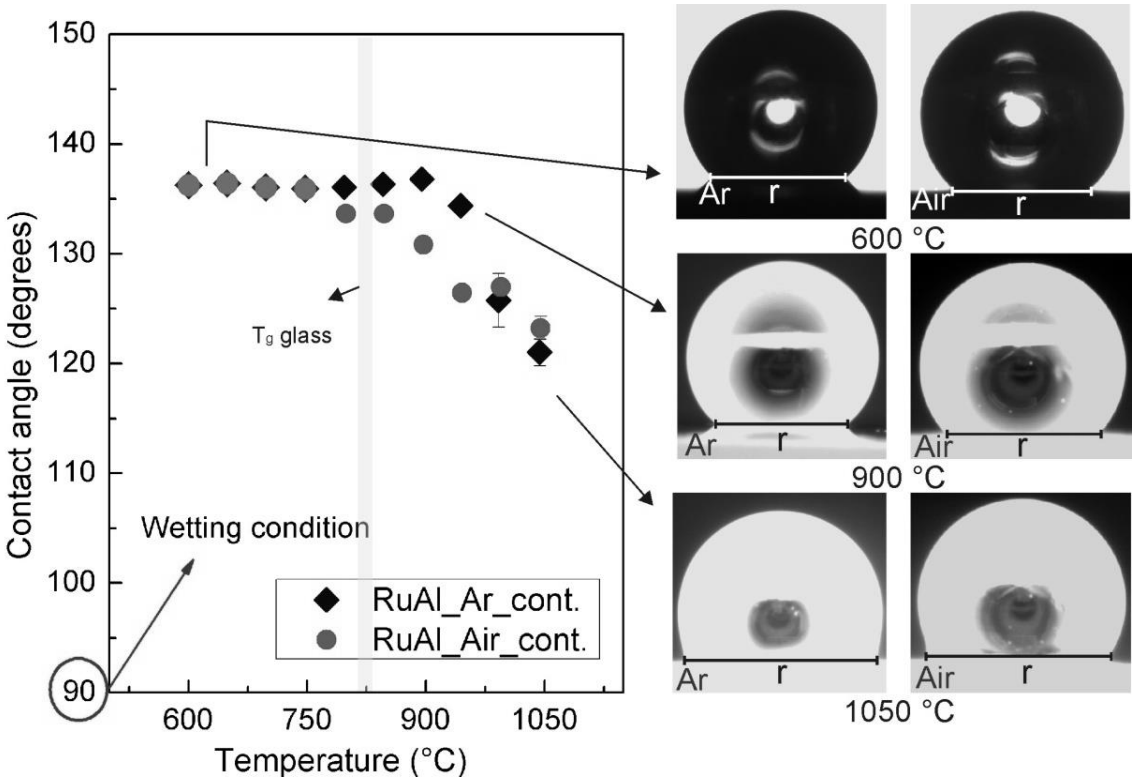

Figure 7.9: Evolution of the contact between molten borosilicate glass and RuAl/SS system as a function of temperature under air and Ar atmosphere. The shape variation of glass beads is shown at three temperature stages. The measurements were made following the process described in Figure 7.7a.

Figure 7.10 shows the contact angle evolution of molten glass on SS and RuAl/SS under air and Ar atmosphere. Wetting of the SS substrate has been observed at about 1000 °C. The glass wetted SS with final contact angles of 55° and 75° under air and Ar atmospheres, respectively.

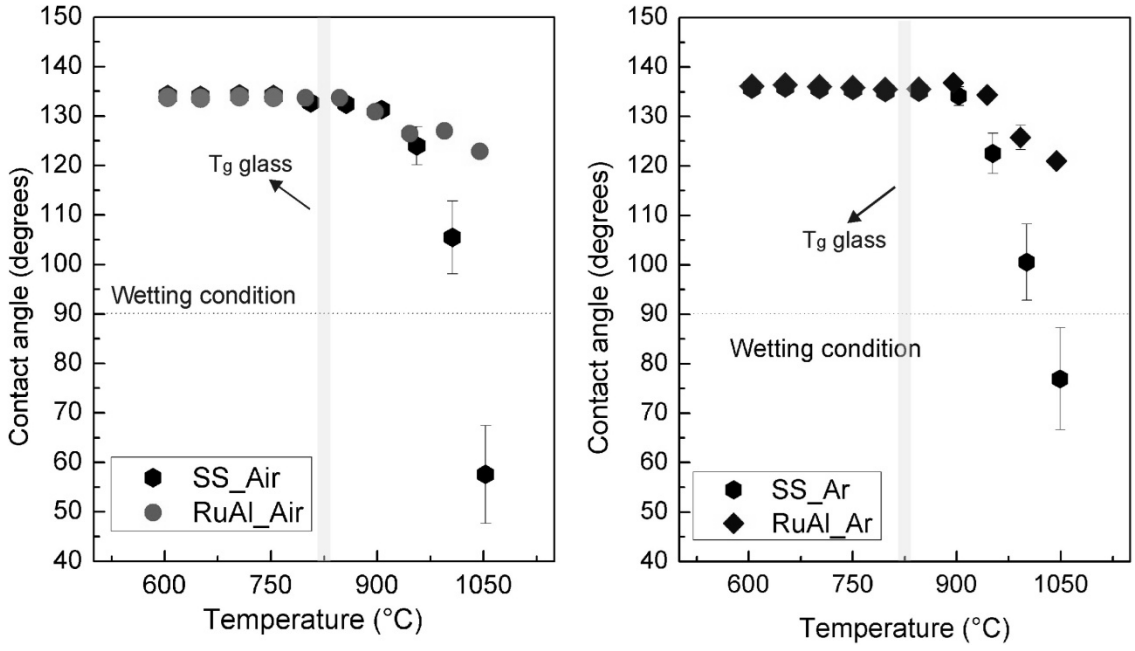

Figure 7.10: Contact angle of molten glass on RuAl films and SS substrates in (a) air and (b) argon-air atmosphere.

Figure 7.11 shows the evolution of the contact angle on RuAl coatings at 1050 °C. The decreasing contact angle achieved a final value, which was higher under Ar than under Air, ~81° and ~71°, respectively. Considering that the mould processing time at T > T_g is about 10 min (see Figure 7.2), the non-wetting behaviour of RuAl by molten borosilcate at elevated temperature (1050 °C) is an essential advantage of this compound for the mentioned application.

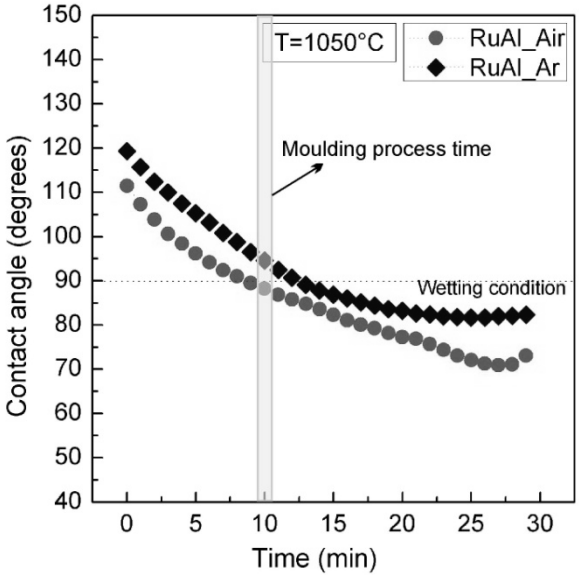

Figure 7.11: contact angle as a function of time, for molten glass and RuAl thin films at 1050 °C. The measurement was made following the heating of Figure 7.7b. The moulding process time according to Figure 7.2 is also indicated in the graphic.

b) Surface tension analysis

Since the surface tension of metals is generally reduced when oxygen is adsorbed on their surface [192], the change in the RuAl surface tension in presence of an Al_2O_3 layer was evaluated measuring the contact angle at room temperature. The γ_{sg} of unoxidised and oxidised RuAl samples were calculated from a single contact angle measurement by using a liquid with known surface tension (deionised water). The empirical relationship given by Equation 7.4 was used to this goal, which is called state theory equation and has been derived from Young's equation (Equation 7.1) and thermodynamic considerations [Krüss manual[33], 192]. The constant β in the exponent has a value of 1.247 x 10^{-4}. Knowing the liquid surface tension γ_{lg} and the contact angle θ, it is possible to determine the solid surface tension γ_{sg}.

$$cos\theta = -1 + 2\left(\frac{\gamma_{sg}}{\gamma_{lg}}\right)^{1/2} exp\left(-\beta(\gamma_{lg} - \gamma_{sg})^2\right) \qquad (7.4)$$

The surface tension of SS and RuAl films measured in air at room temperature corresponds to atmospheric conditions. Since both metals rapidly adsorb oxygen to form nm-thick layers, the real

33) *http://www.kruss.de/en/theory/measurements/contact-angle/models/equation-of-state.html*

surface tension is not easily calculated. The surface energy of oxidised RuAl films was also calculated to analyse the influence of oxide growing at the surface. Table 7.1 shows γsg values from the SS and RuAl samples.

Table 7.1: Surface energy values from the SS substrate, and RuAl films. Details about the thickness and microstructure of the oxide scale are shown in chapter 6. *The high level of spreading did not allow a statistical measurement.

Sample	Surface energy [mJ/m^2] (calculated by Eq. 7.4)
SS substrate	150.2 ± 3.1
RuAl films (not oxidised)	162.4 ± 3.4
RuAl films (oxidised 60 min at 750 °C)	153.7 ± 1.4
RuAl films (oxidised 30 min at 900 °C)	150.1 ± 2.4
RuAl films (oxidised 50 min at 900 °C)	~131*

The surface tension of RuAl films decreases when an oxide scale is grown on the surface, as indicated in Table 7.1. Gaseous environments containing oxygen may affect the surface energies γ_{sl}, γ_{sg} and $\gamma_{lg,}$ when the solid or liquid are sensitive to oxidation or gas dissolution [190]. During measurements at high temperature, the variation in the surface tension of the solid substrate with time and temperature will occur, as a consequence of oxide growth, thus affecting the contact angle.

In RuAl films, the roughness increased during oxide growth, as seen in chapter 6. Since deviation from equilibrium contact angle is usually observed on rough surfaces, a decrease in θ will be detected during the contact angle measurements [190,192].

Physicochemical reactions, such as substrate oxidation, may contribute to the misinterpretation of experimental results, because the contact angle is particularly sensitive to changes in the surface energy. Such is the case of Au and Ag, where γ_{sg} decreases in presence of oxygen as a result of its adsorption [187]. The formation of a thin oxide film at the Ag surface also leads to a reduction of γ_{sg}, allowing the contact angle to increase. However, at the same time, a reduction in γ_{sl} caused by the dissolution of the oxide results is an increased driving force for wetting, thus reducing the contact angle. An analysis using Young's equation assumes a system in equilibrium. In most real cases, at high temperature, the solid surface adsorbs oxygen forming an oxide layer, which changes the equilibrium conditions at the triple line.

7.4.2. Glass/substrate interface characterisation

a) Analysis of the SS substrates

The substrate surface was investigated after wettability measurements, using optical microscopy, SEM and chemical analysis. The contact area between glass and SS substrate samples is delimited

by a well-defined circumference. However, remnants molten glass was found stuck to the surface after contact angle measurements (Figure 7.12). The central zone shows evidence of severe chemical attack at grain boundaries, which lead to the formation of grooves through which the molten glass could penetrate the material. The same behaviour was observed by Pech *et al.* in [194]. Thus, it can be stated that uncoated SS do not provide the required anti-sticking properties for the selected test conditions, due to the interaction with the glass.

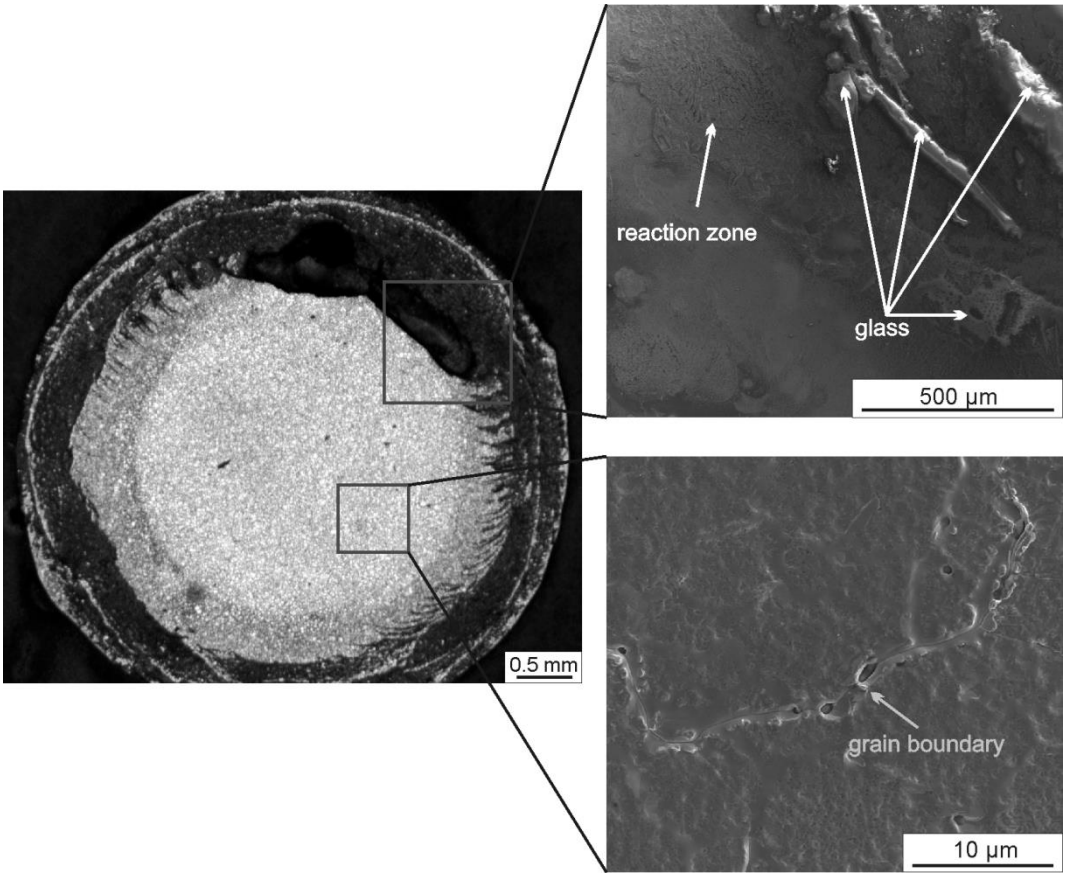

Figure 7.12: Optical and SEM images of SS after wetting measurement. Glass remnants adhered to the metal and chemically attacked grain boundaries.

b) Analysis of the RuAl films

Figure 7.13 shows the surface of a RuAl/SS sample after sessile drop test carried out at up to 1050 °C (echeloned), together with the corresponding chemical analysis performed by EDX. Both samples tested (under air and under Ar atmospheres) showed similar morphology, thus only one is displayed. Concentric rings of different chemical composition are observed. The inner region corresponds to the area enclosed by the glass bead at the beginning of the experiment and was composed mostly by Ru and also by elements from the SS substrate. This results from the exposure of the Al-depleted zone after the dissolution of Al_2O_3 by the molten glass in this contact region (Figure 7.13d). The microstructure of oxidised films has been already described in chapter 6. The outer ring showed high quantities of Ru, Fe and Cr and also small regions of Al_2O_3. Outside the

droplet perimeter, Al oxide grew at the surface above the corresponding Al-depleted zone (Figure 7.13c). EDX measurements comparing the chemical composition of different regions are shown in Figure 7.13b. Very small quantities of Si (~1 at.%) were also detected in some regions of the sample, likely originating from the glass bead. Since no remains of adhered glass were observed, Si might have been retained at grain boundaries, as observed by Pech *et al*. [194].

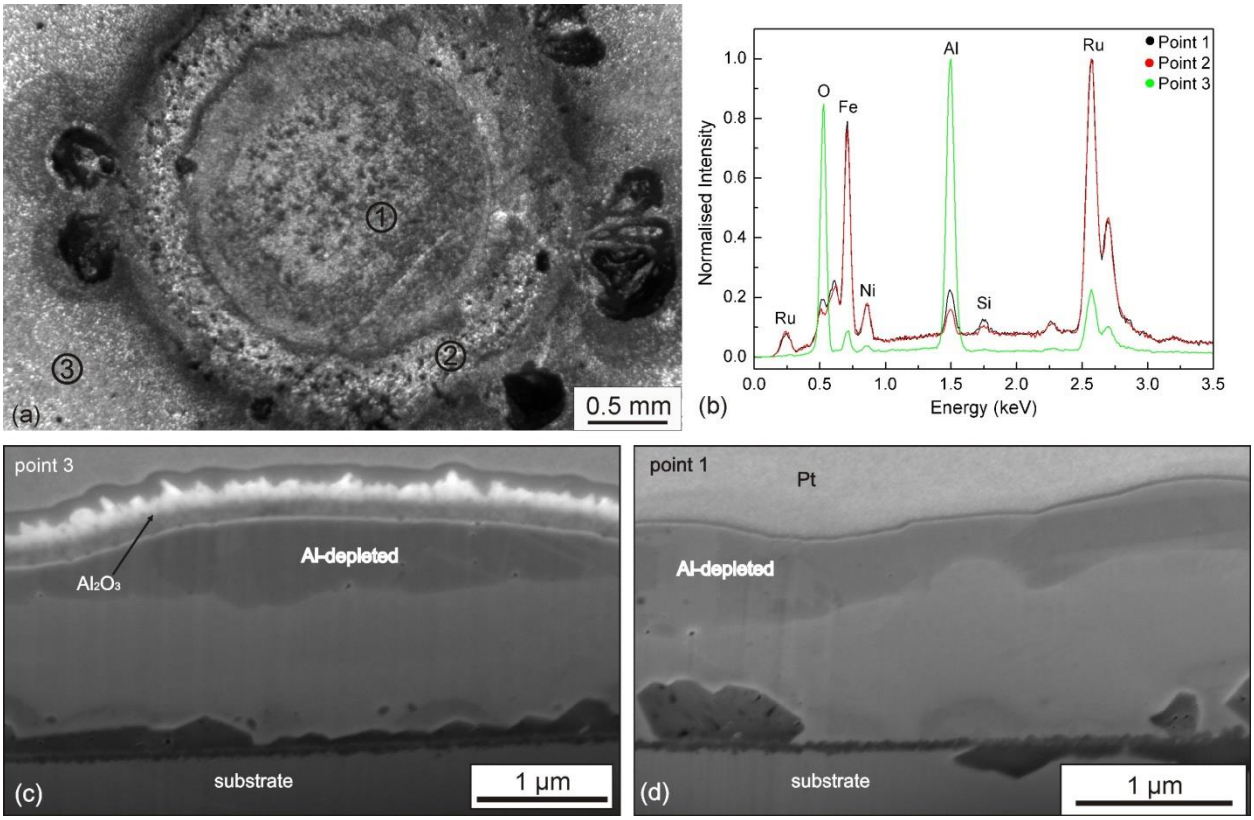

Figure 7.13: (a) Optical image showing the glass-contact region after the wettability test up to 1050 °C (echeloned); (b) EDX chemical analysis of the different zones; (c) and (d) cross-section SEM image from zones 3 and 1, respectively. The final contact angle was θ_f >120°.

The samples measured isothermally (1050 °C) presented ramified morphologies, contrary to the echeloned measurements, which displayed reaction zones with sharper borders (Figure 7.14). As in the previous case, different regions of dissimilar structure and composition were found around the glass droplet. Chemical and microstructural analysis of the inner circumference showed similar results to those previously presented, with dissolution of Al_2O_3 also occurring at the central region (Figure 7.14). The outer zone showed a ramified morphology with dark sub-regions composed mainly of Ru, Fe and Cr and bright sub-regions containing aluminium oxide and an Al-depleted zone of Ru(Cr,Fe). A comparison of the chemical composition is displayed in Figure 7.14b. Moreover, outside the droplet perimeter, the Al oxide layer and Al-depleted zone were also present. The ramified morphology emerges as consequence of the different spreading rates of molten glass on the heterogeneous surface. This is due to the presence of rough Al_2O_3 and Fe-Cr oxides at film defects, formed during the oxidation of RuAl films. High spreading of the liquid occurred on the

highly oxidised samples at RT using water (see analysis of Table 7.1), given the decrease in the surface energy in presence of oxides. From this behaviour, it can be concluded that the presence of oxides at the surface also leads to higher spreading of the molten glass. Additionally, some quantities of Si were detected in the different regions, probably retained at the grain boundaries, as also mentioned in the previous case.

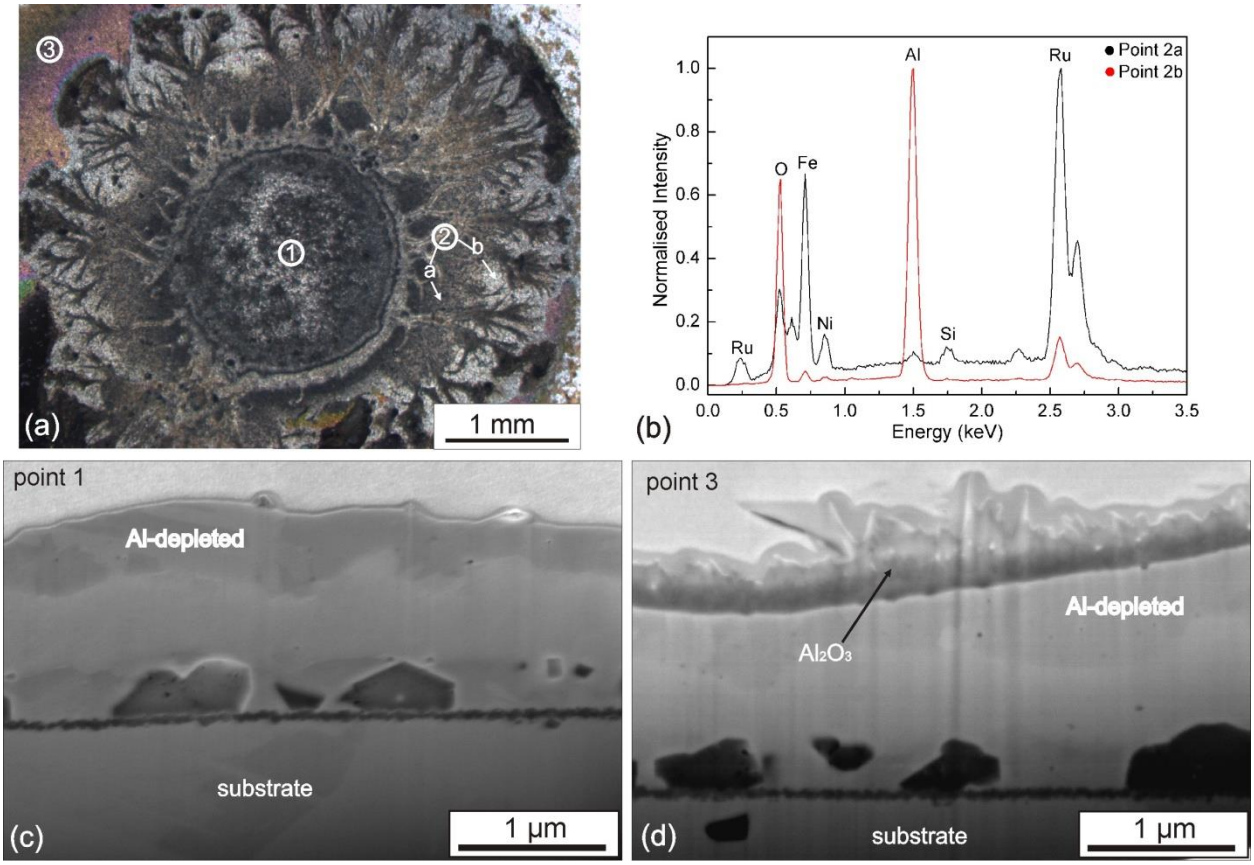

Figure 7.14: (a) Optical image showing the glass-contact region after wettability tests at 1050 °C (isothermal); (b) EDX chemical analysis of sub-regions 2a and 2b; (c) and (d) cross-section SEM image from zones 1 and 3, respectively. The final contact angle was θ_f <90°.

c) Analysis of the glass beads

Glass beads were further analysed regarding the reaction and interdiffusion between the films and the molten glass. After contact angle measurements in Ar atmosphere, no substrate elements were found in the glass, remaining translucid (Figure 7.15a). However, after measurements in air, the glass bead showed some degree of opacity and evidenced chemical reaction, given by the presence of Fe and Cr along with Ru (Figure 7.15).

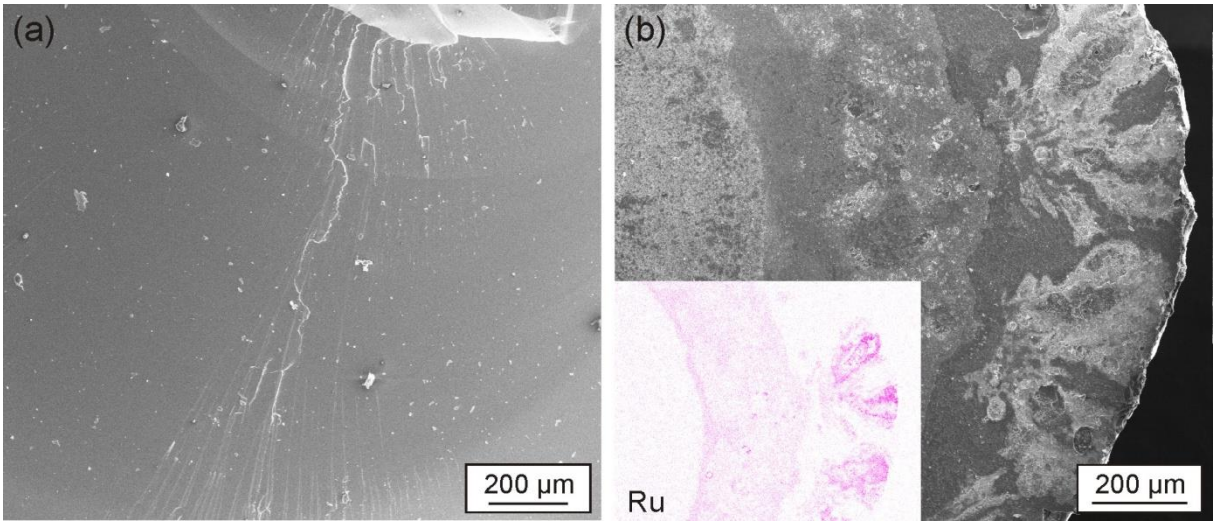

Figure 7.15: SEM images of the glass bead after contact angle measurement under (a) Ar and (b) air atmosphere. The inset image shows the Ru distribution obtained by EDX, corresponding to the whole sample area of (b).

From these results, it was observed decreasing contact angles between glass and RuAl films under air starting at $T \cong T_g$, which is about 150 °C lower than for those under Ar. This difference might be given by the oxide growth, which should be faster under oxidising atmospheres than in less oxidising ones. However, the final contact angle is about the same for both conditions, which corresponds to the Al_2O_3/glass contact. Additionally, from contact angle and microstructural analyses, it was observed that glass sticks to SS but not to RuAl films. This was in part evidenced by the work of adhesion represented in Equation 7.2. Assuming constant γ_{lg} at a certain temperature and atmosphere, the work of adhesion increases as the contact angle is lowered. Since θ is lower for SS than for RuAl (under air and Ar atmospheres, see Figure 7.10), a higher adhesion was expected.

No qualitative difference regarding oxidation and interface reaction has been observed among samples measured under air and Ar. This is due to the relatively high levels of oxygen also present in the Ar atmosphere. However, even if a controlled atmosphere (i.e. under Ar, vacuum, N, etc.) were used, the oxidising agents present in inert gasses are enough to cause some level of oxidation in highly reactive elements, such as aluminium [190].

The presence of O_2 in the chamber induces changes in γ_{sl}, γ_{sg} and γ_{lg}, due to physicochemical interactions with the solid and/or liquid surfaces. This alters the contact angle and thus the wetting behaviour, as previously detailed in section 7.4.1. The wetting of metals by molten glass in air (or oxidising atmospheres) usually involves interfacial reaction wetting, mainly related to oxidation of the solid surface. Furthermore, glasses tend to wet oxide components because of the similarity of the binding forces [190]. Therefore, an increase in wetting can occur if the metal surface has been oxidised either during pre-treatments or in-situ during contact angle measurement. Furthermore, surface roughening of the substrate might occur at high temperatures, as consequence of the

formation of a layer of reaction product growing ahead of the triple line or by the accumulation of fine precipitates. This might perturb the triple line due to droplet deformation and dissolution of reaction products [192]. Copley *et al.* [188] related the wetting of Pt and Rh by E-glass to the stability of their oxides. They proposed that the presence of glass may increase the temperature at which the substrate oxide can exist at the glass/metal interface, by changing the surface energy and locally increasing the pressure. The spreading force exerted by the glass is due to the requirement of metal atoms to bond with oxygen. This condition is partially satisfied by sharing non-bridging oxygen ions from the molten glass. Thus, the competition between substrate metal ions and cations in the glass determines the level of glass/metal wetting.

Substrate material also plays a very important role in the wetting response at high temperature. Even a small amount of substrate elements dissolving in the droplet is enough to affect wetting and significantly decrease the contact angle [192]. In the case of SS substrates, Fe and Cr might diffuse into the protective coating and arrive at the coating/glass interface, where they react, affecting the optical properties of the glass. Diffusion of substrate elements into the glass was noticed only in the samples tested under air. For CrN films, Ma *et al*. [56] observed higher contact angles using WC and SiC substrates instead of M42 steel. Stable substrates have shown to prevent diffusion of undesirable elements into the coating, avoiding its degradation. Zhong *et al*. [59] observed different behaviours in boron nitride when wetting with borosilicate glass under air and vacuum. In vacuum, good wettability response was observed ($\theta>90°$, no glass/substrate interaction) up to ~ 700 °C. However, under air, bubbles form within the glass due to oxidation of BN and the release of gaseous B_2O_3, resulting in wetting of the substrate, which is a major drawback for the manufacture of high quality lenses [59].

RuAl film properties, such as oxidation resistance (see chapter 6) and wettability by molten glass, might degrade in the presence of impurities diffused from the substrate (Cr and Fe). Moreover, the contact behaviour of molten glass changes with the oxidation of the substrate surface. Since molten glass often dissolves additional oxides up to a saturation concentration, a strong chemical bond may be formed at the interface, resulting in increased adhesion.

7.5. Summary and outlook

In the present work, RuAl thin films have been evaluated as potential candidates to be applied as protective coatings for GMDs. The wetting of RuAl films by molten borosilicate glass has been studied, as well as the microstructural changes induced during the process. Based on the analysis of the contact angle, RuAl films deposited onto SS have shown good non-wetting response ($\theta > 90°$ for the processing time), which is a prerequisite for glass moulding. For both analysed conditions, air and Ar atmospheres, wetting was not observed ($\theta > 90°$) up to 1050 °C. Dissolution of aluminium

oxides occurred at the initial contact region, which was evidenced by the only presence of Al-depletion below. Chemical interaction was more intense in the samples measured in air, with substrate elements detected in the glass (Ru from the film and Fe-Cr from the SS substrate), which showed some grade of opacity. Elements diffusing from the SS substrate into RuAl alter the reaction between film and glass, affecting the wetting conditions and the glass transparency. Moreover, the growth of non-protective oxides (Fe/Cr oxides) at the film defects had a negative effect on the wetting, causing different spreading behaviours of the molten glass. The addition of diffusion barriers between the film and substrate might be advantageous in reducing the impurity transfer from the substrate into the RuAl film.

Since the material selection for GMD coatings is strongly influenced by the type of glass that will be shaped, further studies might be useful to evaluate the wetting behaviour of RuAl with a wide range of glass (chemical) compositions. Additionally, given that the wetting behaviour depends on the whole system (substrate/coating) and not only on the individual components, RuAl and molten glass should be analysed using diverse substrates, so as to avoid the incorporation of detrimental elements at the glass/substrate interface. However, the physical and microstructural analysis presented in this work, is a useful starting point for the evaluation of the suitability of the selected system as a protective medium for GMDs.

8

Summary and Outlook

8.1. Summary

The synthesis and high-temperature characterisation of RuAl films using technically relevant substrates have been studied for the first time in this work. This is of high relevance for the future high-temperature application of this intermetallic compound.

Single-phase RuAl intermetallic compound was synthesised on stainless steel (SS) substrates by using sequential Ru-Al deposition and a subsequent annealing. The as-sputtered films were composed of Ru/Al MLs with individual thickness around 1-2 nm and reaction zones identified as RuAl. The last is formed, in part, due to the creation of a co-deposition region between the Al and Ru targets, given the high-spatial distribution of the sputtered material. Furthermore, interdiffusion at the Ru/Al and Al/Ru interfaces was also evidenced by XRD and SAD measurements. After annealing the samples, the multilayer structure rapidly disappears given rise to single-phase RuAl films. The small bilayer period leads to rapid homogenisation of the multilayers, thus avoiding intermediate intermetallic phases to grow and allowing the B2-RuAl to form at temperatures as low as 280 °C. It is essential to mention the formation of RuAl films with ~4 at.% Ru off- stoichiometry, expanding the existence range of the single-phase known for bulk RuAl. During the annealing of the films, texture in the {100} crystallographic orientation is developed with in-plane compressive stresses of about 1.6 GPa, which are mainly due to the CTE mismatch between the SS substrate and RuAl. No significant difference in stress values were found for the RuAl films using a Ti adhesion layer or sputter cleaning. However, a higher critical load L_c was observed during scratch testing of the film with a Ti adhesion layer instead of a sputter-cleaned surface.

Microstructural and grain growth kinetic analysis were performed after thermal treatments at 650 °C, 700 °C and 750 °C for periods of time ranging from 1 to 6 h. XRD measurements on RuAl thin films annealed at the mentioned temperatures for 6 h have shown that only B2-RuAl is present, maintaining the preferred crystallographic orientation along the {100} planes parallel to the surface, for all annealing conditions studied here.

Thermal studies showed that temperatures as low as 650 °C are not sufficient to activate the grain growth. However, annealing for 6 h at 700 °C and 750 °C increased the grain size from about 24 nm at room temperature up to 54 nm and 107 nm, respectively. The isothermal grain growth of RuAl thin films obeys the generalised power grain-growth model and its exponent *n* was found to be dependent on the temperature. For most of the temperatures and times used, normal grain growth of RuAl films has occurred. However, abnormal growth was observed for 6 h at 700 °C and 4 h and 6 h at 750 °C. From the possible mechanisms of abnormal growth, we conclude that the presence of impurities and grain-orientation-specific driving forces were responsible for the observed behaviour. The corresponding activation energy for grain growth in NC RuAl has been found to be 145 ± 14 kJ/mol, which is in agreement with reported values for other B2 NC IMCs. The ratio of the activation energy for lattice diffusion in bulk-RuAl (from literature) and that obtained from this work was 0.61 ± 0.01. This indicates that the grain growth in NC RuAl is highly dominated by grain boundary diffusion, given the high volume fraction of grain boundaries in comparison to CG materials.

Additionally, the diffusion of Fe and Cr from the substrate and their subsequent incorporation into the RuAl lattice as substitutional elements has been verified by the variation of the lattice parameter, which reduces its values as impurity levels increase with the annealing time.

From the isothermal oxidation studies of RuAl thin films using two different substrates (SS and Al_2O_3), it was observed that the high density of grain boundaries in NC RuAl allowed the rapid outward diffusion of Al through short paths, promoting the formation of α-Al_2O_3 for all temperatures and times studied in this work. It is important to emphasise the growth of a stable oxide (α-Al_2O_3) at low temperatures (750 °C), where transient alumina are predominant during oxidation of other aluminides (i.e. NiAl).

Alpha alumina grew linearly in time and controlled by phase-boundary processes. The linear growth-rate was highly temperature dependent, as observed for the RuAl/SS samples oxidised at 750 and 900 °C. This work is the first to report linear kinetics in the growth of α-Al_2O_3 on intermetallic compounds. The thickening of the oxide scale gave rise to a diffusion-controlled process, which followed a parabolic law. A thickness of about 200 nm (at 900 °C) was proposed here for the transition from the linear to the parabolic oxide growth. Despite the oxide growth dominated by chemisorption processes, a net flux of Al diffusing outward to the surface was

distinguished for the systems here studied. This was demonstrated by the presence of Ru-rich particles at the oxide/metal interface, formed during the first oxidation stages, which showed that the surface was not displaced before and after oxidation. Furthermore, the outward diffusion of Al led to the creation of an Al-depleted zone beneath the oxide scale, resulting in a new Ru-rich phase, containing high quantities of Fe and Cr diffused from the SS substrate.

The microstructure of the RuAl/SS was stable after the oxidation process and the multilayered morphology of the oxide, usually observed in RuAl bulk materials, was not observed. The presence of Fe and Cr tends to avoid this type of microstructure by stabilising the Al-depleted region through the formation of a ternary compound (Fe-Ru-Cr) with a hcp structure. On the other hand, the excess of Ru from the RuAl phase can be eliminated by diffusing into the SS substrate and thus, avoiding the precipitation of new δ-Ru regions.

On the contrary, the multilayered morphology was present in the $RuAl_{(Ru\text{-}rich)}/Al_2O_3$ after 1 hour oxidation (at 900 °C). It was also not completely avoided in RuAl films with excess aluminium when Al_2O_3 is used as a substrate ($RuAl_{(Al\text{-}rich)}/Al_2O_3$). These layers also showed this morphology after oxidation at a higher temperature (1000 °C). Consequently, the excess of Al only retarded the formation of this type of microstructure.

The use of different substrates derived in the generation of distinct stress states. Tensile stresses generated in the scale during oxidation in absence of impurities, whereas compressive stresses were developed in the oxide after Fe and Cr diffused into the RuAl film, which are highly related to the stresses present in the RuAl film.

Kinetic and microstructural analysis showed that the oxidation behaviour of non-stoichimetric RuAl films was affected by the presence of Fe and Cr impurities. The kinetics analysis showed that the activation energy for aluminium oxidation on RuAl/SS (116 ± 8 kJ/mol) was around 30% higher than on $RuAl/Al_2O_3$ (90 ± 12 kJ/mol). This indicated an influence of Fe (~62 at.%) and Cr (~20 at.%) on the RuAl oxidation, possibly by the generation of energy barriers at grain boundaries. Complementarily, the diffusion of Fe and Cr into the RuAl layer decreased more than 70% by using a combination of Al_2O_3 and W layers as diffusion barriers. However, the adherence of the coating was weak mainly due to stresses generated during their deposition.

Considering a potential application as protective coatings for GMDs, the wetting of RuAl films by molten borosilicate glass has been evaluated. Based on the analysis of the contact angle, RuAl films deposited on SS have shown good non-wetting response ($\theta > 90°$ for the processing time), which is a prerequisite for glass moulding. For both analysed conditions, air and Ar atmospheres, wetting was not observed ($\theta > 90°$) up to 1050 °C. From microstuctural analysis after the contact angle measurements, the dissolution of aluminium oxides was detected at the initial contact region. Chemical interaction was more intense in the samples measured in air, with substrate elements

detected in the glass (Ru from the film and Fe-Cr from the SS substrate), which showed some level of opacity. However, no glass/substrate interaction was observed during the wetting tests carried out under Ar. Elements diffusing from the substrate into RuAl triggered the reaction between film and glass, affecting the wetting conditions and the glass transparency. Moreover, the growth of non-protective oxides (Fe/Cr oxides) at the film defects had a negative effect on the wetting, causing different spreading behaviours of the molten glass. The physical and microstructural analysis performed in this work is fundamental towards the evaluation of the suitability of the selected system as a protective medium for GMDs.

8.2. Outlook

From the results obtained during the development of the present work, new question arose, which should be answered during subsequent studies.

It was observed that the microstructure of the RuAl/SS samples remained stable after oxidation at 900 °C for different times, not presenting the multilayer morphology as that observed in the RuAl/Al_2O_3 samples. From that, it is clear that the metallic substrate plays an important role in this behaviour; however, the mechanisms acting in this case are not completely clear. For this reason, further studies should be performed to evaluate the mechanical and chemical stability of the Al-depleted zone (containing Fe and Cr), with the aim of determining the reasons behind its good performance as an oxygen diffusion barrier. Additionally, it would be also of high interest to analyse the effect of the Ru migration from the RuAl phase to the metallic substrate in the microstructure stability of the complete system.

From the wetting analysis, arose the need of complementary studies in order to deeply assess the RuAl system. Since the material selection for GMD coatings is strongly determined by the type of glass to be shaped, it will be necessary to evaluate the wetting behaviour of a wider range of glass types. Additionally, given that the wetting behaviour depends on the complete system (substrate/coating) and not only on the individual components, RuAl and molten glass should be surveyed using different substrates, in order to avoid the incorporation of detrimental elements at the glass/substrate interface. Finally, studies assessing the duty life of the coating are also needed by performing tests emulating the real process parameters.

Annexe

A) Texture measurements of annealed RuAl films

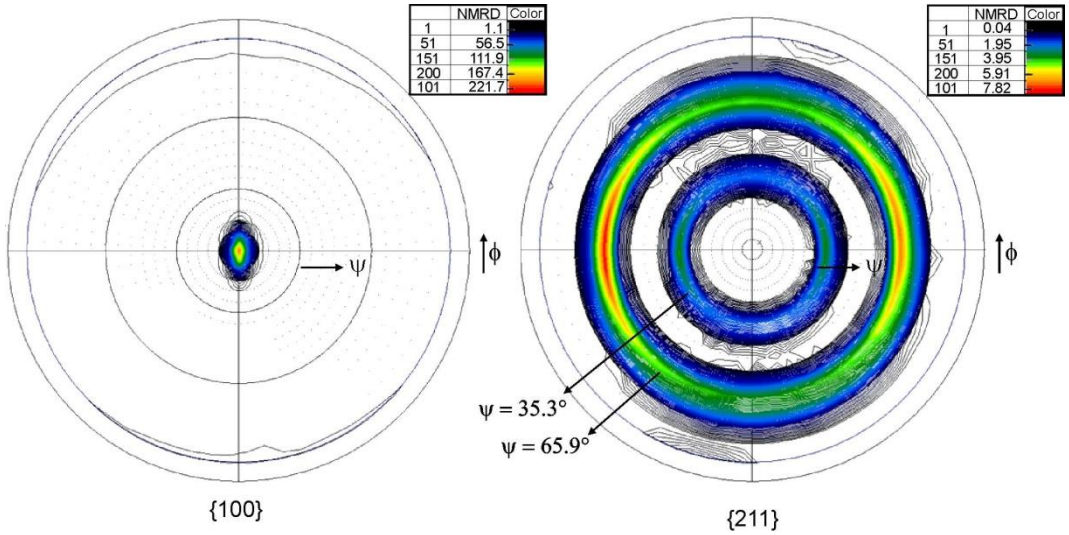

XRD pole figures for RuAl films deposited onto SS measured around a) 100 and b) 211 Bragg reflexions. The coloured scale indicates the normalised multiple random distribution (NMRD). The sample shows a strong fiber texture with the {100} planes being parallel to the sample surface. The higher intensity at the ψ angles indicated in the {211} measurement, confirmed the 100 fiber texture of the RuAl films.

B) RuAl onto Al_2O_3 substrate

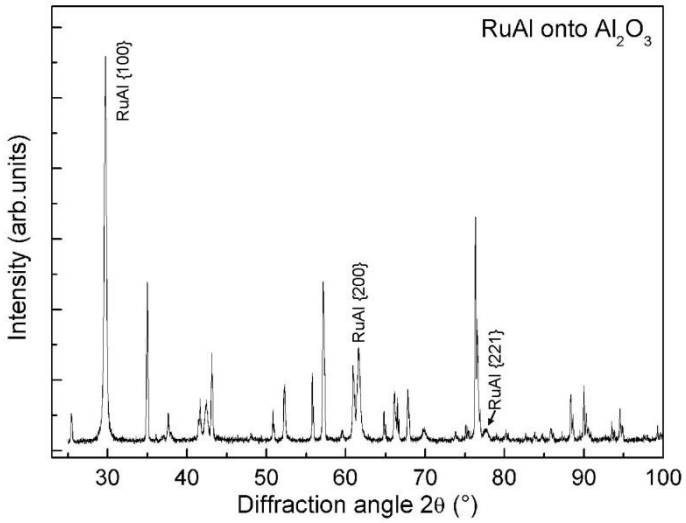

XRD (BB configuration) of RuAl film deposited on a Al_2O_3 substrate. As in the case of SS substrates, RuAl grew with a preferential orientation of the {100} planes parallel to the surface. All non-identified peaks correspond to the signal from the Al_2O_3 substrate.

C) Coefficient of thermal expansion (CTE)

Coefficients of thermal expansion corresponding to the film and substrate materials.

Element	CTE (K^{-1})
RuAl	$6 - 8 \times 10^{-6}$
Al_2O_3	$5 - 6 \times 10^{-6}$
SS	16×10^{-6}
Ru	$5.1 – 9.6 \times 10^{-6}$

9

Bibliography

[1] I.M. Wolff, Toward a Better Understanding of Ruthenium Aluminide, J. Miner. Met. Mater. Soc. 49 (1997) 34–39.

[2] F. Mücklich, N. Ilić, RuAl and its alloys. Part I. Structure, physical properties, microstructure and processing, Intermetallics. 13 (2005) 5–21.

[3] N. Zotov, K. Woll, F. Mücklich, Phase formation of B2-RuAl during annealing of Ru/Al multilayers, Intermetallics. 18 (2010) 1507–1516.

[4] K. Woll, Festkörper- und selbst fortschreitende Reaktionen in Multilagen zur RuAl-Dünnschichtsynthese, Universität des Saarlandes, 2012.

[5] Z. Li, W. Gao, High Temperature Corrosion of Intermetallics, in: Y. Berdovsky (Ed.), Intermet. Res. Prog., Nova Science Publisher, Inc. New York, 2008: pp. 1–64.

[6] G. Sauthoff, Intermetallics, WILEY-VCH Verlag GmbH, 1994.

[7] G. Sauthoff, State of intermetallics development, Mater. Corros. 47 (1996) 589–594.

[8] G.H. Meier, Research on Oxidation and Embrittlement of Intermetallic Compounds in the U.S., in: Oxid. Intermet., Wiley-VCH Verlag GmbH, 1997: pp. 15–58.

[9] H.J. Grabke, Oxidation of Aluminides, Mater. Sci. Forum. 251-254 (1997) 149–162.

[10] H.J. Grabke, Oxidation of NiAl and FeAl, Intermetallics. 7 (1999) 1153–1158.

[11] G.H. Bozzolo, R.D. Noebe, C. Amador, Site occupancy of ternary additions to B2 alloys, Intermetallics. 10 (2002) 149–159.

[12] A. Lasalmonie, Intermetallics: Why is it so difficult to introduce them in gas turbine engines?, Intermetallics. 14 (2006) 1123–1129.

[13] G. Sauthoff, Multiphase intermetallic alloys for structural applications, Intermetallics. 8 (2000) 1101–1109.

[14] P. Korzhavyi, a. Ruban, a. Lozovoi, Y. Vekilov, I. Abrikosov, B. Johansson, Constitutional and thermal point defects in B2 NiAl, Phys. Rev. B. 61 (2000) 6003–6018.

[15] H. Clemens, W. Wallgram, S. Kremmer, V. Güther, A. Otto, A. Bartels, Design of Novel β-Solidifying TiAl Alloys with Adjustable β/B2-Phase Fraction and Excellent Hot-Workability, Adv. Eng. Mater. 10 (2008) 707–713.

[16] M. Engstler, S. Mayer, C. Pauly, H. Clemens, F. Mücklich, 3D characterization of an intermetallic β/γ-Titanium Aluminide Alloy, Adv. Eng. Mater. 15 (2013) 1125–1128.

[17] H. Clemens, W. Smarsly, Light-Weight Intermetallic Titanium Aluminides – Status of Research and Development, Adv. Mater. Res. 278 (2011) 551–556.

[18] I. Baker, A review of the mechanical properties of B2 compounds, Mater. Sci. Eng. A. 192-193 (1995) 1–13.

[19] T.M. Pollock, D.C. Lu, X. Shi, K. Eow, A comparative analysis of low temperature deformation in B2 aluminides, Mater. Sci. Eng. A. 317 (2001) 241–248.

[20] W. Clift, K. McCarty, D. Boehme, Deposition and analysis of Ir-Al coatings for oxidation protection of carbon materials at high temperatures, Surf. Coatings Technol. 42 (1990) 29–40.

[21] D. Zhong, J. Moore, T. Ohno, J. Disam, Deposition and characterization of NiAl and Ni–Al–N thin films from a NiAl compound target, Surf. Coatings Technol. 130 (2000) 33–38.

[22] D. Zhong, J.J. Moore, J. Disam, S. Thiel, I. Dahan, Deposition of NiAl thin films from NiAl compound target fabricated via combustion synthesis, Surf. Coatings Technol. 120-121 (1999) 22–27.

[23] D. Zhong, J.J. Moore, E. Sutter, B. Mishra, Microstructure, composition and oxidation resistance of nanostructured NiAl and Ni–Al–N coatings produced by magnetron sputtering, Surf. Coatings Technol. 200 (2005) 1236–1241.

[24] Z. Yu, D.D. Hass, H.N.G. Wadley, NiAl bond coats made by a directed vapor deposition approach, Mater. Sci. Eng. A. 394 (2005) 43–52.

[25] Y. Ding, Y. Zhang, D.O. Northwood, A.T. Alpas, PVD NiAl intermetallic coatings: microstructure and mechanical properties, Surf. Coatings Technol. 94-95 (1997) 483–489.

[26] C. Michaelsen, G. Lucadamo, K. Barmak, The early stages of solid state reactions in Ni/Al multilayer films, J. Appl. Phys. 80 (1996) 6689–6689.

[27] J. Noro, A.S. Ramos, M.T. Vieira, Intermetallic phase formation in nanometric Ni/Al multilayer thin films, Intermetallics. 16 (2008) 1061–1065.

[28] A.S. Ramos, M.T. Vieira, J. Morgiel, J. Grzonka, S. Simões, M.F. Vieira, Production of intermetallic compounds from Ti/Al and Ni/Al multilayer thin films—A comparative study, J. Alloys Compd. 484 (2009) 335–340.

[29] A.S. Edelstein, R.K. Everett, G.Y. Richardson, S.B. Qadri, E.I. Altman, J.C. Foley, et al., Intermetallic phase formation during annealing of Al/Ni multilayers, J. Appl. Phys. 76 (1994) 7850.

[30] H.A. Gobran, D. Heger, F. Mücklich, Determination of RuAl phase boundaries in binary Ru – Al phase diagram at room temperature and 1200 ° C, Zeitschrift Für Met. 96 (2005) 792–798.

[31] H.A. Gobran, K.W. Liu, D. Heger, F. Mücklich, Investigation on point defect structure in single phase B2 type RuAl alloys by lattice parameter measurements, Scr. Mater. 49 (2003) 1097–1102.

[32] M. Hagen, M. Finnis, Point defects and chemical potentials in ordered alloys, Philos. Mag. A. 77 (1998) 447–464.

[33] W. Jung, O. Kleppa, Standard molar enthalpies of formation of MeAl (Me= Ru, Rh, Os, Ir), Metall. Trans. B. 23 (1992) 53–56.

[34] K. Woll, C. Holzapfel, H.A. Gobran, F. Mücklich, Single-phase interdiffusion in B2-RuAl intermetallic compound, Scr. Mater. 57 (2007) 1–4.

[35] R. Fleischer, Effects of Composition on the Mechanical Properties of Tough, High-Temperature Intermetallic Compounds, ISIJ Int. 31 (1991) 86–91.

[36] I.M. Wolff, G. Sauthoff, Role of an intergranular phase in RuAl substitutional additions, Acta Mater. 45 (1997) 2949–2969.

[37] F. Soldera, N. Ilić, N. Manent Conesa, I. Barrientos, F. Mücklich, Influence of the microstructure on the formation of alumina scales on near stoichiometric RuAl produced by arc melting, Intermetallics. 13 (2005) 101–107.

[38] K.W. Liu, F. Mücklich, R. Birringer, Synthesis of nano-RuAl by mechanical alloying, Intermetallics. 9 (2001) 81–88.

[39] A. Borah, P.S. Robi, A. Srinivasan, Synthesis of nano-crystalline RuAl by mechanical alloying, Met. Mater. Int. 13 (2007) 293–302.

[40] H.A. Gobran, N. Ilić, F. Mücklich, Effects of particle size and pressure on the reactive sintering of RuAl intermetallic compound, Intermetallics. 12 (2004) 555–562.

[41] R. Fleischer, D. McKee, Mechanical and oxidation properties of AlRu-based high-temperature alloys, Metall. Mater. Trans. A. 24A (1993) 759–763.

[42] F. Cao, T.K. Nandy, D. Stobbe, T.M. Pollock, Oxidation of ruthenium aluminide-based alloys: The role of microstructure and platinum additions, Intermetallics. 15 (2007) 34–43.

[43] N. Ilić, F. Soldera, F. Mücklich, Oxidation behavior of Ru(Al)–RuAl intermetallic eutectics produced by ingot and powder metallurgy, Intermetallics. 13 (2005) 444–453.

[44] H. Grabke, M. Brumm, B. Wagemann, The oxidation of NiAl, Mater. Corros. 47 (1996) 675–677.

[45] S.A. Anderson, C.I. Lang, Thermal conductivity of ruthenium aluminide (RuAl), Scr. Mater. 38 (1998) 493–497.

[46] B. Tryon, T.M. Pollock, M.F.X. Gigliotti, K. Hemker, Thermal Expansion Behavior of Ruthenium Aluminides, Scr. Mater. 50 (2003) 9–14.

[47] R.L. Fleischer, Boron and off-stoichiometry effects on the strength and ductility of AlRu, Metall. Trans. A. 24 (1993) 227–230.

[48] R.L. Fleischer, The distribution of boron in AlRu: Effect on ductility and toughness, Acta Mater. 53 (2005) 2623–2627.

[49] I.M. Wolff, G. Sauthoff, High-temperature behavior of precious metal base composites, Metall. Mater. Trans. A. 27 (1996).

[50] Z.A. Chaudhury, C. Suryanarayana, Metastable phases in vapour-deposited Al-Ru alloys, J. Mater. Sci. 17 (1982) 3158–3164.

[51] S.M. Anlage, W.L. Johnson, E.J. Cotts, D.M. Follstaedt, J.A. Knapp, Electrical transport properties of the aluminium-ruthenium icosahedral phase, Phys. Rev. B. 38 (1988) 7802–7805.

[52] F. Mücklich, A. Lasagni, C. Daniel, Laser interference metallurgy—periodic surface patterning and formation of intermetallics, Intermetallics. 13 (2005) 437–442.

[53] J.A. Howell, C.L. Muhlstein, B.Z. Liu, Q. Zhang, S.E. Mohney, Oxidation of RuAl and NiAl Thin Films : Evolution of Surface Morphology and Electrical Resistance, J. Microelectromechanical Syst. 20 (2011) 933–942.

[54] W.K. Shen, J.H. Judy, J.-P. Wang, In situ epitaxial growth of ordered FePt (001) films with ultra small and uniform grain size using a RuAl underlayer, J. Appl. Phys. 97 (2005) 10H301.

[55] F. Klocke, T. Bergs, K. Georgiadis, H. Sarikaya, F. Wang, Coating Systems for Precision Glass Molding Tools, in: Proc. 7th Int. Conf. Coatings Manuf. Eng. (2008) 209–218.

[56] K.J. Ma, H.H. Chien, W.H. Chuan, C.L. Chao, K.C. Hwang, Design of Protective Coatings for Glass Lens Molding, Key Eng. Mater. 364-366 (2008) 655–661.

[57] J. Lin, S. Carrera, A.O. Kunrath, D. Zhong, S. Myers, B. Mishra, et al., Design methodology for optimized die coatings: The case for aluminum pressure die-casting, Surf. Coatings Technol. 201 (2006) 2930–2941.

[58] D. Zhong, G.G.W. Mustoe, J.J. Moore, J. Disam, Finite element analysis of a coating architecture for glass-molding dies, Surf. Coatings Technol. 146-147 (2001) 312–317.

[59] D. Zhong, E. Mateeva, I. Dahan, J.J. Moore, G.G.W. Mustoe, T. Ohno, Wettability of NiAl , Ni-Al-N , Ti-B-C , and Ti-B-C-N films by glass at high temperatures, Surf. Coatings Technol. 133-134 (2000) 8–14.

[60] J. Pask, R. Fulrath, Fundamentals of Glass-to-Metal Bonding: VIII, Nature of Wetting and Adherence, J. Am. Ceram. Soc. 45 (1962) 592–596.

[61] F. Mücklich, N. Ilić, K. Woll, RuAl and its alloys, Part II: Mechanical properties, environmental resistance and applications, Intermetallics. 16 (2008) 593–608.

[62] R. Bunshah, Handbook of Hard Coatings, William Andrew, 2001.

[63] D.M. Mattox, Handbook of Physical Vapor Deposition (PVD) Processing, Elsevier, 1998.

[64] K.S. Harsha, Principles of vapor deposition of thin films, Elsevier, 2005.

[65] J. Greene, Thin Film Nucleation, Growth, and Microstructural Evolution: An Atomic Scale View, in: P.M. Martin (Ed.), Handb. Depos. Technol. Film. Coatings (2009) 584–616.

[66] J.J.L. Mulders, Three-Dimensional Crystallographic Analysis Beyond EBSD Mapping: The next dimension, 2007.

[67] A. Schwartz, Electron backscatter diffraction in materials science, Kluver Academic/Plenum Publishers, 2009.

[68] D.B. Williams, C.B. Carter, Transmission Electron Microscopy, Springer, 2009.

[69] L. Spieß, G. Teichert, R. Genzel, H. Behnken, C. Genzel, Moderne Röntgenbeugung, 2nd ed., GWV Fachverlage GmbH, Wiesbaden 2009, 2009.

[70] R. Guinebretière, X-ray diffraction by polycrystalline materials, 2010.

[71] U. Welzel, J. Ligot, P. Lamparter, A.C. Vermeulen, E.J. Mittemeijer, Stress analysis of polycrystalline thin films and surface regions by X-ray diffraction, J. Appl. Crystallogr. 38 (2005) 1–29.

[72] M. Birkholz, Thin film analysis by X-ray scattering, Wiley-VCH Verlag GmbH, 2006.

[73] B. Fultz, J. Howe, Transmission Electron Microscopy and Diffractometry of Materials, 3rd ed., Springer, 2008.

[74] T.F. Kelly, M.K. Miller, Invited review article: Atom probe tomography., Rev. Sci. Instrum. 78 (2007) 031101–1/20.

[75] P. Bas, A. Bostel, B. Deconihout, D. Blavette, A general protocol for the reconstruction of 3D atom probe data, Appl. Surf. Sci. 87-88 (1995) 298–304.

[76] K. Thompson, D. Lawrence, D.J. Larson, J.D. Olson, T.F. Kelly, B. Gorman, In situ site-specific specimen preparation for atom probe tomography., Ultramicroscopy. 107 (2007) 131–9.

[77] Z. Zhang, F. Zhou, E. Lavernia, On the analysis of grain size in bulk nanocrystalline materials via x-ray diffraction, Metall. Mater. Trans. A. 34A (2003) 1349–1355.

[78] M. Kerber, E. Schafler, M. Zehetbauer, Processing and evaluation of X-ray line profiles measured from nanostructured materials produced by severe plastic deformation, Rev. Adv. Mater. Sci. 10 (2005) 427–433.

[79] K.L. Mittal, Adhesion Measurement of Films and Coatings, VSP, 1995.

[80] P. Burnett, D. Rickerby, The relationship between hardness and scratch adhession, Thin Solid Films. 154 (1987) 403–416.

[81] S.J. Bull, Failure modes in scratch adhesion testing, Surf. Coatings Technol. 50 (1991) 25–32.

[82] A.Y. Yi, A. Jain, Compression Molding of Aspherical Glass Lenses-A Combined Experimental and Numerical Analysis, J. Am. Ceram. Soc. 88 (2005) 579–586.

[83] K. Barmak, Reactive phase formation in sputter-deposited Ni/Al multilayer thin films, J. Mater. Res. 12 (1997) 133–146.

[84] P. Bhattacharya, K.N. Ishihara, K. Chattopadhyay, FeAl multilayers by sputtering: heat treatment and the phase evolution, Mater. Sci. Eng. A. 304-306 (2001) 250–254.

[85] D.M. Follstaedt, J.A. Knapp, Formation of icosahedral Al-Mn and Al-Ru solid state processes, Mater. Sci. Eng. 90 (1987) 1–8.

[86] M.K. Miller, Atom probe tomography, Springer, 2000.

[87] F. Vurpillot, A. Bostel, D. Blavette, Trajectory overlaps and local magnification in three-dimensional atom probe, Appl. Phys. Lett. 76 (2000) 3127.

[88] F. Vurpillot, D. Larson, A. Cerezo, Improvement of multilayer analyses with a three-dimensional atom probe, Surf. Interface Anal. 36 (2004) 552–558.

[89] K. Ellmer, Magnetron sputtering of transparent conductive zinc oxide: relation between the sputtering parameters and the electronic properties, J. Phys. D. Appl. Phys. 33 (2000) R17–R32.

[90] T. Ungar, J. Gubicza, Grain size, size-distribution and dislocation structure from diffraction peak profile analysis, TMS Annu. Meet. (2002) 595–604.

[91] A.S. Ramos, M.T. Vieira, Kinetics of the thin films transformation Ti/Al multilayer→γ-TiAl, Surf. Coatings Technol. 200 (2005) 326–329.

[92] E. Schmid, Aluminium-Iron-Ruthenium, in: Ternary Alloy. VCH, 1992: pp. 378–380.

[93] K.W. Liu, F. Mücklich, Thermal stability of nano-RuAl produced by mechanical alloying, Acta Mater. 49 (2001) 395–403.

[94] B. Bax, C. Pauly, P. Leibenguth, K. Woll, F. Mücklich, Synthesis of B2-RuAl coatings on mild steel by laser cladding, Surf. Coatings Technol. 206 (2012) 3931–3937.

[95] N. Birks, G.H. Meier, F.S. Pettit, Introduction to the High Temperature Oxidation of Metals, 2nd ed., Cambridge University Press, 2006.

[96] S. Bull, Techniques for improving thin film adhesion, Vacuum. 43 (1992) 517–520.

[97] J. Gerth, U. Wiklund, The influence of metallic interlayers on the adhesion of PVD TiN coatings on high-speed steel, Wear. 264 (2008) 885–892.

[98] F.. Shieu, L.. Cheng, M.. Shiao, S.. Lin, Effects of Ti interlayer on the microstructure of ion-plated TiN coatings on AISI 304 stainless steel, Thin Solid Films. 311 (1997) 138–145.

[99] K.A. Pischow, L. Eriksson, E. Harju, A.S. Korhonen, E.O. Ristolainen, The influence of titanium interlayers on the adhesion of PVD TiN coatings on oxidized stainless steel substrates, Surf. Coatings Technol. 58 (1993) 163–172.

[100] ASTM-International, ASTM C1624-05, (2005) 1–28.

[101] R. Andrievski, Review Stability of nanostructured materials, J. Mater. Sci. 8 (2003) 1367–1375.

[102] K.W. Liu, F. Mücklich, High-temperature stability of nano-grained B2-structured RuAl-based intermetallics by mechanical alloying, Intermetallics. 13 (2005) 373–376.

[103] C. Koch, I. Ovid'Ko, S. Seal, Structural Nanocrystalline Materials - Fundamentals and applications, Cambridge University Press, 2007.

[104] C. Suryanarayana, C.C. Koch, Nanocrystalline materials–Current research and future directions, Hyperfine Interact. 130 (2000) 5–44.

[105] D.A. Porter, K.E. Easterling, Phase Transformations in Metals and Alloys, 3rd ed., CRC Press, 1992.

[106] G. Gottstein, L.S. Shvindlerman, Grain Boundary Migration in Metals: Thermodynamics, Kinetics, Applications, CRC Press, 2009.

[107] C. V Thompson, Grain Growth in Thin Films, Annu. Rev. Mater. Sci. 20 (1990) 245–268.

[108] H. Hu, B. Rath, On the time exponent in isothermal grain growth, Metall. Trans. 1 (1970) 3181–3184.

[109] S.-J. Kang, Sintering: densification, grain growth and microstructure, Elsevier, 2005.

[110] C. V. Thompson, R. Carel, Stress and grain growth in thin films, J. Mech. Phys. Solids. 44 (1996) 657–673.

[111] C.V. Thompson, R. Carel, Texture development in polycrystalline thin films, Mater. Sci. Eng. B. 32 (1995) 211–219.

[112] C. Thompson, Structure evolution during processing of polycrystalline films, Annu. Rev. Mater. Sci. 30 (2000) 159–190.

[113] J. Palmer, C. Thompson, H. Smith, Grain growth and grain size distributions in thin germanium films, J. Appl. Phys. 62 (1987) 2492–2497.

[114] R. Dannenberg, E. Stach, J.R. Groza, B.J. Dresser, TEM annealing study of normal grain growth in silver thin films, Thin Solid Films. 379 (2000) 133–138.

[115] M. Iordache, S. Whang, Z. Jiao, Z. Wang, Grain growth kinetics in nanostructured nickel, Nanostructured Mater. 11 (1999) 1343–1349.

[116] L. Wang, X.Y. Qin, W. Xiong, L. Chen, M.G. Kong, Thermal stability and grain growth behavior of nanocrystalline Mg2Si, Mater. Sci. Eng. A. 434 (2006) 166–170.

[117] M. Huang, Y. Wang, Y.A. Chang, Grain growth in sputtered nanoscale PdIn thin films, Thin Solid Films. 449 (2004) 113–119.

[118] M.K. Datta, S.K. Pabi, B.S. Murty, Thermal stability of nanocrystalline Ni silicides synthesized by mechanical alloying, Mater. Sci. Eng. A. 284 (2000) 219–225.

[119] L.Z. Zhou, J.T. Guo, Grain growth and kinetics for nanocrystalline NiAl, Scr. Mater. 40 (1998) 139–144.

[120] C.E. Krill, R. Birringer, Estimating grain-size distributions in nanocrystalline materials from X-ray diffraction profile analysis, Philos. Mag. A. 77 (1998) 621–640.

[121] T. Ungar, J. Gubicza, G. Ribárik, A. Borbély, Crystallite size distribution and dislocation structure determined by diffraction profile analysis: principles and practical application to cubic and hexagonal crystals, J. Appl. Crystallogr. 34 (2001) 298–310.

[122] A. Rollett, Simulation and theory of abnormal grain growth--anisotropic grain boundary energies and mobilities, Acta Metall. 37 (1989) 1227–1240.

[123] W. Mullins, The effect of thermal grooving on grain boundary motion, Acta Metall. 6 (1958) 414–427.

[124] J.-M. Zhang, D.-D. Wang, G.-X. Chen, K.-W. Xu, Surface structure and energy of B2 type intermetallic compound NiAl, Appl. Surf. Sci. 254 (2008) 2540–2543.

[125] J. Nelson, D. Riley, An experimental investigation of extrapolation methods in the derivation of accurate unit-cell dimensions of crystals, Proc. Phys. Soc. 160 (1945) 160–177.

[126] J.C.M. Li, Microstructure and Properties of Materials: Vol 2, World Scientific Publishing Co Pte Ltd, 2000.

[127] F. Soldera, N. Ilic, S. Brännström, I. Barrientos, H.A. Gobran, F. Mücklich, Formation of Al_2O_3 Scales on Single-Phase RuAl Produced by Reactive Sintering, Oxid. Met. 59 (2003) 529–542.

[128] C. Fu, Y. Ye, M. Yoo, K. Ho, Equilibrium point defects in intermetallics with the B2 structure: NiAl and FeAl., Phys. Rev. B. Condens. Matter. 48 (1993) 6712–6715.

[129] T. Chou, The formation of discontinuous Al_2O_3 layers during high temperature oxidation of IrAl alloys, J. Mater. Res. 5 (1990) 378–384.

[130] P.J. Bellina, A. Catanoiu, F.M. Morales, M. Rühle, Formation of discontinuous Al_2O_3 layers during high-temperature oxidation of RuAl alloys, J. Mater. Res. 21 (2006) 276–286.

[131] F. Cao, T.M. Pollock, Deformation mechanisms in a Ru–Ni–Al ternary B2 intermetallic alloy, Acta Mater. 55 (2007) 2715–2727.

[132] P. Hou, Impurity effects on alumina scale growth, J. Am. Ceram. Soc. 86 (2003) 660–668.

[133] R. Klumpes, C. Maree, E. Schramm, J. Wit, The influence of chromium on the Oxidation of B-□NiAl at 1000 °C, Mater. Corros. 47 (1996) 619–624.

[134] V. Tolpygo, H. Grabke, The effect of impurities on the alumina scale growth: an alternative view, Scr. Mater. 38 (1997) 123–129.

[135] N. Takahashi, T. Mizoguchi, T. Nakagawa, T. Tohei, I. Sakaguchi, A. Kuwabara, et al., Cr diffusion in α-Al_2O_3: Secondary ion mass spectroscopy and first-principles study, Phys. Rev. B. 82 (2010) 1–5.

[136] G. Bye, G. Simpkin, Influence of Cr and Fe on formation of α-Al_2O_3 from γ-Al_2O_3, J. Am. Ceram. Soc. 57 (1974) 367–371.

[137] I. Barin, Thermochemical Data of Pure Substances, 3rd ed., VCH, 1989.

[138] A.S. Khanna, Introduction to High Temperature Oxidation and Corrosion, ASM International, 2002.

[139] M.F. Ashby, D.R.H. Jones, Engineering materials, 2nd ed., 1996.

[140] G.C. Wood, High-temperature oxidation of alloys, Oxid. Met. 2 (1970) 11–57.

[141] G. Meier, F. Pettit, The oxidation behavior of intermetallic compounds, Mater. Sci. Eng. A. 153 (1992) 548–560.

[142] M.A. Nicolet, Diffusion barriers in thin films, Thin Solid Films. 52 (1978) 415–443.

[143] R. Prescott, M.J. Graham, The oxidation of iron-aluminum alloys, Oxid. Met. 38 (1992) 73–87.

[144] C. Choux, a. J. Kulińska, S. Chevalier, High temperature reactivity of nickel aluminide diffusion coatings, Intermetallics. 16 (2008) 1–9.

[145] R. Prescott, M.J. Graham, The formation of aluminum oxide scales on high-temperature alloys, Oxid. Met. 38 (1992) 233–254.

[146] G.C. Rybicki, J.L. Smialek, Effect of the θ-Al_20_3 Transformation on the oxidation behaviour of β-NiAl+Zr, Oxid. Met. 31 (1989) 275–304.

[147] D. Barber, Electron microscopy and diffraction of aluminium oxide whiskers, Philos. Mag. 10 (1964) 75–94.

[148] G.H. Meier, Research on oxidation and embrittlement of Intermetallic Compounds in the U.S., Mater. Corros. 47 (1996) 595–618.

[149] J. Doychak, M. Rühle, TEM studies of oxidized NiAl and Ni_3Al cross sections, Oxid. Met. 31 (1989) 431–452.

[150] A. Kumar, M. Nasrallah, D. Douglass, The effect of yttrium and thorium on the oxidation behavior of Ni-Cr-Al alloys, Oxid. Met. 8 (1974) 227–263.

[151] K. Reddy, J. Smialek, A. Cooper, ^{18}O Tracer studies of Al_2O_3 scale formation on NiCrAl alloys, Oxid. Met. 17 (1982) 429–449.

[152] S. Choi, H. Cho, Y. Kim, D. Lee, High-temperature oxidation behavior of pure Ni_3Al, Oxid. Met. 46 (1996) 51–72.

[153] J. Smialek, J. Doychak, D. Gaydosh, Oxidation behavior of FeAl+ Hf, Zr, B, Oxid. Met. 34 (1990) 259–275.

[154] C. Xu, W. Gao, H. Gong, Oxidation behaviour of FeAl intermetallics. The effects of Y and/or Zr on isothermal oxidation kinetics, Intermetallics. 8 (2000) 769–779.

[155] P.Y. Hou, X.F. Zhang, R.M. Cannon, Impurity distribution in Al_2O_3 formed on an FeCrAl alloy, Scr. Mater. 50 (2004) 45–49.

[156] F. Liu, K. Stiller, Atom probe tomography of thermally grown oxide scale on FeCrAl., Ultramicroscopy. 132 (2013) 279–84.

[157] ASM Handbook: Volume 3: Alloy Phase Diagrams (ASM Handbook), ASM International, 1992.

[158] M. De Graef, Introduction to conventional Transmission Electron Microscopy, Cambridge University Press, 2003.

[159] O. Ueda, S. Isozumi, S. Komiya, Composition-modulated structures in InGaAsP and InGaP liquid phase epitaxial layers grown on (001) GaAs substrates, Jap. J. Appl. Phys. (1984) L241–L243.

[160] Z. Liliental-Weber, D.N. Zakharov, K.M. Yu, J.W. Ager, W. Walukiewicz, E.E. Haller, et al., Compositional modulation in $In_{(x)}Ga_{(1-x)}N$: TEM and X-ray studies., J. Electron Microsc. (Tokyo). 54 (2005) 243–50.

[161] D.R. Clarke, The lateral growth strain accompanying the formation of a thermally grown oxide, Acta Mater. 51 (2003) 1393–1407.

[162] W. Bell, M. Tagami, High-temperature chemistry of the ruthenium-oxygen system, J. Phys. Chem. 7 (1963) 2432–2436.

[163] B.A. Pint, Optimization of Reactive-Element Additions to Improve Oxidation Performance of Alumina-Forming Alloys, J. Am. Ceram. Soc. 86 (2003) 686–95.

[164] J. Stringer, Stress generation and relief in growing oxide films, Corros. Sci. 1 (1970) 513–543.

[165] S.-L. Shang, H. Zhang, Y. Wang, Z.-K. Liu, Temperature-dependent elastic stiffness constants of α- and θ-Al_2O_3 from first-principles calculations., J. Phys. Condens. Matter. 22 (2010) 1–8.

[166] Y. Waseda, E. Matsubara, K. Shinoda, X-Ray diffraction Crystallography, Springer-Verlag, 2011.

[167] F. Pettit, J. Wagner, Transition from the linear to the parabolic rate law during the oxidation of iron to wüstite in CO-CO2 mixtures, Acta Metall. 12 (1964) 35–40.

[168] F. Pettit, R. Yinger, J. Wagner, The mechanism of oxidation of iron in carbon monoxide-carbon dioxide mixtures, Acta Metall. 8 (1960) 617–623.

[169] K.R. Lawless, The oxidation of metals, Reports Prog. Phys. 37 (1974) 231–316.

[170] M.A. Guitar, F. Mücklich, Isothermal Oxidation Behaviour of Nanocrystalline RuAl Intermetallic Thin Films, Oxid. Met. 80 (2013) 423–436.

[171] J. Bernardini, Grain boundary diffusion in metallic nano and polycrystals, Interface Sci. 62 (1997) 55–62.

[172] G. Cao, L. Geng, Z. Zheng, M. Naka, The oxidation of nanocrystalline Ni3Al fabricated by mechanical alloying and spark plasma sintering, Intermetallics. 15 (2007) 1672–1677.

[173] G. Liu, Y. Zhu, K. Mimura, M. Isshiki, Effect of Alloying Element of S, Se or te on Oxidation Resistance of Cu at 573-873 K, Open Corros. J. 3 (2010) 92–98.

[174] P. Panjan, M. Čekada, M. Panjan, D. Kek-Merl, Growth defects in PVD hard coatings, Vacuum. 84 (2009) 209–214.

[175] W. Thongkham, R. Sakdanuphab, C. Chityuttakan, S. Chatraphorn, Effect of Diffusion Barrier and Substrate Temperature on the Physical Properties of Flexible Cu(In,Ga)Se_2 Thin Film Solar Cells, J. Met. Mater. Miner. 20 (2010) 61–65.

[176] G. Young, R. Glenn, Feasibility Study of Tungsten as a Diffusion Barrier Between Nickel-Chromium-Aluminium and γ/γ'-δ Eutectic Alloys, Cleveland, Ohio, 1978.

[177] L.-C. Chang, Y.-I. Chen, J.-W. Lee, H.-Y. Lin, Y.-C. Kuo, C.-J. Wang, Detaching mechanism for Mo–Ru hard coating on tungsten carbide, Surf. Coatings Technol. 202 (2007) 967–972.

[178] Y.-I. Chen, K.-T. Liu, F.-B. Wu, J.-G. Duh, Mo–Ru coatings on tungsten carbide by direct current magnetron sputtering, Thin Solid Films. 515 (2006) 2207–2212.

[179] S. Nishiyama, E. Takahashi, Y. Iwamoto, Boron nitride hard coatings by ion beam and vapor deposition, Thin Solid Films. 281-282 (1996) 327–330.

[180] T.-N. Lin, S. Han, K.-W. Weng, C.-T. Lee, Investigation on the structural and mechanical properties of anti-sticking sputtered tungsten chromium nitride films, Thin Solid Films. 529 (2013) 333–337.

[181] F. Klocke, Complete qualification methodology for coatings of precision glass molding tools, Opt. Eng. (2012) 073401–1–9.

[182] Y.-Y. Chang, C.-M. Cheng, Y.-Y. Liou, W. Tillmann, F. Hoffmann, T. Sprute, High temperature wettability of multicomponent CrAlSiN and TiAlSiN coatings by molten glass, Surf. Coatings Technol. 231 (2013) 24–28.

[183] Y.-Y. Chang, H.-M. Lai, H.-Y. Kao, High temperature wettability of ion implanted multicomponent CrAlSiN films by molten glass, Surf. Coatings Technol. (2013) 6–11.

[184] J. Moore, D. Zhong, J. Lin, Coatings for glass molding dies and forming tools, US2005/0268662, 2011.

[185] G. Kleer, E. Kaiser, W. Döll, Behaviour of Ti-Al-N coatings for tools applied in the thermoplastic moulding of inorganic glasses, Surf. Coatings Technol. 79 (1996) 95–102.

[186] S.C. Liu, Y. Chen, H.Y. Tsai, K.C. Lin, Y.H. Chen, Thermal stability of Ir–Re coatings annealed in oxygen-containing atmospheres, Surf. Coatings Technol. (2013) 1–7.

[187] V. Nagesh, A. Tomsia, J. Pask, Wetting and reactions in the lead borosilicate glass-precious metal systems, J. Mater. Sci. 18 (1983) 2173–2180.

[188] G. Copley, A. Rivers, R. Smith, Contact angle measurements of E-glass with platinum group metals, J. Mater. Sci. 10 (1975) 1285–1290.

[189] C.-L. Chao, C.-B. Huo, W.-C. Chou, Y.-R. Lin, K.-J. Ma, H.-H. Chien, Study on the design of precious metal based protective films for glass moulding process, Surf. Coatings Technol. 231 (2013) 567–572.

[190] N. Eustathopoulos, M.G. Nicholas, B. Drevet, Wettability at High Temperatures, Pergamon, 1999.

[191] E.C. Donalson, W. Alam, Wettability, Gulf Publishing company, Houston, 2008.

[192] N. Sobczak, M. Singh, R. Asthana, High-temperature wettability measurements in metal/ceramic systems – Some methodological issues, Curr. Opin. Solid State Mater. Sci. 9 (2005) 241–253.

[193] P.J. Skrdla, Semi-empirical description of the constant β in the equation of state for interfacial tension., J. Colloid Interface Sci. 360 (2011) 313–6.

[194] J. Pech, M. Braccini, A. Mortensen, N. Eustathopoulos, Wetting, interfacial interactions and sticking in glass/steel systems, Mater. Sci. Eng. A. 384 (2004) 117–128.

[195] C. Ward-Close, R. Minor, P. Doorbar, Intermetallic-matrix composites - a review, Intermetallics. 4 (1996) 217–229.

List of figures